

IntechOpen

Fusion Energy

Edited by Aamir Shahzad



Fusion Energy

Edited by Aamir Shahzad

Published in London, United Kingdom



IntechOpen





Supporting open minds since 2005



Fusion Energy

<http://dx.doi.org/10.5772/intechopen.78809>

Edited by Aamir Shahzad

Contributors

Ronald Hemsworth, Deirdre Boilson, Vladimir Gribkov, Tao Zhang, Aamir Shahzad, Mikhail Tokar, Masahiro Kobayashi, Pingping Liu

© The Editor(s) and the Author(s) 2020

The rights of the editor(s) and the author(s) have been asserted in accordance with the Copyright, Designs and Patents Act 1988. All rights to the book as a whole are reserved by INTECHOPEN LIMITED. The book as a whole (compilation) cannot be reproduced, distributed or used for commercial or non-commercial purposes without INTECHOPEN LIMITED's written permission. Enquiries concerning the use of the book should be directed to INTECHOPEN LIMITED rights and permissions department (permissions@intechopen.com).

Violations are liable to prosecution under the governing Copyright Law.



Individual chapters of this publication are distributed under the terms of the Creative Commons Attribution 3.0 Unported License which permits commercial use, distribution and reproduction of the individual chapters, provided the original author(s) and source publication are appropriately acknowledged. If so indicated, certain images may not be included under the Creative Commons license. In such cases users will need to obtain permission from the license holder to reproduce the material. More details and guidelines concerning content reuse and adaptation can be found at <http://www.intechopen.com/copyright-policy.html>.

Notice

Statements and opinions expressed in the chapters are these of the individual contributors and not necessarily those of the editors or publisher. No responsibility is accepted for the accuracy of information contained in the published chapters. The publisher assumes no responsibility for any damage or injury to persons or property arising out of the use of any materials, instructions, methods or ideas contained in the book.

First published in London, United Kingdom, 2020 by IntechOpen

IntechOpen is the global imprint of INTECHOPEN LIMITED, registered in England and Wales, registration number: 11086078, 7th floor, 10 Lower Thames Street, London, EC3R 6AF, United Kingdom

Printed in Croatia

British Library Cataloguing-in-Publication Data

A catalogue record for this book is available from the British Library

Additional hard and PDF copies can be obtained from orders@intechopen.com

Fusion Energy

Edited by Aamir Shahzad

p. cm.

Print ISBN 978-1-78985-413-8

Online ISBN 978-1-78985-414-5

eBook (PDF) ISBN 978-1-78985-845-7

We are IntechOpen, the world's leading publisher of Open Access books Built by scientists, for scientists

4,700+

Open access books available

121,000+

International authors and editors

135M+

Downloads

151

Countries delivered to

Our authors are among the
Top 1%

most cited scientists

12.2%

Contributors from top 500 universities



WEB OF SCIENCE™

Selection of our books indexed in the Book Citation Index
in Web of Science™ Core Collection (BKCI)

Interested in publishing with us?
Contact book.department@intechopen.com

Numbers displayed above are based on latest data collected.
For more information visit www.intechopen.com



Meet the editor



Aamir Shahzad has more than fourteen years of experience of university research and teaching at home and abroad. Dr. Shahzad received postdoctoral and doctoral degrees from Xi'an Jiaotong University (XJTU), China, in 2015 and 2012. He has proposed novel methods for exploring outcomes of complex materials in the fields of computational physics and molecular modeling and simulation. Dr. Shahzad's interests include computational physics, complex fluids/plasmas, plasma oncology, and bio- and energy materials. Currently, Dr. Shahzad is a tenured associate professor in the Department of Physics at GC University Faisalabad (GCUF). Dr. Shahzad is a member of the ThermoPhysical Society at Xian Jiaotong University, as well as the Physics societies at GCUF and the University of Agriculture Faisalabad, Pakistan.

Contents

Preface	XIII
Section 1	
Experimental Fusion Studies	1
Chapter 1	3
Research, Design, and Development Needed to Realise a Neutral Beam Injection System for a Fusion Reactor <i>by Ronald Stephen Hemsworth and Deirdre Boilson</i>	
Chapter 2	25
Taxonomy of Big Nuclear Fusion Chambers Provided by Means of Nanosecond Neutron Pulses <i>by Vladimir Gribkov, Barbara Bienkowska, Slawomir Jednorog, Marian Paduch and Krzysztof Tomaszewski</i>	
Chapter 3	55
Experimental Studies of and Theoretical Models for Detachment in Helical Fusion Devices <i>by Masahiro Kobayashi and Mikhail Tokar</i>	
Section 2	
Modeling and Simulation Studies	83
Chapter 4	85
Wave Spectra in Dusty Plasmas of Nuclear Fusion Devices <i>by Aamir Shahzad, Muhammad Asif Shakoori and Mao-Gang He</i>	
Chapter 5	103
Measurement of Vacancy Migration Energy by Using HVEM <i>by Pingping Liu</i>	
Chapter 6	115
The Tungsten-Based Plasma-Facing Materials <i>by Tao Zhang, Zhuoming Xie, Changsong Liu and Ying Xiong</i>	

Preface

This book presents fundamental and applied research in plasma physics and fusion energy. It discusses the latest developments and innovative techniques of fusion energy and its practical uses.

The challenge in exploring fusion energy and indirect plasma physics is the obvious complexity. Production of clean and environmentally friendly energy on a large scale is a global challenge for plasma scientists and technologists. To achieve fusion energy, we need to confine fusion plasma. Confinement of fusion plasma is a key scientific problem that involves understanding anomalous transport processes in a tokamak device.

Chapter 1 discusses the research, design and development needed to realise a neutral beam injection system (NBI) for a fusion reactor. NBI is the most successful heating method used for fusion devices. Chapter 2 explains the taxonomy of big nuclear fusion chambers provided by means of nanosecond neutron pulses. The method is based on use of very bright nanosecond neutron pulses generated from a compact neutron source of a dense plasma focus type in two classes of experimental methods supported by MCNP numerical modeling. Chapter 3 incorporates experimental studies and theoretical models for detachment in helical fusion devices, including Tokamaks JET, JT-60U and heliotrons LHD. By approaching the density limit, the plasma detaches from the divertor target plates so that the particle and heat fluxes onto the targets reduce dramatically. Chapter 4 presents investigations of wave spectra through an equilibrium molecular dynamic simulation of three-dimensional, strongly coupled complex-dusty plasmas. The EMD method is the best tool for computing CL and CT in the dusty plasma over a suitable range of plasma parameters. Chapter 5 gives the measurement of vacancy migration energy by using a high-voltage electron microscope (HVEM). It investigates the vacancy migration energy on the HVEM. Chapter 6 discusses tungsten-based plasma-facing materials. Tungsten is considered the most promising material for plasma facing components (PFCs) in magnetic confinement fusion devices due to its high melting temperature, high thermal conductivity, low swelling, low tritium retention and low sputtering yield.

Dr. Aamir Shahzad
Tenured Associate Professor,
Molecular Modeling and Simulation Laboratory,
Department of Physics,
Government College University Faisalabad,
Pakistan

Key Laboratory of Thermo-Fluid Science and Engineering,
Ministry of Education (MOE),
Xi'an Jiaotong University,
P.R. China

Section 1

Experimental Fusion Studies

Research, Design, and Development Needed to Realise a Neutral Beam Injection System for a Fusion Reactor

Ronald Stephen Hemsworth and Deirdre Boilson

Abstract

The ion temperature in the plasma in a fusion reactor must be sufficiently high that the fusion reaction (probably between D^+ and T^+) will need to be high to ensure that the reaction rate is as high as is required. The plasma will be heated by the energetic alpha particle created in the fusion reaction, but it is widely accepted that additional (externally supplied) heating will also be required to ensure a sustained “burn” and, perhaps, to control the reaction rate. A reactor based on the tokamak confinement system requires a toroidal current to flow in the plasma. Most of that current will be created by the “bootstrap” effect, but an external method of driving current in the poloidal centre of the plasma is needed as the bootstrap current will be low, or zero in that region. Neutral beam injection is an efficient heating mechanism and it has the current drive efficiency required in a reactor. In this chapter the R&D required for an NBI system for a reactor, is considered against the background of the ITER NBI system design as the ITER beam energy and operating environment are reactor relevant. In addition the elements requiring most development are identified.

Keywords: neutral beam injection, negative ion sources, beamline design

1. Basic considerations for a neutral beam injection system on a reactor

A neutral beam system on a fusion reactor will have to meet specifications that are significantly beyond those of any system so far designed. The injectors will be directly connected to the reactor vessel, and therefore they will both form a part of the nuclear confinement barrier and be subjected to high levels of neutron and gamma radiation. Consequently, the injector design must include a radiation barrier around the injectors; the choice of materials that can be used must be acceptable to the vacuum environment, be radiation tolerant, and, where possible, be low-activation materials. In addition, the design will have to satisfy the nuclear regulator, which, typically, limits the engineering design codes that can be used.

It is clear that the main factors that will influence the design of the injectors, and require R&D, are the pulse length, the global efficiency, operation and maintenance in a nuclear environment, and component lifetime. In the following sections of this chapter, each of the aforementioned aspects is discussed more in detail and some

suggestions given as to how problems arising from each aspect may be resolved and the parameters of the future injectors achieved. However it is important to understand that although various basic conceptual designs of an injector to be used on a fusion reactor have been considered [1–3], no concept has been chosen, and no serious engineering design of any concept has been carried out. Experience with the design of the neutral beam systems has shown that many aspects of the conceptual design are changed significantly during the engineering design phase. For example:

- The initial design of the neutral beam system on the JET tokamak had one single large ion source, whereas the final design has eight smaller beam sources [4] with the accompanying four residual ion deflection and collection systems and four beamline calorimeters.
- The initial design of the ITER injectors used a vacuum vessel of cylindrical cross section, and all component removal and maintenance were to be carried out through the rear of that vessel [5]. The design being constructed uses a vessel that is rectangular in cross section with a removable lid that allows removal and maintenance of the beamline components from above the injector [6].

It is clear from the above examples that the resolution of problems arising from operation in the fusion reactor environment, for example, maintenance of the injector components, can depend strongly on details of the injector design and that the methods to achieve the required parameters of the injectors may also depend strongly on the details of the design. Therefore the following sections of this chapter do not consider any design in detail, but, against the background of the design of the injectors for ITER, they try to describe the problems that will arise and to suggest ways in which they might be resolved. Also it is important to understand that the components of a neutral beam injector are interdependent and that in the following sections the assumptions made about the design and/or performance of the injector are self-consistent.

2. Issues related to the design of a neutral beam injector operating on a fusion reactor, some possible ways to resolve those issues and suggested R&D

2.1 Global efficiency

The global efficiency of a heating system is simply the ratio of the electrical power required to operate the heating system divided by the power absorbed by the device being heated, the fusing plasma in the case of a fusion reactor, and it is of overriding importance for a fusion reactor. This can easily be understood with an example: suppose that the heating power required to heat the fusing plasma to the temperature required to ensure that the rate of fusion reactions in the plasma is that required to achieve the electrical output from the reactor is 100 MW. Then, if the global efficiency of the heating system were similar to that achieved by the systems operating today, of the order of 25%, about 400 MW of electrical power would be required simply to operate the heating system, that is, the output of a typical power station. There have been several studies aimed at defining an acceptable global efficiency for the heating systems of a fusion reactor, and the typical result is $\approx 60\%$ or higher [7].

The specification of the neutral beam injectors designed for ITER is the closest of any design to that which would be suitable for use on a fusion reactor.

Thus it is interesting to look at the expected efficiency of the ITER injectors to see where improvements must be made. **Table 1** shows the expected performance of an ITER-like injector plus indications of possible performance changes that could lead to an injector operating on a fusion reactor. Each of the suggested changes is discussed in more detail below.

Before discussing the various items impacting the global efficiency, it is important to understand some of the more important constraints on the design of the injectors.

Firstly, the injectors will need to be commissioned after the first installation on the reactor and then maintained and recommissioned several times during their lifetime. Commissioning or recommissioning of all the injectors involves firing the neutral beam through the beamline components and into a beam dump, usually called a calorimeter. The overall process is that at the start of commissioning, the beam source is operated at low power and beam energy and for short pulse lengths, for example, 5–10 s. That ensures safe operation of the system even if the beam quality, such as the beamlet divergence, is not optimal. Once safe, good operation is achieved at the selected low power, the beam power, energy, and pulse length are gradually increased. This continues until full power and pulse length are achieved, always with the neutral beam being intercepted on the calorimeter. No system has yet been developed which allows commissioning of the high power beam system without a calorimeter. As it is almost certain that a calorimeter is required, it must be designed to withstand the power and power density it will be subjected to, and this has been demonstrated to be a restricting factor in the design of an injector for the ITER heating NB injectors. The calorimeter was one of the most difficult beamline components to be designed, and it can be reasonably considered that the power and power density handling of the ITER calorimeter design is close to the limit of what is technologically possible. Thus the beamline calorimeter sets a limit on the neutral beam power that can be produced by a neutral beam injector of ≈ 17 MW. In **Table 1**, the changes to be made for an injector to be used in a fusion reactor are such that this limitation is respected.

Table 1 gives a calculation of the global efficiency of an ITER-like heating neutral beam injector (HNB) and of a possible injector for a fusion reactor. Both deliver ≈ 17 MW of 1 MeV D^0 to the plasma in the device. The calculations in **Table 1** assume that for the injector on a fusion reactor:

- I. The ion source and accelerator will be similar to those of the ITER-like injector.
- II. The gas flow into the ion source will be 3 times lower than the flow into that of the ITER-like injector.
- III. The ion source on the injector on a fusion reactor will be based on solid-state technology with an efficiency of 85%.

A photon neutraliser will be used that has a neutralisation efficiency of 90% and a laser power of 800 kW, with a laser efficiency of 40%. A lower laser efficiency would be acceptable if the required laser power is < 800 kW.

2.1.1 Detailed discussion

This section discusses the items of **Table 1** that are considered not to be self-explanatory.

		ITER-like injector (MW)	Reactor injector (MW)
1	RF power to ion source	0.8	0.4
2	Electrical power for the ion source: the AC to RF conversion efficiency for the ITER-like ion source power supplies is $\approx 50\%$. The efficiency of the solid-state RF power supplies used for the reactor injectors is assumed to be 85%	1.6	0.5
3	Stripping loss: this is approximately proportional to the gas flow from the source, which is assumed to be reduced by a factor 3 for the reactor injectors	8.0	1.5
4	Back-streaming ion power: this is approximately proportional to the gas flow from the source (see above)	1.0	0.2
5	Electron power exiting the accelerator: this is approximately proportional to the gas flow from the source (see above).	1.0	0.2
6	Total accelerated power	40.0	22.3
7	Total power lost in the accelerator (including back-streaming ions): this is approximately proportional to the gas flow out of the source (see above).	10.0	1.9
8	DC power to accelerator:	50.0	24.1
9	Electrical power to the accelerator: the AC to DC conversion for the accelerator power supplies is assumed to be 87.5% for both injectors	57.1	27.6
10	Beamlet halo: for the beam source of the HNBS, this is assumed to carry 15% of the power of each beamlet, whereas that of the reactor beam source is assumed to be 5%	6.0	1.1
11	Neutral power exiting the neutraliser: neutralisation for the D ₂ target is $\approx 56\%$; with a photon neutraliser, it is assumed to be 90%	19.0	19.0
12	Neutral power to ITER without re-ionisation loss: the geometric transmission is taken to be the same for both injectors, 95%, for the core of the beamlets	18.1	18.1
13	Re-ionisation loss: in the reactor injector, the total gas influx is reduced by a factor of ≈ 15 ; consequently the re-ionisation losses are similarly reduced	0.9	0.06
14	Power injected into ITER:	17.2	18.1
15	Electrical power to the electrostatic residual ion dump: this is reduced because of the considerably higher neutralisation achieved with the photon neutraliser	1.05	0.04
16	Electrical power to the laser: 800 kW of laser power is assumed to be required to inject sufficient photons into the neutraliser, and the laser efficiency is assumed to be 40%	0.0	2.0
17	Electrical power to the active correction and compensation coils: assuming that the AC to DC conversion efficiency for the ACC coil power supply is 95%	1.6	1.1
18	Electrical power for the cryogen supply: 0.5 MW is estimated as the additional power at 4 K in the ITER cryoplant needed for the HNB cryopumps (≈ 5 MW electrical power). The required pumping speed is reduced in proportion to the gas flow per injector, and the power in the reactor cryoplant is similarly reduced.	5.0	0.2

	ITER-like injector (MW)	Reactor injector (MW)
19 Electrical power for the water cooling of the beam source and the beamline components: the power needed for the water pumps for the higher efficiency injector is reduced proportionately	0.8	0.1
Total electrical power to the injector	67.2	32
Overall efficiency	26%	57%

Table 1. Global efficiency of the ITER HNBs and possible injectors for a fusion reactor, based on reduced gas flow into the ion source, improved RF power supplies and a photon neutraliser.

2.1.1.1 RF power to the ion source

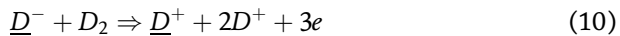
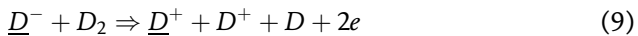
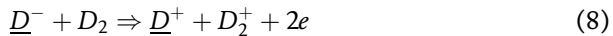
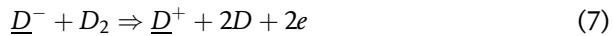
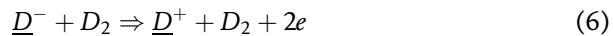
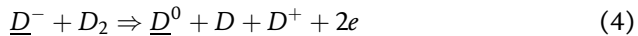
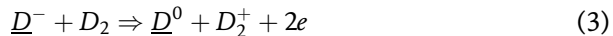
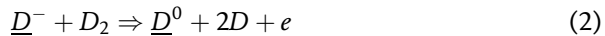
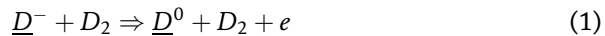
The requirement to limit the neutral power to the calorimeter combined with efficiency increases elsewhere in the injector for a fusion reactor leads to a reduction in the accelerated negative ion current of about a factor 2 (see Section 2.1.1.5.), which leads to a similar reduction in the maximum power into the RF source. The reduction in the accelerated negative ion current leads to a more easily realised extracted negative ion current, lower power to the extraction and acceleration grids, lower back-streaming ion power, and lower electron power exiting the accelerator, all of which are very desirable.

2.1.1.2 Electrical power for the ion source

The current design of the RF power supply for the ITER neutral beam injectors uses a high power tetrode oscillator, which results in an efficiency of RF power production of about 50%. More modern RF power supplies which use solid-state technology have a power efficiency of about 85%. The use of such solid-state RF power supplies with an ITER-relevant type of RF-driven ion source has recently been successfully demonstrated at the ELISE facility in IPP, Garching, Germany [8].

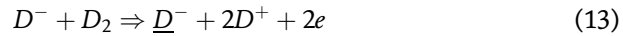
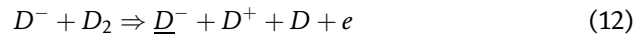
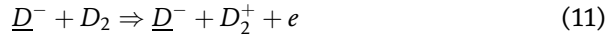
2.1.1.3 Stripping loss and back-streaming positive ions

The negative ions extracted from the ion source can, and do, undergo diverse charge changing reactions with the background gas:



where the underlined species are high-energy particles. Because the above reactions occur inside the accelerator, the produced \underline{D}^0 will not have the full acceleration energy, and the precursor \underline{D}^- will not have experienced the full electrostatic optics of the extractor and accelerator, and therefore the \underline{D}^0 will in general have a higher divergence than the fully accelerated \underline{D}^- . After it is created, the \underline{D}^+ will be decelerated, and it will either exit the accelerator with reduced energy, or they will be reflected, and they return to the ion source, and they will impinge on the rear of the ion source.

In addition to the above reactions, the accelerated \underline{D}^- can simply ionise the background gas, that is:



The D^+ and D_2^+ created in reactions (11)–(13) will be back-accelerated, and they return to the ion source, and they will impinge on the rear of the ion source.

The background gas in the extractor and accelerator of a negative ion-based injector comes overwhelmingly from the ion source, and the background gas density decreases with the distance from the plasma grid. That, combined with the fact that the cross sections of reactions (1)–(13) decrease with the energy of the precursor D^- at energies above ≈ 10 keV, means that essentially all the D^0 produced by reactions (1)–(5) is not useful for heating a fusion reactor and the precursor D^- is considered as lost in the accelerator. Although the D^+ created by reactions (6)–(10) can be neutralised to produce D^0 , that reaction is negligible for D^+ at energies close to that required of the D^0 needed to heat the fusing plasma, so the D^- that undergoes reactions (6)–(10) is also considered to be completely lost. The losses via reactions (1)–(10) are commonly referred to as stripping loss.

In the case of the ITER heating neutral beam injectors, the stripping loss is calculated to be ≈ 8 MW, and the power in the back-streaming positive ions (mainly from reactions (11)–(13)) is calculated to be ≈ 1 MW. It is obvious that losing ≈ 9 MW in an injector that is designed to deliver ≈ 17 MW to the plasma has a major impact on the global efficiency of the injector, and it must be reduced if the target of 60% global efficiency is to be met. As noted above, most of the background gas in the accelerator comes from the ion source. Hence to achieve a global efficiency of 60%, that gas flow must be reduced. Fortunately, it has been demonstrated with a filamented ion source that extracted current densities higher than those needed in the injectors for a fusion reactor assumed in **Table 1** can be achieved with a filling pressure (the pressure in the in source without source operation) of 0.1 Pa [9], a factor 3 lower than the target value for the ITER injectors. Thus that value is chosen in **Table 1** for the injector of a fusion reactor. It must be noted that any filamented source, including the source type where operation at the low gas flow has been demonstrated, is not considered suitable for use on an injector to be used on a fusion reactor because of the limited lifetime of the filaments (< 200 h). Operation at such a low gas flow has not yet been achieved in the type of source to be used on the ITER injectors, an RF-driven source, and significant R&D is needed to develop an RF-driven source that can operate at such low gas flows.

Back-streaming ions are positive ions that are created inside the accelerator, which are then accelerated back to the ion source by the electrical fields in the accelerator. There are three reasons the power in the back-streaming ions must be reduced in an injector on a reactor:

- i. Reduction of the back-streaming ion power contributes to increasing the global efficiency of the injectors.
- ii. Lifetime of the ion source backplates: the back-streaming ions sputter material from the backplates, and eventually the back-streaming ions will drill through the backplate and, most likely, reach the cooling water channel in the backplate. This problem is avoided in the sources designed for ITER by having a 1-mm-thick molybdenum layer on surface of the backplates receiving the back-streaming ions. Most of the sputtering is due to H_2^+ (from reaction (11)), and the sputtering rate of Mo bombarded by H_2^+ is low compared to other possible materials (copper, nickel, etc.), and it is calculated that a 1-mm-thick layer of Mo will not be eroded away during the foreseen lifetime of ITER [10]. The calculations in [10] predict an erosion depth of ≈ 0.5 mm during the ITER lifetime, but they assume that D^+ and D_2^+ are the only back-streaming ions. In fact Cs will be present in the extractor, and at a lower density in the accelerator, that Cs will be ionised by the accelerated D^- and back-accelerated into the source. It is calculated that the erosion by Cs^+ could be as important as that of the D_2^+ [11] and that back-streaming Cs^+ will overlap with the back-streaming D_2^+ and add to the erosion by D_2^+ . The erosion over the lifetime of the reactor would be about 20 times higher than in the ITER HNBS, which have a duty cycle of 25%. The Mo layer thickness cannot be increased 20-fold to counter that as that would lead to a design of the backplates that cannot withstand the power density from the back-streaming ions.
- iii. Reduction of the Cs “consumption”: the conversion of D atoms impacting the PG with a low work function surface is the main method of D^- in the ion source. To create the low work function surface Cs is injected into the ion source and deposited on the PG. If Cs injection is stopped, the extracted ion current is found to decrease after some period of operation, which is due to the an increasing PG surface work function, which may be caused by impurities reacting with the Cs on the PG, or coating of the Cs by other material. This is termed “Cs consumption”. In order to maintain the D^- production rate and the extracted D^- current constant, it is found necessary to inject Cs into the ion source periodically or even continuously. To avoid the metal sputtered from the backplates that is deposited on the PG, increasing the work function is likely to increase the Cs consumption rate, which is highly undesirable (see Section 4).

It has been suggested that if the plasma grid were made from a low work function material, there would be no need to inject caesium into the source, with the accompanying problems discussed in Section 4. However, as mentioned above, if the PG is coated by several monolayers of metal sputtered from the backplates, the work function will increase leading to a reduction in the negative ion production and hence in the extracted current. The sputtering rate for the ITER beam source is by back-streaming D_2^+ which is calculated to be 5×10^{16} atoms/s, and the rate for the injector on a reactor may be a factor ≈ 6 lower if the extracted current density is lower (see Section 1.2) by a factor 2 and the gas density in the accelerator is reduced by a factor 3. As a monolayer corresponds to about 10^{17} m^{-2} , so it is obvious that several monolayers of the sputtered material will be deposited on the PG in a time that is short compared to the reactor lifetime.

Potential solutions to the problems discussed above are:

- a. Easily replaceable backplates plus a reduction in the back-streaming ion flux. Since the back-streaming D_2^+ is directly proportional to the of D_2 in the

extractor and accelerator and that of Cs^+ ion intensity is directly proportional to the density of Cs in the extractor, reducing by a factor 3 the D_2 flow out of the ion source and the Cs density in front of the PG would reduce the sputtering of the ion source backplates enough to avoid the erosion causing a water leak in <1 year of reactor operation, allowing the backplates to be replaced during an annual maintenance period.

- b. It should be noted that a factor 3 reduction in the sputtering of the backplates is not sufficient to prevent a non-renewable PG surface deteriorating in a time that is short compared to the lifetime of a reactor.
- c. Bending of the D^- after the extraction grid and offsetting the subsequent acceleration grids such that the back-streaming ions, which cause most of the sputtering of the backplates, could be directed onto dumps that are separated from the beam source. The reduction in the sputtering thus achieved should be sufficient to allow the backplates to survive for more than 1 year, but replacement of the backplates must be foreseen.
- d. Unfortunately the reduction in the sputtering would not be sufficient to allow a non-renewable low work function PG to maintain its low work function for the lifetime of a reactor. Therefore, the use of a non-renewable low work function PG is not viable.
- e. In situ cleaning of the sputtered material off the PG might allow a low work function PG to be used. Of course that would not solve the backplate problem. As a and b above do not solve the problem of the sputtered material “polluting” the PG, it can be concluded that there is little point in carrying out R&D on the creation of a low work function PG unless a technique is developed to remove the sputtered material from the PG in situ.

2.1.1.4 Electrons exiting the accelerator

Some electrons are co-extracted from the ion source, and, as noted in Section 2.1.1.3, electrons are created in the accelerator via reactions (1)–(13). Electrons in the extractor and accelerator will be co-accelerated along with the negative ions until they are deflected onto the extraction grid or one of the accelerator grids, or they exit the accelerator. The power loss in the extractor is given in **Table 1**, line 2, and line 5 gives the power in the electrons exiting the accelerator. That power is deposited on downstream beamline components and the beamline vessel. The reduction in the gas density in the extractor and accelerator, as discussed above, results in a reduction in the exiting electron power by a factor similar to the reduction factor for the back-streaming ions.

2.1.1.5 Total accelerated power

Line 6 of **Table 1** gives the total accelerated D^- power for the injector to be used on a fusion reactor as 22.3 MW compared to 40 MW for a heating neutral beam injector for ITER. The main reason for the reduced accelerated D^- power is to keep the power density on the calorimeter similar to that of the ITER injector.

2.1.1.6 Beamlet halo

Early measurements of negative ion beamlet profiles suggested that the optics of the beamlets are not well described by a simple Gaussian divergence, that is,

$$P(\omega) = P_0 * \exp\left(-\left\{\frac{\omega^2}{\omega_0^2}\right\}\right) \quad (14)$$

where $P(\omega)$ is the power density at a radial position that subtends an angle with respect to the beamlet axis of ω and ω_0 is the beamlet divergence. The measured profiles were found to be better fitted by a bi-Gaussian profile. For the ITER design, the latter was chosen, that is,

$$P(\omega) = (1 - f) * P_0 * \exp\left(-\left\{\frac{\omega^2}{\omega_0^2}\right\}\right) + f * P_0 * \exp\left(-\left\{\frac{\omega^2}{\omega_{0h}^2}\right\}\right) \quad (15)$$

where f is the fraction of the beamlet power carried by the “halo”, which has a divergence of ω_{0h} . For the ITER design, f was assumed to be 15%. It is assumed that R&D from the ITER neutral beam test bed and other negative ion-based systems will allow an improved optics with a halo carrying only 5% of the beamlet power.

3. Pulse length

All neutral beam injection systems that have been designed or built have been conceived for a pulsed mode operation, whereas fusion reactors, and any NBI system to be used on the reactor, are expected to operate continuously for 1 year or more. Continuous operation will require fundamental changes in the design of the injectors, such as:

3.1 Pumping and gas flow

All NBI systems so far designed and/or built require very high pumping speed at the exit of the accelerator and downstream of the residual ion dump in order to minimise beam loss. The former is needed in order to reduce the gas density, and hence the stripping losses, in the accelerator and the latter to reduce the pressure in, and downstream of, the residual ion dump and hence the re-ionisation of the neutral fraction of the beam in that region and in the duct leading to the reactor vessel. That is important as re-ionised particles will be deflected into the walls of the duct by the stray magnetic field from the reactor, reducing the injected power as well as heating the duct walls. The latter is important as removing heat deposited in the duct leads to water-cooled components in the duct, and those may occasionally require maintenance. As those components will become highly active during operation of the reactor, such maintenance will only be possible by remote means, which is inherently complicated and difficult. Reducing the power load means that the components can be designed with a high safety factor, leading to less, perhaps no, maintenance in the lifetime of a reactor.

Cryopumps that “wallpaper” each side of the injector beamline vessel can provide a sufficient pumping speed for D_2 , which in the ITER heating injectors is $\approx 3 \times 10^6$ l/s [12]. Gas is not removed from an injector by cryopumps, it is simply frozen on the cryogenically cooled panels of the pumps, and the quantity of D_2 that can be stored on the pumps is limited because of the possible explosion; if the D_2 is released from the pumps, there is sufficient oxygen inside the injector, and a source

of ignition is present. Although the risk is low, it is not acceptable, especially in the case of a reactor where the injector is part of the confinement barrier. Consequently, when the gas storage limit is reached, it is necessary to regenerate the pumps, i.e. to release the stored D_2 , and pump it away with an external pumping system. As several injectors are likely to be installed on a reactor in order to provide the required total heating and current drive power, continuous provision of the required power can be assured by installing one “excess” injector. Then if the n injectors are installed, $n - 1$ injectors provide the required power, and only $n - 1$ are usually operating. That allows the non-operating injector to be isolated vacuum wise from the reactor and to be regenerated, with each injector being regenerated in turn. That only works if the regeneration time¹ is $\leq \tau / (n - 1)$ hours, where τ is the time for which each injector can operate before regeneration is needed. As an example, assume that the injectors can be regenerated in 1.5 h and that each injector can operate for >3 h before needing to be regenerated. Then with three injectors installed on the reactor, one is regenerated each hour, so that the cryopump of each injector is regenerated after 3 h of operation; all three injectors are regenerated after 4.5 h, and the cycle is then repeated, as shown in **Figure 1**. Having an “extra” injector is expensive, both because of the cost of the injector and the additional cost of operating the extra injector and because it reduces the efficiency of the reactor as the wall space needed for the extra injector cannot be used for generating power.²

In the example given above, the injectors would have to operate >3 times longer than permitted for the ITER injectors, so that, all other things being unchanged, the total gas flow into the injectors on the reactor would have to be reduced by a factor 3 compared to the gas flow into the ITER injectors, and that must be achieved without degrading the injector performance or the global injection efficiency.

An alternative to having an extra injector is to instal a higher pumping speed than is required for the efficient operation of the injector and to be able to regenerate the “unnecessary” part of the cryopumps in situ. For example, if the installed pumping speed were twice that required for the efficient operation of the injector, then half the pump could be shut off from the injector, whilst the other half continues to operate; once the first half has been regenerated, that can be opened up to the injector and the second half closed off for regeneration and so on.

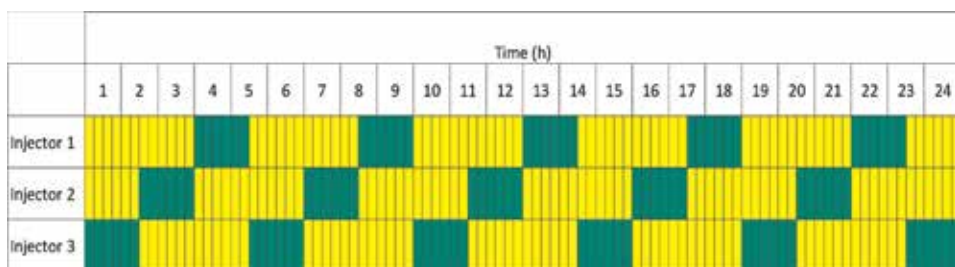


Figure 1. Schematic of the regeneration cycle for a neutral beam system with three injectors installed, with each injector capable of operating for >3 h before regeneration of the cryopumps being necessary. The yellow areas indicate that the injector is operational and the green ones that it is being regenerated. Two injectors are always operational.

¹ The regeneration time consists of the time to isolate the injector from the fusion device, warming up the cryopumps to the release the gas, pumping down the injector and cooling down the cryopumps, plus the time to recondition the injector.

² If a reactor costs 2×10^9 €, and the apertures in the blanket for the injectors take up 1% of the wall space, the cost of not producing power from that fraction of the wall is 2×10^7 €, i.e. 66 M€ per injector.

Unfortunately no system for closing off part of a cryopump sufficiently to allow it to be regenerated whilst the rest of the pump continues operation has yet been developed.

In the above discussion, it is assumed that cryopumps will be used in the NB injectors. It has been suggested that non-evaporable getters (NEGs) could be used instead of cryopumps. NEGs have an advantage that no sudden release of the gas captured by the getters is possible; thus there is no safety hazard associated with the storage of large quantities of D₂ in the getters. If NEGs are to be considered, a viable assembly of NEGs needs to be designed, using NEGs that will not be poisoned by any impurities in the NB injector and, obviously, that the assembly needs to provide the required pumping speed. However the problem of regeneration of the pumps remains as NEGs do not actually pump the D₂ out of the injector, but they trap it within the getter material, and regeneration is needed once the NEGs become saturated with D₂. The possible ways to overcome the lack of pumping during regeneration are, in essence, the same as suggested for cryopumps above. However the regeneration time for NEGs is expected to be several hours, so that with three injectors installed on the reactor, as in the above example with cryopumps, the NEGS would have to operate for 10 h if the regeneration time is 5 h. No design of such a system has yet been done.

Because of the quasi-continuous operation of the injectors, all the gas used for the injectors will be gas recovered from the gas recycled through the reactor "tritium plant". That must include the gas released from the injector cryopumps as that will be contaminated with T₂ that has flowed to the injectors from the reactor. However, the gas flowing into the ion sources must contain only a small fraction of T₂ to make sure that the neutral beams will have a negligible fraction of T⁰ as the lower velocity of T⁰ would lead to deposition in the plasma of the reactor nearer the outside of the plasma which is undesirable.³ The requirement to have fairly pure D₂ for the ion source operation impacts directly on the design of the tritium plant, which could lead to substantial cost increase for the tritium plant, and therefore any reduction in that gas flow is highly desirable.

It is to be noted that some of the He produced in the fusion reactions will flow into the neutral beam duct and the injector, adding to the gas density in the duct. That will increase the fraction of the neutral beam that is re-ionised by collisions with the gas in the duct and thus the power to the duct walls. The density of He in the duct and the injector must be kept at a level that the He in the ion source does not compromise its performance and that the He density in the beamline and the neutral beam duct does not significantly enhance re-ionisation losses. An estimate of the density in the ion source and the increase in re-ionisation loss due to the presence of He in the injector and duct is given below:

Assume that a 1 MeV D beam is being injected into the reactor.

If the pumping speed for He in the injectors is zero, the He density in the duct between the injector and the reactor will rise until the flow out of the duct into the reactor is equal to the flow from the reactor into the duct. Assuming that the He temperature in the duct is 100°C (due to collisions with a 100°C duct wall), that the gas flow out of the reactor into the injector duct is $\approx 10^{20}$ atoms/s (a value calculated for the plasma in ITER), and that 10% of the outflow is He (the rest being D and T), the density of He in the duct will be $\approx 2.5 \times 10^{16} \text{ m}^{-3}$.

³ T₂ in the source may also impact on the source performance. Operating in D₂ is known to result in a higher fraction of co-extracted electrons compared to operation in H₂, and it is possible that the electron fraction with T₂ is even higher.

Now the He flow out of the injector into the duct must be equal to the flow into the injector from the duct. Assuming that the He temperature in the injector is 20°C (due to collisions with water-cooled components in the injector), then the gas density in the injector will be $\approx 2.8 \times 10^{16} \text{ m}^{-3}$.

Re-ionisation loss occurs between the entrance to the residual ion dump and the entrance into the reactor. The cross section for re-ionisation of D on He is $\approx 3 \times 10^{-21} \text{ m}^2$. Assume that the length of the duct between the injector and the reactor is 10 m and that the length of the residual ion dump plus that of the beamline calorimeter is 3.5 m. Then the extra re-ionisation loss due to the presence of He in the system is calculated to be $\approx 0.1\%$.

If the He temperature in the ion source is 1200 K (the gas temperature in a negative ion source of the type to be used in the ITER injectors has been measured to be 1200 K), then as the He flow into the ion source from the beamline must equal the He flow out of the source, the He density in the ion source will be $\approx 1.6 \times 10^{16} \text{ m}^{-3}$. To put that in perspective, the D₂ density in the ion source should be of the order of $6 \times 10^{18} \text{ m}^{-3}$, that is, the He will represent $< 0.25\%$ of the gas particles in the ion source.

In conclusion, the small increase in the re-ionisation loss due to the presence of He in the injector and the duct of $\approx 0.1\%$ is almost certainly acceptable. The presence of an He density of significantly above $\approx 1.6 \times 10^{16} \text{ m}^{-3}$ has been shown experimentally not to have any significant effect on the source performance [13].

4. Caesium (Cs) “consumption”

It is currently estimated that Cs will need to be injected into each ion source at a rate of $\approx 20 \text{ mg/h}$ in order to reach the required extracted negative ion current. With quasi-continuous operation and that Cs injection rate, $> 1 \text{ kg}$ will have been injected into each source every 6 years. It has been found that most of the injected Cs remains in the ion source and significantly less than 1 kg of Cs is almost certain to cause operational problems. There are three possible ways to overcome this problem:

- i. Develop a technique for cleaning Cs from an ion source by remote means, so that cleaning of the source can be done during a reactor maintenance period;
- ii. Reduce the required Cs injection rate by about a factor 20 so that Cs accumulation in the source does not become a problem during the reactor lifetime;
- iii. Develop an alternative to Cs (see is section 2.1.1.3 above).

5. Operation and maintenance in a nuclear environment

The injectors will be operating in a very hostile nuclear environment, and that will have an impact on many aspects of the NBI system, for example, the activation and transmutation of materials, the requirement to maintain confinement barriers under operational response and accidental scenarios, etc., and the necessity to meet all nuclear safety requirements. A particularly important aspect of operating in a nuclear environment is that all the components in the actual injectors and the injector vessel and the nuclear shielding around the injectors will become activated during operation; that no human intervention for maintenance operations will be

possible, so all maintenance must be carried out remotely; and that requirement must be considered at all stages of the design of the injection system.

5.1 Component lifetime

The lifetime of fusion reactors must be very long, and similar to that of a fission reactor, for example, >40 years, and, like fission reactors, they will operate continuously between outages for maintenance, which will occur not more frequently than yearly, and the outage time has to be as short as possible, for example, <1 month, see, for example [14]. The time that the NBI system on a reactor must operate, both in total and between maintenance periods, is orders of magnitude beyond any NBI system designed so far, and that means that many new considerations enter into play, such as the lifetime of components which are subjected to sputtering by the beams and thermal fatigue. It is also evident that as the reactor and the injectors will operate for 1 year or more between maintenance periods, any component that is designed to be replaced routinely must be able to operate for more than 1 year before the replacement becomes necessary.

5.2 Lifetime and fatigue

The injector components should be designed to have a fatigue life that is greater than the life of the fusion reactor, that is, about 40 years with essentially continuous operation. When there is a breakdown in the accelerator, the beam will be re-established in ≈ 180 ms, which is short compared to the thermal response time of the components, and the components “see” only a small part of a thermal cycle. Therefore fatigue failure will arise from the on-off cycles of the beam, when the components will experience the complete thermal cycle. The number of on-off cycles will probably be dominated by the regeneration cycle of the cryopumps. With a photon neutraliser and a gas flow into the ion source that is reduced by a factor 3, the cryopumps should be regenerated after ≈ 3 h of operation (see **Figure 2**). As, with continuous operation of the reactor, ≈ 3000 regenerations will be needed per year, there will be $\approx 1.2 \times 10^5$ cycles in the reactor lifetime, 40 years. The injector will almost certainly require conditioning pulses after a regeneration in order to regain full performance. The low power operation used at the start of the reconditioning does not contribute significantly to fatigue, and about five full power pulses should suffice to complete the conditioning. Thus the injector components will “see” $\approx 6 \times 10^5$ full thermal cycles in the reactor lifetime.

The relatively low extracted current assumed above, together with the reduction in the stripping losses by a factor 3 (due to the reduced source gas outflow), means that the power load to the grids should be easily handled and fatigue should not be a problem. Similarly, the power to the residual ion dump will be quite low because of the high neutralisation expected with a photon neutraliser and designing the residual ion dump to have the required fatigue life not be a problem. The reduced gas flow into the injector will significantly reduce the re-ionisation loss, hence the loads to the panels in the duct leading to the reactor, and fatigue should not be a problem. However, even in the reduced current density design considered in Section 1.2, the beamline calorimeter, which is essential for the commissioning and recommissioning of the beam source, will receive a similar power density to that received by the calorimeter of the heating neutral beams of ITER, and the fatigue life of the optimised design of that component is calculated to be $\approx 7.5 \times 10^4$ cycles, so either a non-negligible improvement of the design is needed or the calorimeter will have to be replaced after about 20 years, i.e. once in the lifetime of the reactor.

It is worth emphasising that, as assumed above, it is reasonable to conclude that the power “seen” by the beamline calorimeter of an injector on a reactor cannot be higher than that “seen” by the calorimeter of the heating injectors of ITER, which precludes increasing the accelerated D^- current density to $>100 \text{ A/m}^2$ when a high efficiency neutraliser is used. Another consequence is that any increase in the beam energy would necessitate a decrease in the accelerated current density in order to keep the power to the calorimeter at the acceptable level.

5.3 Space limitations

High-power, high-energy neutral beam injectors are large; for example, the ITER 1 MeV heating injectors are $\approx 15 \text{ m}$ long and $\approx 4 \times 4 \text{ m}$ in cross section, and the high voltage bushing through which connects the power, gas, and water cooling to the beam is over 6 m tall and 2.5 m in diameter (see **Figure 2**).

Obviously the injectors will require a large “neutral beam cell” somewhere around the reactor, which must also provide space around the injectors for nuclear and magnetic shielding, and, because the injectors on a reactor will become radioactive, space for the remote handling equipment needed for all maintenance on the injectors. Space around the reactor will also be required for many other types of equipment, and the space for the injectors will inevitably be limited, which will directly influence the design and layout of the injectors and any attachments to the injectors. Some appreciation of the likely space constraints can be gained from the ITER system. The layout of the three heating and one diagnostic neutral beam injectors is shown in **Figure 3**.

5.3.1 Heating power

The three ITER heating neutral injectors will be capable of injecting “only” 50 MW of D^0 into ITER, and significantly higher power may be required on a reactor. If that is realised by adding more injectors, an even larger neutral beam cell will be required. However that might be avoided by increasing the power from each injector, which might be achieved by having a more uniform power density on the calorimeter. In principle, that might be possible as the geometric limitations associated with the gas neutraliser used in the ITER injector would not apply to a photon neutraliser-based system. However that requires detailed considerations of the injector design, and those are not possible with the present state of development of the photon neutraliser.

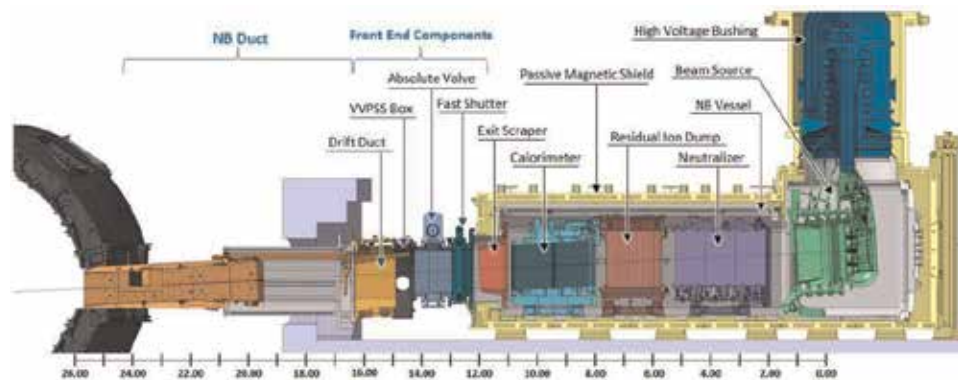


Figure 2. Computer-generated cut-away view of an ITER HNB beamline. The scale below the beamline shows the distance along the beamline axis in metres from the last grid of the accelerator.

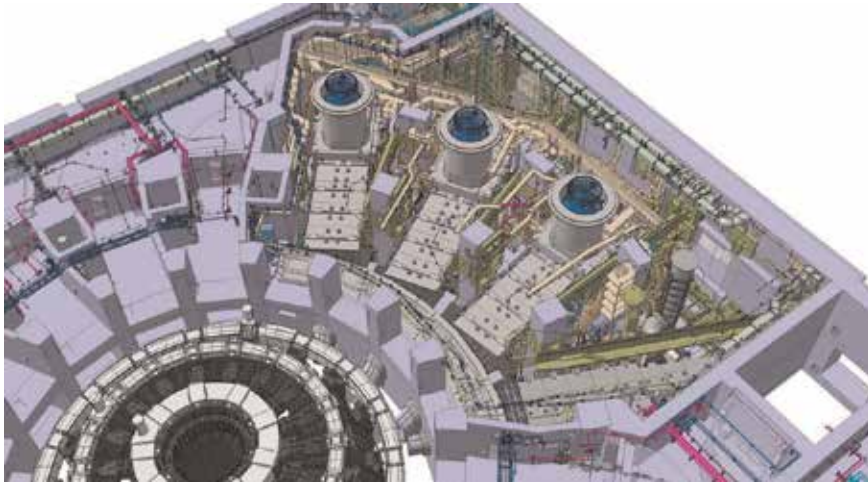


Figure 3.
Computer view of the ITER NB cell with three heating neutral beam injectors and a diagnostic neutral beam injector installed. The three heating neutral beam injectors should be capable of injecting 50 MW into the ITER plasma.

5.4 Operation in a nuclear environment

The injectors at ITER are expected to perform in a harsh nuclear environment which will not be better on a reactor. In the present scheme of things, the injectors are an extension of the vacuum vessel and therefore a part of the nuclear confinement barrier. It is therefore essential that their integrity is assured for all situations including normal and accidental events which can be initiated when the machine operates.

The design and operation of injectors in a nuclear environment need to be considered from various aspects such as the engineering design codes used, the injector materials, their layout, their operational response to normal and accidental scenarios under various load conditions, and maintenance, including remote handling, tooling, and the deployment of remote handling tools. All those have been addressed for the ITER injectors, and the impact on the design has been very significant. Some of the various aspects are discussed below in order to give an idea of the complexity involved in adapting the systems to nuclear environments.

5.4.1 Materials

Operation in a radiation environment impacts the choice of materials used for components, such as to ensure that the essential material characteristics are not modified by irradiation and to reduce the degree of activation and the quantity of activated waste. This impacts on all parts of the injector, including, for example, the choice of vacuum seals, where, essentially, only all metal seals are accepted, the joining techniques for similar and dissimilar materials, etc. The definitions for reactors will be stringent because of the harsh environment and strict safety standards that will be applied. Radiation can damage electronics, components, and sensors, corrupt signals, and make optical fibres and windows become opaque. These effects can appear instantaneously or over a period of time due to an accumulation of, for example, atomic displacements. It is clear that the design of an injector designed to operate on a reactor will have to ensure that all electronics are situated in low radiation areas, as has been done for the ITER design, both to ensure their lifetime is adequate and to allow their maintenance.

5.4.2 Injector layout

Designing a system for the environment of a reactor requires a serious consideration of the layout of the injectors, ensuring good access for the remote handling tooling and adequate shielding in case of the need for man access. Meeting these requirements requires sufficient space, but there is a conflicting requirement, which is to keep the “nuclear island” as small as possible. The latter means that the location of the inventory, the first confinement boundary, is confined to as small an area as possible. The vacuum boundary of the machine, in normal operation, defines the first confinement barrier, and any penetration through the barrier becomes part of the first confinement barrier. To ensure reliability and safety, it is likely that two metal valves will need to be installed, in series, upstream of any penetration of the barrier, as is the case on ITER. In that case, the vacuum boundary of the machine and the second valve, which is the last layer of the primary confinement barrier, defines the nuclear island. To minimise the size of the nuclear island, the valves and windows must be located as close as possible to the machine. This can lead to a complex design which must tolerate high radiation loads, heat loads, neutron fluxes, and electromagnetic loads whilst simultaneously fulfilling the safety function of primary confinement. An example of the impact on the injector design is that this means that any guide tubes for the laser light used for the photon neutraliser will need to incorporate a window in series with a valve close to the injector vessel. That window will have to meet all the requirements of the first confinement barrier and vacuum boundary as well as be able to transmit the laser light quasi-continuously. As some laser power will be absorbed by the window, it is probable that the window will need to be cooled by some type of cooling system. Also the window must be capable of withstanding any over pressure or heat load that might occur during the failure inside the reactor.

5.4.3 Operational response to normal and accidental scenarios

To ensure safe operation of injectors on a reactor, all possible accidental events will have to be analysed under all possible load conditions including those arising from abnormal plasma events such as a “vertical displacement event” (VDE),⁴ and under all conditions, i.e. when the system is operating, in stand-by or being maintained. In addition, nuclear analyses will have to be performed to confirm that radiation damage to the materials will be below the level at which the mechanical properties are compromised.

5.4.4 Remote handling

Operation in a nuclear environment limits direct access and hands on maintenance as the injector will become radioactive, and there are then hazards related to exposure to radiation and from inhalation of airborne contamination. The expected level of radioactivity in the ITER NB cell and the defined radiation zoning of the facility lead to the need for remote handling to be in place. Human access is only allowed when the dose rates are kept beneath the allowed limits of <100 µSv/h.

⁴ In some magnetic confinement devices loss of control of the plasma position can result in a rapid vertical movement of the plasma, leading to a violent disruption (sudden loss of the plasma), which is known as a vertical displacement event. The consequent release of the energy that was stored in the plasma can lead to very strong, potentially damaging, forces being applied to the machine.

Achieving the compliance with the radiation zoning is carried out by the use of effective shielding in the design of the components and reducing materials which are more activated, i.e. using low cobalt content stainless steel, but achieving a similar situation on a reactor will be difficult.

6. Discussion and summary

6.1 Efficiency increase

A global efficiency of $\approx 60\%$ or better is required for a neutral beam system on a reactor, which is much higher than any neutral beam system has achieved so far. Meeting that requirement represents a major challenge for neutral beam development. To do so requires both a significant increase in the neutralisation efficiency and a decrease in the losses in the system.

- Increasing the neutralisation efficiency appears most feasible, if difficult, with a photon neutraliser. The only identified alternative is a plasma neutraliser plus energy recovery. However, work so far carried out on this topic has failed, by a wide margin, to produce an adequate D^+ and D_2^+ + electron plasma target⁵ nor to demonstrate how to produce a plasma confinement system that allows the transmission of the beam through the neutraliser that does not degrade the beam emittance. Additionally recovering the energy from the D^+ fraction of the beam leaving the neutraliser has severe difficulties and has not been demonstrated [15–17].
- The stripping losses in the extractor and accelerator of the beam sources of the ITER heating injectors are very high ($\approx 30\%$) and must be reduced. That can only be achieved by reducing the gas flow out of the source into the extractor and accelerator, which would also reduce the back-streaming in power into the ion source and the sputtering from the ion source backplates.
- Solid-state RF power supplies have an efficiency of $\approx 85\%$ and must be used for injectors on a reactor that use RF-driven ion sources.

6.2 Low work function PG surface

Sputtering from the ion source backplates by the back-streaming ions means that the PG surface will be coated in the sputtered material in a time that is very short compared to the operational time between the reactor maintenance periods. That will result in an increase of the work function and a significant reduction in the extracted ion current. Thus either the PG needs to be replaced or the surface renewed. Replacing the PG is not reasonably possible with the current type of accelerator design. Therefore R&D into low work function PG surfaces should not be prioritised. However the continued use of Cs injection means that:

⁵ In principle other gases could be used in the plasma neutraliser, such as argon (Ar), and it is easier to obtain a higher ionisation degree with Ar [18]. However the potential problems that might occur with Ar such as contamination of the tritium plant and Ar^+ back-streaming into the ion source need to be evaluated, which has not been done.

- The Cs flow into the source must be significantly reduced to avoid excessive Cs accumulation in the source, and ways of in situ cleaning the source of Cs needs to be developed (see Section 1.1.2).
- Preliminary estimates indicate that back-streaming Cs⁺ may cause significant sputtering of the ion source backplates, adding to the erosion by back-streaming D₂⁺. Therefore the Cs density in the extractor must be reduced via a reduction in the Cs in the in source plasma, and R&D on easily exchangeable ion source backplates may be essential.

6.3 Long pulse operation

Meeting the pumping requirements of the injectors during very long pulse operation is very difficult, even with a substantial reduction of the gas flow into the ion source and no gas into the neutraliser. The only systems that can provide the required pumping speed are cryopumps, and possibly non-evaporable getters (NEGs), and neither of those actually pumps gas out of the injector. Consequently, such pumps require regular regeneration to avoid possible explosions and/or to avoid saturation of the pumps. As no way has yet been developed to allow an injector to continue operation whilst the pumps are regenerated, the only option is to take the injector off-line during the regeneration. That problem could be overcome by having one “excess” injector, so that of the n injectors installed, only $n - 1$ injectors are ever operating, and each injector is regenerated in turn.

6.4 Lifetime and fatigue

Because the beamline component will become activated during the operation of the reactor, any maintenance or exchange of the components will have to be done remotely, and all such operations will be very difficult. That consideration leads to the requirement that all the components must be designed to have an expected life that is longer than that of the reactor, for example, with a fatigue life of >40 years. The calorimeter of the injectors of a reactor will “see” a similar thermal load to that of the calorimeter of the ITER injectors, even though the accelerated current density is reduced by 50% of that expected with the ITER system. The ITER calorimeter design was extremely challenging, and it is unlikely that the design of the calorimeter of the injectors on a reactor will be significantly better. The calorimeter of the ITER injectors has a calculated fatigue life of 7.5×10^4 thermal cycles, and R&D is needed to meet the full fatigue lifetime requirement which could be $\approx 5 \times 10^5$, i.e. 8 times higher.

6.5 Nuclear environment

The injectors on a reactor will have to fit into the available space, and they will have to minimise their impact on the size of the nuclear island. The resulting space constraints will impact on the design and the layout options of the injectors and any attachments to the injectors, and the requirement that all maintenance must be carried out by remote means, with the consequent need for space around the injectors for the remote handling equipment, must be taken into account during the design of the injectors. An obvious conclusion is that in order to be considered for R&D funding, any proposal for R&D should consider the possible implications of the nuclear environment and propose conceptual solutions to those implications.

Disclaimer

The views and opinions expressed herein do not necessarily reflect those of the ITER organisation.

Author details

Ronald Stephen Hemsworth^{1*} and Deirdre Boilson²

1 Ensue la Redonne, France

2 ITER Organization, Route de Vinon-sur-Verdon, St. Paul Lez Durance Cedex, France

*Address all correspondence to: rshemsworth@gmail.com

IntechOpen

© 2019 The Author(s). Licensee IntechOpen. This chapter is distributed under the terms of the Creative Commons Attribution License (<http://creativecommons.org/licenses/by/3.0>), which permits unrestricted use, distribution, and reproduction in any medium, provided the original work is properly cited. 

References

- [1] Pilan N, Antoni V, De Lorenzi A, Chitarin G, Veltri P, Sartori E. A new deflection technique applied to an existing scheme of electrostaticv accelerator for high energy neutral beam injection in fusion reactor devices. *Review of Scientific Instruments*. 2016; **87**:02B325
- [2] Sonato P, Agostinetti P, Fantz U, Franke T, Furno I, Simonin A, et al. Conceptual design of the beam source for the DEMO Neutral Beam Injectors. *New Journal of Physics*. 2016;**18**:125002
- [3] Simonin A, de Esch HPL, Garibaldi P, Grand C, Bechu S, Bès A, et al. Ion source development for a photoneutralization based NBI system for fusion reactors. *AIP Conference Proceedings*. 2015;**1655**:050002. DOI: 10.1063/1.4916459
- [4] Duesing G, Altmann H, Falter H, Haange R, Hemsworth RS, et al. Neutral Beam Injection System. *Fusion Technology*. 1987;**11**:163-202
- [5] Hemsworth RS, Feist J-H, Hanada M, Heinemann B, Inoue T, Kussel E, et al. Neutral beams for ITER. *The Review of Scientific Instruments*. 1996;**67**(3): 1120-1125
- [6] Hemsworth RS, Boilson D, Blatchford P, Dalla Palma M, Chitarin G, de Esch HPL, et al. Overview of the design of the ITER heating neutral beam injectors. *New Journal of Physics*. 2017;**19**:025005
- [7] Pamela J, Bécoulet A, Borba D, Boutard J-L, Horton L, Maisonnier D. Efficiency and availability driven R&D issues for DEMO. *Fusion Engineering and Design*. 2009;**84**:194-204
- [8] Kraus W, Fantz U, Heinemann B, Franzen P. Solid state generator for powerful radio frequency ion sources in neutral beam injection systems. *Fusion Engineering and Design*. February 2015; **91**:16-20
- [9] Taniguchi M, Hanada M, Iga T, Inoue T, Kashiwagi M, Morisita T, et al. Development of high performance negative ion sources and accelerators for MeV class neutral beam injectors. *Nuclear Fusion*. 2003;**43**:8
- [10] Singh MJ, De Esch HPL, Hemsworth R, Boilson D. Mo layer thickness requirement on the ion source back plate for the HNB and DNB ion sources in ITER. *AIP Conference Proceedings*. 2015;**1655**:040007
- [11] Hemsworth RS. Private communication. A technical note detailing those calculations may be obtained from D Boilson. 2015
- [12] Dremel M, Day C, Hemsworth R, Pearce R, Mayaux C. Cryopump design for the ITER heating neutral beam injector. *Nuclear Fusion*. 2009;**49**: 075035
- [13] Fantz U, Garching IPP. Private communication. 2015
- [14] Available from: <https://www.fe.nvoimo.fi/en/hanhikivi-1/nuclear-power-plant-maintenance>
- [15] McAdams R. Beyond ITER: Neutral beams for a DEMOnstration fusion reactor (DEMO). *Review of Scientific Instruments*. 2014;**85**:02B319
- [16] McAdams R, Holmes AJT, Porton M, Benn A, Surrey E, Jones TTC. Advanced energy recovery concepts for negative ion beamlines in fusion power plants. *AIP Conference Proceedings*. 2013;**1515**:559
- [17] Kulygin VM, Skovoroda AA, Zhil'tsov VA. Plasma neutraliser for

ITER NBI. Plasma Devices and Operations. 1998;**6**(1-3):135-147

[18] Kulygin VM, Dlougach ED, Gorbunov EP, Klimenko EY, Mehed'kin AA, Panasenkov AA, et al. The next step in a development of negative ion beam plasma neutralizer for ITER NBI. Nuclear Fusion. 2001; **41**(4):355-362

Taxonomy of Big Nuclear Fusion Chambers Provided by Means of Nanosecond Neutron Pulses

Vladimir Gribkov, Barbara Bienkowska, Sławomir Jednorog, Marian Paduch and Krzysztof Tomaszewski

Abstract

A methodology is elaborated and applied to taxonomy of large chambers of thermonuclear fusion reactors. It ensures a feasibility to describe impairments produced by environment and details of the chamber into the neutron field generated during the operation of a reactor. The method is based on application of very bright nanosecond neutron flashes irradiated from a compact neutron source of a dense plasma focus type. A number of neutron activation procedures as well as a neutron time-of-flight method were applied to trace deviations of neutron 3-D fields after their interaction with the simulator of the above chamber. Monte-Carlo modeling of these processes gained the data on the most important elements that influenced on the fields.

Keywords: nuclear fusion reactors, dense plasma focus, nanosecond neutron pulses, neutron activation diagnostics, time-of-flight spectral diagnostic

1. Introduction

Contemporary and future nuclear fusion reactors are of rather sophisticated assemblies positioned in intricate surroundings. Elements of their environment and constructions may absorb and scatter the basic fusion energy carriers—neutrons [1].

The contemporary main-stream nuclear fusion installations using magnetic and inertial plasma confinement, namely: Joint European Torus (JET, U.K.) [2], Wendelstein 7X Stellarator (W7X, Germany) [3] (in the nearest future—the International Thermonuclear Experimental Reactor (ITER) [4]), the powerful laser devices Iskra-5 (in future Iskra-6, R.F.) and National Ignition Facility (NIF, U.S.A.) [5] as well as the Z-Machine [6] (Jupiter expected in future [7], U.S.A.)—generate around their chambers 3-D neutron fields that are distorted at their irradiation outside. The elements of the sheds, numerous structures of the Nuclear Fusion Chambers (NFC), power sources as well as specific apparatus belonging to these parts of the facilities exemplify scatterers and absorbers irradiated by neutrons. So produced by the fluctuations (“voids” and “hot spots”) in neutron intensity and in spectra around the NFC must be taken into account at the interpretation of the operational results. The neutron intensity changes and spectra imperfections observed out of NFC because of elastic and inelastic neutron scattering may happen

even at an absolutely isotropic initial expansion of neutrons into space from a source with symmetric nuclear fusion neutron spectral content (e.g., from a laser target in a laser fusion facility or from an element of the toroidal plasma ring in a tokamak).

But there is an opportunity to describe a 3-D neutron field formed around a nuclear fusion chamber before its full-scale operation with a help of a foreign powerful point neutron source that has pulse duration in a nanosecond (ns) range. Indeed the intense short neutron flash will allow attributing and describing all elements of a NFC that absorb and/or scatter neutrons separately by using measurements of neutron fluxes (with neutron activation methods) and spectra (with photomultiplier tube plus plastic scintillator—PMT + S—by means of time-of-flight (TOF) method) in all directions. These two procedures will also be important from the point of view of the radiation material science: they will give information where one may expect increased or diminished values of *dpa* in the plasma-facing and construction materials of a NFC.

A very intense ns neutron pulse irradiated from a tiny volume (about 1 cm^3) can be generated by a nuclear fusion device named dense plasma focus (DPF) [8]. Moreover, its neutron emission is quasi-mono-energetic one. So by means of this device, one may have an opportunity to distinguish elastic scatterings produced by different parts of a chamber or by dissimilar chemical elements of their content. DPF may also be used in time-of-flight technique for spectra measurements with a moderate path length.

Nuclear fusion reactions in a DPF are produced at the interaction of self-generated and magnetized fast deuterons with pinched plasma [8]. It is similar to the process taking place in tokamaks with an external neutral beam heating of its plasma. Accelerated fast deuterons have spectrum spreading to MeV range and peaked at hundreds keV. The DPF device may be exploited with *D* or *D-T* mixture as working gases. In these cases, it will produce neutrons with mean energy at around 2.5- or 14-MeV energy peaks correspondingly as it is so in the contemporary main-stream NFCs. With these ns neutron pulses, a majority of materials used in activation technique will have the activation time much shorter compared with the time of their radioactive decay.

Nanosecond neutron pulses are irradiated from the DPF chamber into space as a neutron “shell” (Figure 1a) of a finite thickness. It has almost a spherical shape. The thickness of the shell (i.e., a space between the surfaces *A* and *B* of the sheath filled

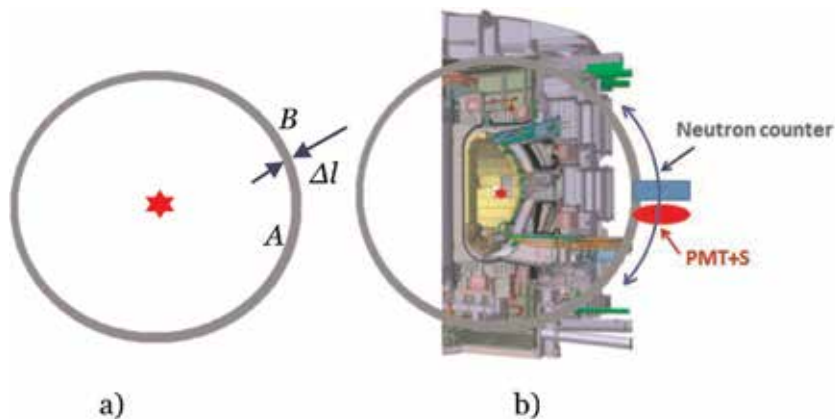


Figure 1. A neutron “sheath” (a) irradiated from a compact neutron source (shown by a star) of an ns pulse duration having a thickness in space Δl given by formula (1); its possible use (b) in a large main-stream NFC (a sketch of a cross-section of the ITER chamber is here).

with neutrons) has a value Δl equal to pulse duration of neutron radiation Δt multiplied by neutron speed v :

$$\Delta l = \Delta t \times v \quad (1)$$

This sheath during its propagation from the compact source outwards will be distorted because of absorption and scattering on elements and systems belonging to a NFC. Thus, such a source can be able to uncover each element of a NFC producing the above-mentioned distortions during neutron radiation expansion through the chamber components (**Figure 1b**).

These alterations may be found in data on the absolute neutron flux measured in certain 3-D points in the exterior of the chamber. It will also be discovered as confident modifications in a neutron temporal evolution in time and, consequently, in neutron spectral composition after their transit through elements and systems of the nuclear reactor.

The spatial thickness of the above neutron “shell” will have a value of about 10 of cm being much less compared with the main construction elements of a NFC of a main-stream fusion facility. Thus, for the taxonomy of objects by such a bright

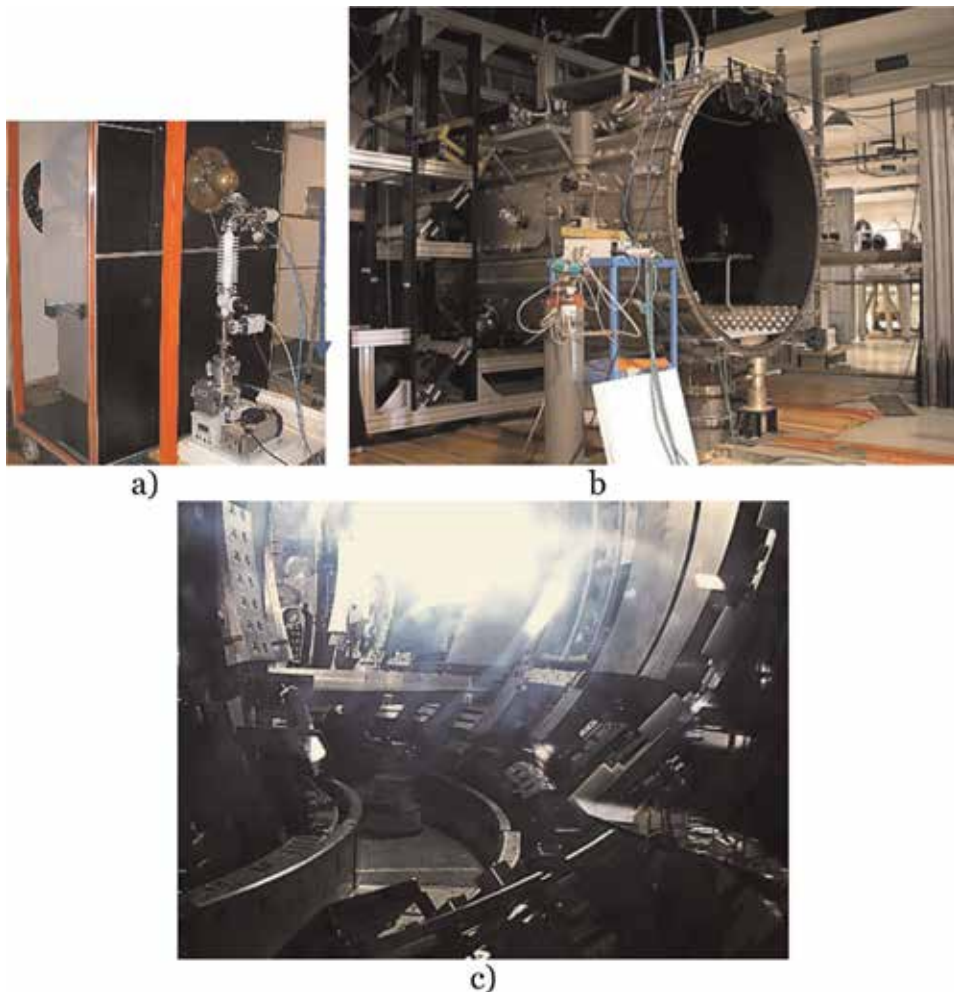


Figure 2. Dense plasma focus device PF-6 (a) and a big chamber of the PF-1000U facility (b), simulating a section of a main-stream fusion chamber of a present-day tokamak (JET here) (c).

short-pulse neutron radiation, one may use elastic and inelastic scattering of neutrons upon nuclei of unknown elements. It is evident that this short powerful neutron flash allows using TOF technique with short flight bases for modern NFCs.

This type of measurements can be provided by positioning of a DPF-based compact neutron source in the center of the spherical chamber used in laser fusion facility or at the movement of this neutron source along the circumference of the toroidal chamber of a modern fusion device with magnetic plasma confinement. Such characterization procedures should preferably be repeated after each important stage of assembling of a new main-stream fusion facility to describe its novel elements and their influence on neutron field.

Here in the very beginning, we shall observe the activation methods applied by using ns neutron pulses generated in a DPF device PF-6 (**Figure 2a**) due to $D-D$ reactions. Thus, the generated in the device 2.5-MeV neutrons are subjected mainly to elastic scattering on parts and structures of a simulator of a NFC [1]. Then later, a neutron spectroscopic technique will be talked over.

In this case, we exploit in the capacity of the simulator of a big NFC a large chamber that belongs to the PF-1000U facility [9] available at the Institute of Plasma Physics and Laser Microfusion (**Figure 2b**), Poland. This chamber looks quite similar to the section of JET tokamak (U.K.)—**Figure 2c**. The vacuum chamber of the PF-1000U device has a shape of a large cylinder with walls made of stainless steel. The discharge circuit of the chamber consists of a set of capacitors, cables, and spark-gaps connecting the battery with cylindrical concentric electrodes playing the role of a plasma accelerator.

2. The PF-6 device as a compact ns-pulsed neutron source and its auxiliary facilities

2.1 PF-6 device

This machine (**Figure 2a**) has been described in a number of papers (see e.g., [1, 10–12]). Its battery charged to 12–20 kV contains up to 6 kJ of energy. Typical range of initial pressures of pure deuterium in the device in this configuration was in the range from 2 to 8 Torr. Amplitude of a discharge current of the device measured by a Rogowski coil reaches 0.7 MA. The definition of the device as a neutron source (its major parameters that were measured many times) is as follows:

- Neutron emitting plasma volume is less than 1 cm^3 ; so it is much smaller compared with a several-meter characteristic size of a main-stream NFC elements and systems; thus it may be counted as a point very bright mono-energetic source.
- Quasi-mono-energetic spectra of neutrons are different to some extent being measured at dissimilar angles to Z-axis of the device; they are peaked near the energy about 2.5 MeV with the narrow spectrum near it: $\Delta E_n/E_0 \approx 3\text{--}5\%$, where ΔE_n —full width of neutron energy distribution function at its half maximum (FWHM), and E_0 is an energy value where the peak of neutron energy distribution is observed in a particular direction.
- Neutron yield is $10^8\text{--}10^9$ neutrons/pulse with the deuterium chamber filling and about two orders of magnitude higher for the $D-T$ mixture as a working gas.

- Pulse duration is in the range 15–20 ns, that is, a “thickness” of a quasi-spherical neutron “sheath” (**Figure 1a**) spreading into a space from the source has its value of about 10 cm. In other words, 10 cm is the length of the neutron packet coming to a detector from the neutron source. Thus, the DPF source irradiates an ns neutron pulse to a detector as a neutron bunch with a size much smaller than the characteristic dimensions of the elements and systems of a NFC.

A DPF is an ecologically more acceptable radiation-producing device in comparison with another neutron sources like the accelerators, fission reactors, and isotope-based sources because:

- Its battery charging voltage is relatively low (~10 kV).
- The DPF is a so-called “push-button source” because it irradiates neutrons during several nanoseconds merely at switching it on.
- It does not demand safe containers for the device’s protection.
- This set-up can be supplied with a sealed chamber having a $D-T$ gas mixture generator with a heater discharging the gas into the chamber’s volume [13].

In **Figure 3**, the oscilloscope trace of the current derivative of a typical “shot” (discharge) of the device is presented. Chambers that have been used in this device were of two types (small and large) designed and manufactured at the VNIIA. With the last one, it may be sealed, obeying a gas generator with deuterium-tritium mixture and produce the 14-MeV neutrons with the yield up to 10^{11} neutrons of 15–20 ns time duration.

2.2 Activation methodology

A silver activation counter—SAC [1] (in fact two of them—SAC-1 and SAC-2) is the main tool in this technique of measurements of the absolute neutron yield Y_n . It is based on silver as activated material. The whole detector is composed of a Geiger-Muller (G-M) counter wrapped with a silver foil and placed within a hydrogen-reach moderator. Fast neutrons (2.5 MeV) emitted from a DPF source are slowed

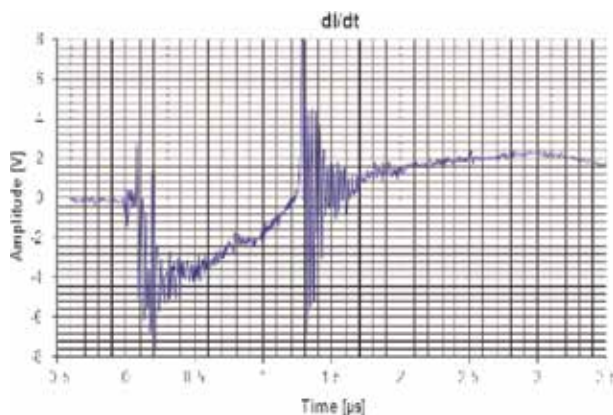


Figure 3.
Oscillogram of the current derivative for a typical “shot” of the PF-6 device.

down in the moderator. Indirect products of two reactions of decelerated neutrons with Ag are β^- emitters. This type of neutron detectors is a wide-spread tool in the DPF community, in particular because of the short (ns) neutron pulses generated by a DPF that is much shorter compared with the half-life of the reactions (see **Table 1**). We used these detectors with and without cadmium foil enveloping our moderators of SACs. With this foil, the effective “threshold” of neutrons’ energy registered by the counter is 500 keV. In this case, slow neutrons coming to the detector after scattering in the surroundings are not registered. SACs that were used since many years as the Y_n monitor for the PF-6 device were calibrated many times by special isotope-based neutron sources placed inside the device’s chamber. The calibration of SACs has been combined with MCNP calculation [14].

The SAC method has a number of limitations. It can be better operational if it will be used in a combination with other methods of Y_n monitoring. So other elements [14–18] (In , Be , and Y) were exploited for a so-called cross-calibration technique with SACs. In a **Table 1**, one may see the most important nuclear data regarding the nuclear reactions that were engaged in the PF-6 neutron activation monitors. Here, $T_{1/2}$ is the half-life time of particular radionuclides.

The elements have been chosen because of their specific advantages. Thus, a cross-section for the reaction with Be (the BNAC detector) has an effective threshold near 1 MeV, so undesirable multiple-scattered neutrons do not undergo this reaction and, therefore, are not measured. The inelastic scattering reaction with In has such a threshold equal to 340 keV. Fusion neutron yttrium monitor (FNYM) does not need any neutron moderator to allow neutrons detection.

A large area gas sealed proportional detector SP-126C (Canberra made) has been chosen in these techniques as a β^- particle counter. Its calibration includes the following procedures: use of calibration sources of β^- and neutron radiations with a parallel set of various Monte Carlo calculations for β^- particle and neutron transport. We applied the MCNP5 [16] Monte Carlo code with MCNP5DATA [17] cross section library that have been used for the above-mentioned calculations.

In some of the above-mentioned activation techniques, the gamma spectrometry system based on the high purity germanium (HPGe) detector equipped with multichannel analyzer (MCA) was used. The detector is supplied by the

Irradiated element	Nuclear reaction	Reaction’s product	Half-life decay, $T_{1/2}^a$	Mean energy E_β (keV)	Intensity (%)
^{107}Ag [14]	n, γ	^{108}Ag	2.382 m	629	95.5
^{109}Ag [14]	n, γ	^{110}Ag	24.56 s	1199.36	95.18
9Be [14–18]	n, α	6He	806.7 ms	1567.62	100
				E_γ (keV)	Intensity (%)
^{115}In [14]	n, n'	^{115m}In	4.486 h	336.241	45.8
^{115}In [14]	n, γ	^{116}In	54.29 m	1293.56	84.8
				1097.28	58.5
				416.90	27.2
				2112.29	15.09
^{89}Y [14]	n, n'	^{89m}Y	15.663 s	908.960	99.16

^ahttp://www.nndc.bnl.gov/nudat2/dec_search.jsp.

Table 1.

Nuclear data relating to the nuclear reactions that are engaged in neutron activation techniques.

manufacturer with its numerical characterization and software for mathematical calibration of the system (ISOCS/LABSOCS). Specific features of the above-mentioned activation methods, calibration procedures, and their MCNP support calculations one may find in the work [18].

2.3 Neutron spectroscopy based on the time-of-flight measurements

Time-of-flight (TOF) methodology was applied for the neutron spectra investigations with and without the above-mentioned simulator of a NFC. For this goal, two mobile measuring stands for experiments prepared to work in a harsh electromagnetic environment are used [1, 22]. The base for each measuring stand is the cabinet, which represent a Faraday cage featuring outstanding electromagnetic compatibility (EMC) shielding (it is possessed of 80 dB in the range from 30 to 300 MHz, of 60 dB in the range from 300 MHz to 1 GHz and up to 40 dB for the frequency band centered around 3 GHz).

At the data acquisition procedure, the stand is linked with the detectors and triggers only by the fiber optic connections (i.e., for triggering, time marking, and data transmission) with the devices positioned out of the stand, thus having no any galvanic contacts with the main lines and the experimental facilities. The stands are equipped with the converters for two-way signal conversion (**Figure 4**) and they are battery-powered.

The hybrid module is equipped with the photomultiplier tube (PMT) having 12 focusing dynodes. The conversion of ionizing radiation into light occurs in the fast organic scintillators S (so on the whole the system is named as a PMT + S—**Figure 5**).

Usually, the scintillators used in the device have 45 mm in a diameter and 50 mm of their length. This length was chosen due to its closeness to the mean free path of 2.5-MeV neutrons in it.

All PMT + Ss (these detectors will be named subsequently as TOF-1 or TOF-2) are inserted into the cylinders made of paraffin (served as collimators) and have a 2-mm lead foil blocking front part of the PMT + Ss to prevent them from scattered neutrons and soft X-rays. The oscilloscopes are triggered through the fiber optic cables. In **Figure 6**, one may see two stands near the PF-6 with the open door showing PMT + S, an oscilloscope and SACs on their roofs.



Figure 4. Elements of mobile measuring stands used for powering management and optical communication [19].

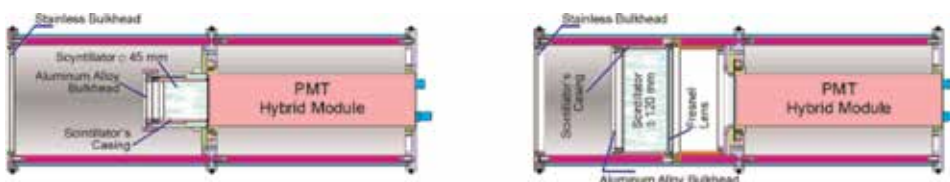


Figure 5. Key components of the fast neutron scintillation probes (FNSP-1) [19].

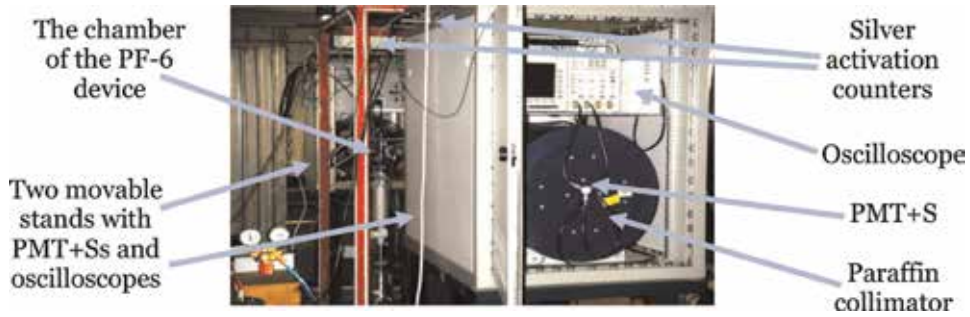


Figure 6. Experimental complex for measuring the neutrons field produced around the PF-6-based neutron source; it consists of two sets of detectors (silver activation counters and PMT + Ss) placed inside two cabinets.

In **Figure 7**, one may see an oscillogram of a cosmic radiation, demonstrating the temporal resolution of the PMT + S used in the experiments. It appears to be equal to 2.6 ns of its full width at half maximum (FWHM).

In **Figure 8**, the oscilloscope traces (OTs) for low (a), medium (b), and high (c) intensity of hard X-rays and neutrons are presented. It is seen that at a high-intensity of the X-ray and neutron radiations, the photomultipliers are working in a “current mode of operation” (**Figure 8c**) rather than in a “single-pulse” recording (as it is in a and b pictures) regime.

Our plan for the first step of experiments on the taxonomy of a simulator is to investigate the angular characteristics of neutron radiation of the PF-6 device itself in empty room (**Figure 9a**).

It is provided in the most “clean” hall by two stands. In this test, one stand (No. 1) has an immobile position in a direction perpendicular (90°) to the Z-axis of the PF-6 chamber, whereas the other one (stand No. 2) is moved around the PF-6 device.

After these measurements, giving information on the spatial distribution of neutron intensity around the PF-6 device itself, the second step of this procedure starts. In these tests, the same measurements must be done but already with the simulator (in its capacity a chamber of the PF-1000U facility is used). That gives an

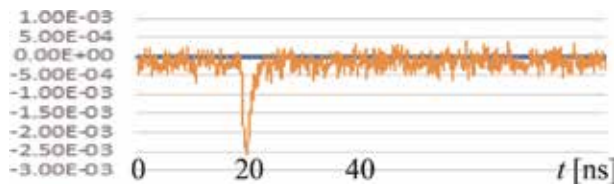


Figure 7. Oscilloscope trace (OT) of cosmic radiation measured by PMT + S (2.6 ns of its FWHM).

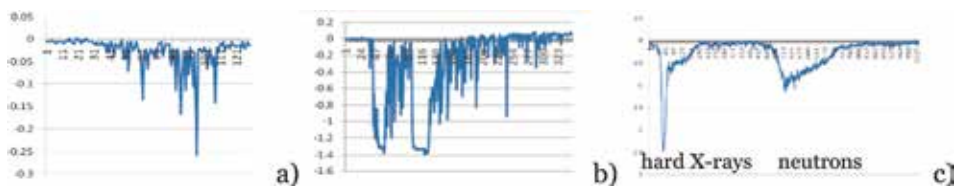


Figure 8. Oscillograms of three shots with low, medium, and high intensity of hard X-rays (1st pulses) and neutrons (2nd pulses); in the last oscilloscope trace all flashes produced inside the scintillator by individual X-ray photons and neutrons (a, b) are merged (c) and the PMT begins to work in the “current” mode of operation.

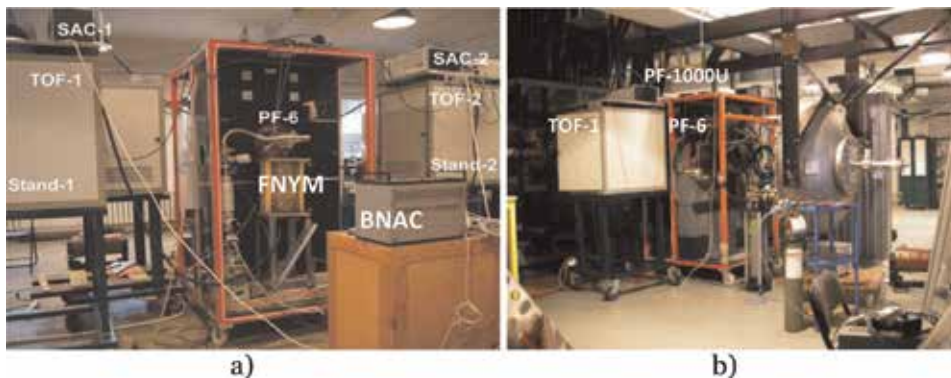


Figure 9. Steady-state position of the stand No. 1 (SAC-1 and TOF-1) and a movable stand No. 2 (SAC-2 and TOF-2) in its position No. 1 (see later) in a “clean-room” condition (a) as well as the same stands placed at their 90° positions to the Z-axis of both chambers of PF-6 (neutron source) and PF-1000U (simulator) devices (b).

opportunity to disclosure imperfections produced in the 3-D neutron field by scattering and absorption of 2.5-MeV neutrons in structures of the PF-1000U chamber as well as in the hall parts (**Figure 9b**).

3. Methodology

3.1 Theoretical treatment

3.1.1 Neutron emission anisotropy

The well-known nuclear fusion reaction $D(d,n)He^3$ produced by a parallel monoenergetic beam of high-energy deuterons propagating along Z-axis at its interaction with an optically “thin” target (a cloud) of deuterium gas or low temperature deuterium plasma (i.e., when its thickness is much less than the mean free path of deuterons in the cloud) is characterized in the laboratory system of coordinates [20, 21] by the following formula:

$$Q = \frac{4}{3}E_n - \frac{1}{3}E_d - \frac{2\sqrt{2}}{3}(E_d \cdot E_n)^{1/2} \cos \theta \quad (2)$$

where Q is the energy released in the reaction, E_d is the energy of a fast deuteron bombarding the deuterium target, E_n is the energy of a neutron, and θ is the angle in relation to Z-axis that neutron is emitted to.

This equation can be resolved, and it gives for neutron energy E_n :

$$\sqrt{E_n} = 0.3535 \cdot \sqrt{E_d} \cdot \cos \theta \pm \left\{ (0.125 \cdot \cos^2 \theta + 0.250) \cdot E_d + 2.475 \right\}^{1/2} \quad (3)$$

For the angle $\theta = 90^\circ$, this formula takes the simplest form:

$$E_n = \frac{3}{4}Q + \frac{1}{4}E_d \quad (4)$$

For the parallel beam of, e.g., 200 and 500-keV deuterons propagating along Z-axis (the angle $\theta = 0^\circ$) and bombarding plasma, the data on neutrons energy that escape the plasma volume (i.e., a target) at some angles are depicted in **Tables 2 and 3**.

Neutrons escaping angle θ_i (°)	Neutrons energy E_n (MeV)
90	2.47
0	3.1
180	2.0

Table 2.
Energy of neutrons produced by 200-keV deuterons with the exit angle θ_i .

Neutrons escaping angle θ_i (°)	Neutrons energy E_n (MeV)
90	2.57
0	3.6
180	1.8

Table 3.
Energy of neutrons produced by 500-keV deuterons with the exit angle θ_i .

Figure 10 represents an angle distribution of the effective differential cross-section σ_{eff} of the reaction $D(d,n)He^3$ in the laboratory system of coordinate. This picture is valid again for the low-intensity parallel monoenergetic beam of deuterons of energy $E_d = 500$ keV interacting with a “thin” target of deuterium plasma of relatively low temperature [20, 21]. Neutron stream density (fluence) is proportional to the effective differential cross-section σ_{eff} . Now, we can define the neutron anisotropy for the particular plasma device as a ratio of fluencies obtained in different directions:

$$A(\theta_i) = \varphi(\theta_i)/\varphi(90^\circ) \tag{5}$$

where $A(\theta_i)$ is the anisotropy of neutrons emitted at an angle of θ_i to the direction of the beam of fast deuterons (i.e., to Z-axis of a DPF oriented from its anode), $\varphi(\theta_i)$ is the fluence of neutrons emitted at an angle of θ_i , $\varphi(90^\circ)$ is the fluence of neutrons emitted at an angle of 90° , and various i are the subsequent positions where anisotropy is calculated and/or measured. From the next section, one can get that each i denotes the angle that corresponds to the measuring position location.

It gives for the data on anisotropy of neutron streams at various angles normalized to the value at 90° that produced by the beam of 500-keV deuterons at its interaction with a low-temperature deuterium plasma the following values (**Table 4**).

Thus, the theoretical angular distribution of neutron intensity produced in an “optically” thin deuterium gas (or low-temperature plasma) target by a

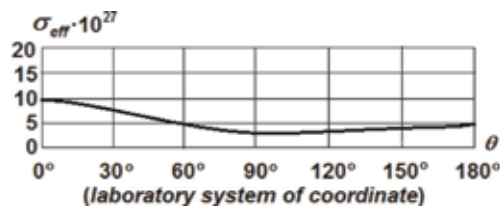


Figure 10.
A graph of the effective differential cross-section σ_{eff} for neutrons taking part in the reaction $D(d,n)He^3$ that is presented for the laboratory system of coordinate in dependence on the angle. The diagram is calculated for the case of the mono-energetic beam of deuterons having energy $E_d = 500$ keV and interacting with a so-called “thin” target of deuterium plasma of fairly low temperature.

Angle θ_i (°)	Anisotropy coefficient A for the beam of 500-keV deuterons normalized to the value at 90°
90	1.0
0	3.33
180	1.8

Table 4.
 Anisotropy coefficient on the exit angle normalized to the value at 90°.

low-intensity parallel mono-energetic beam of 100-keV deuterium ions as test particles (usually for the DPF deuteron spectrum obtained in various conditions, different authors give a figure in the range of hundreds KeV—see e.g., [8, 22]) looks similar to the eight digit (see **Figure 11** plotted for the monoenergetic deuterons of 100-keV energy). In a center-of-mass system, it is symmetrical, whereas in a laboratory coordinate frame, it is slightly shifted in the direction of the beam propagation with $A(\theta_i) \approx 2.0$ and 1.5 for 0 and 180° correspondingly.

However, one has to take into account that the main part of neutrons generated in DPF is produced by gyrating deuterons [8, 22]. These particles escape pinch plasma (target) at a certain effective angle. So, it must give for the direction of Z axis the lower values of anisotropy counted for 100-keV deuterons: $A(\theta_i) \approx 1.7$ and 1.2 for 0 and 180°, respectively.

Moreover, the spectrum of fast deuterons in DPF devices is not monoenergetic: it extends till MeV range following the power law with a peak at hundred keV [8]. As it is known, the deuterons generating neutrons are captured for a certain time by self-produced magnetic fields and then fly out from the pinch under an appreciable angle as it was mentioned above. Besides, this flow of deuterons is very dense and intense (so it may be better characterized as a fast-moving cloud—high-energy and almost relativistic plasma jet) [8, 22].

All these features must result in the obtained experimental data for neutron anisotropy and spectra in smoothing of the pictures compared with the aforementioned theoretical ones. One may expect that the energy of deuterons producing neutrons in a DPF will occupy an energy range in the interval between the above-mentioned values (i.e., for deuterons energy distributions with their peak energy somewhere from 100 till 500 keV).

3.1.2 Time-of-flight spectral measurements

As it is well known [20, 21], the TOF technique converts a temporal behavior of the ns pulse of the neutron emission reflected in the pulse shape for the PMT + S positioned at the close vicinity to the generator into the pulse shape reproducing

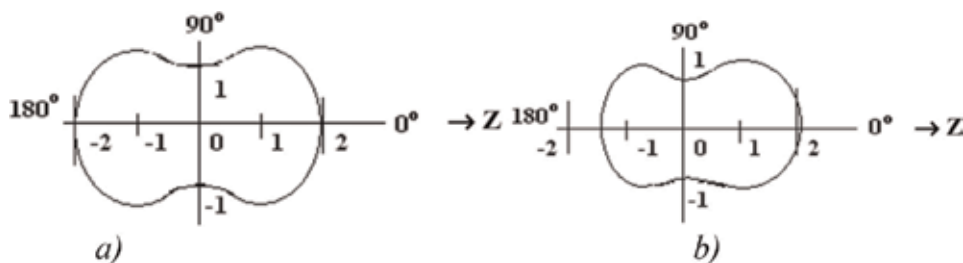


Figure 11.
 Theoretical angular distribution of neutron intensity produced in an “optically” thin gas target by a low-intensity parallel monoenergetic beam of 100 keV deuterium ions: in a center-of-mass system (a) and in a laboratory coordinate frame (b).

spectral characteristics of neutron radiation when the fast probes is moved to a certain distance (the speed distribution of particles transfers into the space one).

Time-of-flight of neutrons measured by means of PMT + S can be transformed into the energy distribution of the neutrons producing the neutron pulse. Their maximum may be expressed by a ratio (6) presented in books [20, 21]:

$$E_{MeV} = (72.24 l_m / t_{ns})^2 \quad (6)$$

In this formula, E_{MeV} is neutron energy in (MeV), l_m is a distance in (m), and t_{ns} is a flying time interval in (ns).

To transform temporal behavior of a neutron pulse in the OT into spectral distribution of neutrons by their energy values in the OT, the distances l from the source till the PMT + S for the observation of spectra must be much longer compared with the size of the neutron pulse in space (in our case $l \gg 10$ cm).

3.2 Neutron activation techniques application for the “clean-room” conditions

The first stage of the characterization experiments is the investigation of the angular characteristics of neutron yields of the PF-6 device itself by activation methods. General arrangement of the two stands with SACs and other activation detectors as well as with two stands containing PMT + Ss-related equipment is shown in **Figure 9** in the positions of a “clean-room” condition (*a*). Note that there is a difference in heights of the positions of PMT + Ss and SACs: the PMT + Ss are situated in the plane of Z-axes of the PF-6 and PF-1000U chambers (that are directed horizontally in relation to the floor) but the SACs are placed 70 cm higher.

This taxonomy of the PF-6 device was provided in the most “clean” hall. However, it must be noted here that these conditions are not absolutely “clean.” Indeed, the device itself has four capacitors filled with a castor oil (scatterers), the concrete floor and ceiling are presented, four coils of cables and four separating transformers are the elements of the PF-6 construction. All of these parts are rather bulky scatterers/absorbers. Due to these obstacles, we shall use the term “absolute” neutron yield in the subsequent text for the figures that will represent the values which are only correlate with another instruments’ data in the dissimilar positions. Thus, these data are the “virtual” readings, or the “absolute” quantities with the identical but unknown standardizing coefficient.

During the experimental simulations, the neutron yield (Y_{nTOTAL}) is monitored using two SAC(s). The shots of the PF-6 device when the Y_{nTOTAL} magnitude was in the range of 10^8 – 10^9 neutrons per pulse were taken into account only. Side by side with two silver activation counters (SACs), the activation detectors based on *Be* and *Y* were used. The *Y* neutron detectors give the data that are correlated with the neutron yield obtained from SAC quite well (see **Figure 12**).

The calibration measurements were produced during the successive 33 shots with SAC-1 and SAC-2. These probes were placed normally to the Z-axis of the chamber of the PF-6 device from its two opposite sides. Then keeping the position of the probe with SAC-1, the stand No. 2 was relocated along the way around the PF-6 device with seven different stops shown in **Figure 13**.

The procedure looks as follows. There are two cages. Each cage has a SAC placed 70 cm above the Z-axis of the PF-6 chamber (**Figure 13b**). The Z axis covers the axis of symmetry of the PF device. The X axis is horizontal, so the Y axis is vertical.

For any (x, y, z) point $\theta = \arccos \{z / (x^2 + y^2 + z^2)\}$ is the angle between vector $(\vec{x}, \vec{y}, \vec{z})$ and the Z axis. This gives the spatial angles θ_i° that differ from those

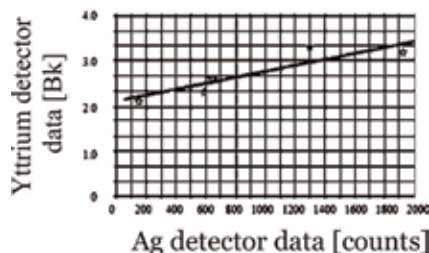


Figure 12. Data of the absolute neutron yield measured during the experimental session with yttrium and silver activation counters averaged over 10–20 shots for each point of the graph.

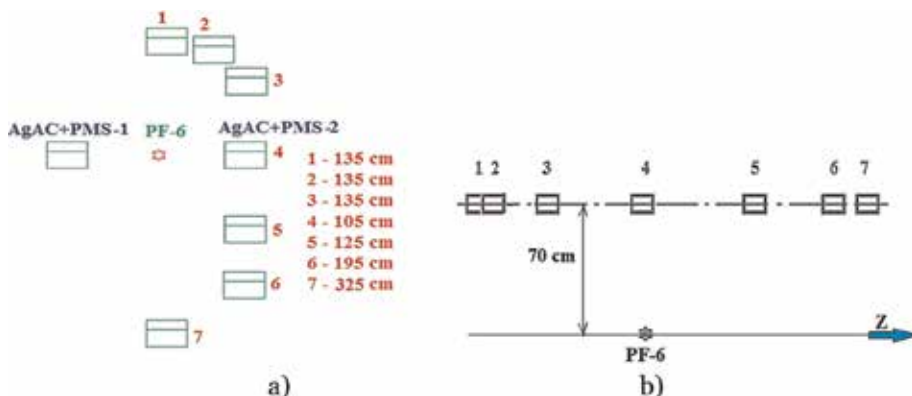


Figure 13. Presentation of the diagram of the immobile position of the stand No. 1 and seven successive locations of the movable stand No. 2: top view—(a) and side view—(b) during measurements of the angular distribution of “absolute” neutron yield by SACs for the PF-6 device in a “clean” situation.

“flat” angles α_i° depicted in **Figure 13a**. From literature, one may find that neutrons produced in DPF and irradiated in all directions perpendicular to Z-axis (i.e., for the detector SAC-1 in its immobile place and for the detector SAC-2 in the position 4) has usually the energy peak near the value equal to 2.5 MeV for reacting deuteron having energy of hundred’ keV [20, 21].

Step 1: At the beginning, the background (i.e., cosmic radiation) data are fixed by both SACs. It is repeated five times and the mean figures (usually it is $\sim 30\text{--}40$ counts in the case) are computed for each collection of shots.

Step 2: On the assumption that for both SACs placed at 90° (i.e., perpendicular to the Z-axis of the PF-6 chamber—position No. 4 for a movable SAC-2), neutron yields are the same (with this device it was proved many times), and their individual sensitivities ratio is calculated as $Y_{n1}/Y_{n2(\text{position } 4)} = Q_1$. This is a standardization coefficient Q_1 for all subsequent calculations for different positions of a SAC-2 and for dissimilar neutron outputs in various collections of shots. For example, in this set of experiments, $Q_1 = 1.374$.

Step 3: Data that were collected by the SAC-1 and by the SAC-2 in its different locations ($Y_{n1(i)}$ and $Y_{n2(i)}$) are averaged over about 10–20 “good” shots during a single session, so the mean figures for each collection of shots $Y_{n1(i)\text{measured}}$ and $Y_{n2(i)\text{measured}}$ are calculated after deducting background values.

Step 4: At that time, the “actual” magnitudes of $Y_{n2(i)}$ of the SAC-2 are calculated with the detector sensitivity correction:

$$Y_{n2(i)\text{real}} = Y_{n2(i)\text{measured}} \times Q_1 \quad (7)$$

Step 5: The remoteness r_{2i} of the detector SAC-2 from the PF-6 chamber are computed for each of its positions; then a standardization procedure is produced according to the knowledge of the real distance lengths between the source and the SAC-2: r_{SAC-2} . Subsequently by applying the r^{-2} law, the factors for the neutron yield belonging to all locations of the detector SAC-2 are gained:

$$k_i = (r_{SAC-2i}/r_{SAC-2(position\ 4)})^{-2} \quad (8)$$

Step 6: By means of the multiplication of the above-mentioned “actual” neutron yields $Y_{n2(i)real}$ with these factors k_i and regularizing them by the character for $Y_{n1(i)}$ in each collection of shots “ i ,” a coefficient of the anisotropy A in the “clean” room is gained finally:

$$A = k_i (Y_{n2(i)real}/Y_{n1(i)}) \quad (9)$$

3.3 Neutron activation techniques application for the conditions with an object simulating a section of a toroidal chamber of a mainstream fusion facility (the PF-1000U chamber)

Upon obtaining data on the clean-room conditions, the neutron source—PF-6 device—as well as the both fast probes No. 1 (SAC-1 plus TOF-1) and No. 2 (SAC-2 plus TOF-2) must be transported to the simulator, that is, to the PF-1000U facility chamber. In this arrangement, we must repeat the measurements of the same type as above but around the model set representing the tokamak chamber section (Figure 14).

The data acquired in this structure (Figures 14, 15, and 9b) are compared with the previous data (Figure 9a) as well as with monitoring of readings of the transportable test desk No. 2 in comparison with the values obtained by the stand No. 1 in its steady-state location.

Besides, in these experiments, a special 2/4-cm stainless steel (SS) supplement (see Figure 16) on the top of the PF-6 chamber was mounted that represented an additional irregularity (mainly in forward direction of neutron propagation).

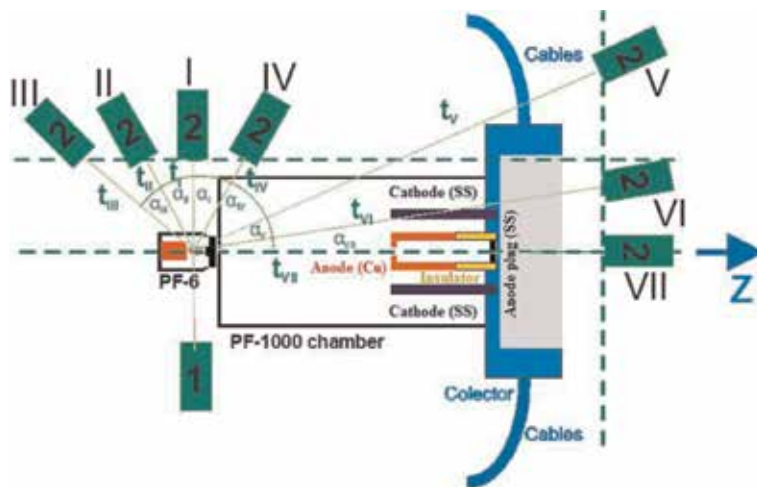


Figure 14. A scheme of a steady-state location of a stand No. 1 (i.e., the stand containing the activation counter SAC-1 and the fast probe PMT + S—TOF-1) and seven different locations of a movable stand No. 2 during the simulation experiment with the PF-1000U chamber (i.e., a stand with the SAC-2 and the PMT + S probe TOF-2)—top view.

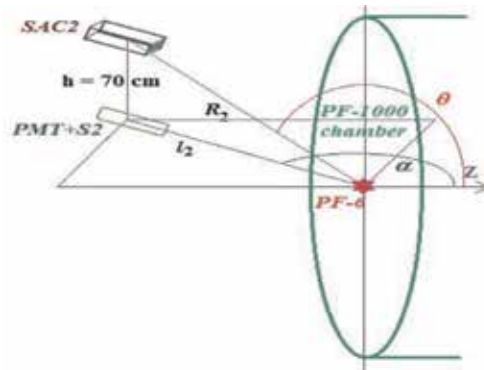


Figure 15. Distances l_2 , R_2 and angles α , θ in the plane of the SACs, and the real 3-D angles from the source to the SAC2, depicted for a hall with a simulator.

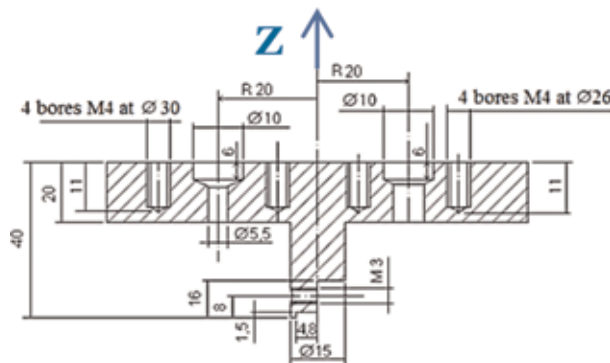


Figure 16. A stainless steel (SS) supplement placed on the top of the PF-6 chamber in front of the anode; distance between the anode top and the lid's peg was 3.5 cm.

3.4 Neutron spectral measurement procedure by time-of-flight technique for the “clean-room” condition and for the experiments with a simulator

The typical fast probe OT of the PMT + S-1, that is, obtained by the immobile stand No. 1 with TOF-1, for the experiment made in a “clean-room” condition is given in **Figure 17**.

The PMT + S probes No. 1 (immobile) and No. 2 (movable) are placed in the horizontal plane coinciding with a Z-axis of the PF-6 chamber. The above-mentioned TOF method was used to obtain information on the angle neutron spectral distribution. Again, the PMT + S-1 position (TOF-1) was preserved from one side of the PF-6 chamber but the PMT + S-2 stand (TOF-2) was moved along the steps 1 through 7 shown in **Figure 13a**.

As it was mentioned above, the neutrons' energy is 2.5 MeV [8] at the angle 90° to Z-axis of the chamber; so for the detectors Nos 1 and 2 placed at 1.05 m we have to move forward the hard X-ray pulse by its time-of-flight equal to 3.5 ns ($v_{hxr} = 3 \times 10^8$ m/s) and the neutron pulse—by 48.5 ns ($v_n = 2.1667 \times 10^7$ m/s) as it is shown in **Figure 18a** and **b**.

This correction on TOF of both types of radiation (we have taken a mean value for it calculated for the 33 shots) provides the time interval for the delay of the neutron pulse peak appeared near the anode of the DPF chamber in relation to the front of the hard X-ray pulse. We found that in these experiments, it was equal to

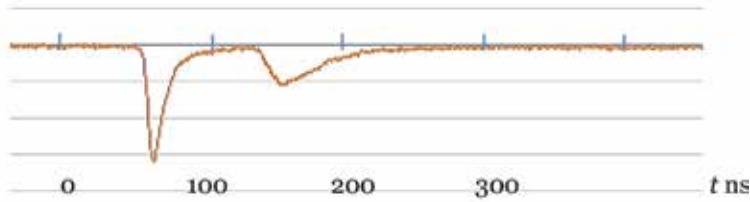


Figure 17. Typical OT of hard X-ray (1st— $\Delta t_{FWHM} = 10$ ns) and neutron (2nd) pulses of the PF-6 device (neutron pulse: $\Delta t_{FWHM} = 20$ ns).

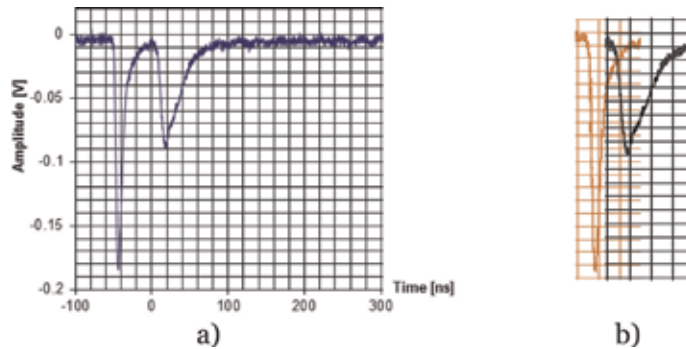


Figure 18. Initial (measured—a) and corrected for TOF positions of hard X-ray (1st) pulse and 2.45-MeV neutron (2nd) pulse (b).

$\Delta t = 25$ ns for each stand in this collection of experiments. Later, one must recheck this figure in each shot by using fixed stand No. 1. Typically, the rise-time of the hard X-ray pulse is vertical practically, that is, it is equal to the fast probe temporal resolution and, consequently, to the measurements' uncertainty. These readings establish for us a foundation for the following measurements and amendments fitted for all other neutron pulses observed at different angles and at dissimilar remoteness from the PF-6-based pulsed source of neutrons. So in every shot, we begin our temporal calculations from the front of the hard X-ray pulses, subsequently moving the neutron pulses to the time moment delayed in relation to the X-ray front namely by this Δt .

After such a procedure, we obtained an opportunity to calculate TOF of this neutron pulse to the detector No. 2 in its each specific location. Using formula (6), this measured and corrected time-of-flight can easily be recalculated into the energy of this neutron group producing the neutron pulse maximum. Results of calculations at usage of the above procedure and the formula give the angle dependence of the neutron spectral distributions in the space around our PF-6 device in a “clean” room conditions.

The same procedure of neutron spectra distortions has been provided in the experiments with the PF-1000U chamber simulator.

4. Numerical simulations

4.1 Geometrical model

We have used a geometrical model of this simulation experiment in a simplified form. The scheme encloses the PF-1000U stainless steel vacuum chamber, a set of

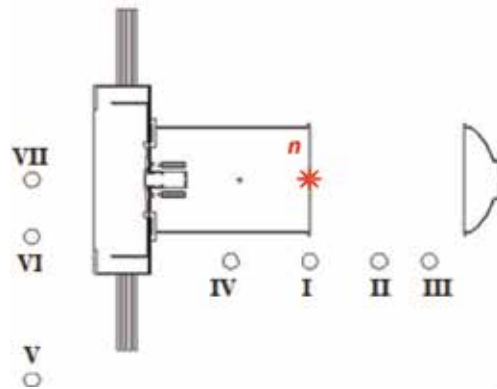


Figure 19. A cut-view of the geometrical MCNP input: ZX plane. Numbered spheres are “detectors”, the star with the letter “n” denotes neutron source (PF-6).

electrodes with insulators, a collector with cables, as well as all details of the hall interior. The vacuum cover of the PF-1000U chamber is detached and removed 2 meters away along Z-axis. Thus, an air is filled in the chamber. A frame of reference is originated in the center of the anode end. The Z-axis is on the axis of symmetry of the chamber, the X-axis is horizontal, whereas the Y-axis is vertical. A cross-section of the model in the X-Z plane is offered in **Figure 14** and in **Figure 19**.

4.2 Neutron source

The source of neutrons is point and lies on the Z-axis near the end of the opened chamber of the PF-1000U facility. The coordinates are (0, 0, 160) cm. The energy spectrum of neutrons is the Gaussian one. The peak of the most probable energy of the Gaussian spectrum of neutrons depends on the direction of neutron emission.

The group of neutrons that are emitted in-Z direction (in opposite direction in the respect to Z-axis) has energy around 2.7 MeV, neutrons that are emitted in XY plane (90° in respect to Z-axis) have their peak energy around 2.45 MeV, and the group of neutrons emanated in +Z direction (i.e., at 0° in respect to Z-axis) has their energy peak around 2.3 MeV. In all in-between directions, the neutron groups have corresponding intermediary energies. The widths of all Gaussian peaks are assumed to be 120 keV. The neutron emissions in all directions are unequal (i.e., anisotropic) as it is described above.

4.3 The code

The MCNP code (X-5 Monte Carlo Team, MCNP—A general Monte Carlo N-particle transport code, Version 5, Los Alamos National Laboratory, LA-UR-03-1987, 2003 [16]) was carried out for calculations. Cross-sections used in these computations have been derived from the ENDF/B-VI library [17].

4.4 Tallies

Calculations of neutron flux density and spectra have been performed for seven spheres of air placed in positions with spherical coordinates that are described in Section 3.2.

Let us denote φ_n ($n = I, II, \dots, VII$) as MCNP calculated neutron flux density in n -th SAC. Then anisotropy $A_n(\theta_n)$ equals:

$$A_n(\theta_n) = \frac{\varphi_n r_n^2}{\varphi_1 r_1^2} \quad (10)$$

Using the above procedure, we have provided test calculations both for neutron anisotropy and spectra for several configurations close to the experimental ones including those for the pulse shape as it is seen in the oscilloscope traces.

5. Results and discussions

5.1 Experimental results on measurements of anisotropy of neutron emission using PF-6 device positioned in an “empty” hall

One may see the results of anisotropy measurements after their processing in **Figure 20**. As in **Figure 13a**, this is the top view. Thus, it is a projection of the plane of SACs (70 cm above Z-axis) to the plane containing PMT + Ss and Z axis. In particular, for example, for the SAC-2, the so-called “flat” angle presented as $\alpha = 0^\circ$ corresponds in the 3-D diagram to the actual angle $\theta = 12^\circ$. Juxtaposition of the experimental figures and the theoretical data (see **Figure 11** and the side analysis) one may find a number of dissimilarities. However as it was mentioned before, the beam of deuterons is not a parallel one because of the magnetization of ions in the self-generated magnetic fields [8, 22]). Besides, this beam of fast deuterons is very powerful and its energy spectrum is very broad extending to the MeV range (so this stream is non-monoenergetic one). It is a reason for the observed in the experiment a certain “leveling” of the “8-digit” form of anisotropy shown in **Figure 11**. In addition, there are two peculiarities of the graph 20 that must be discussed.

1. It is seen that in forward directions (V, VI, and VII), a value of anisotropy is noticeably larger compared with those from literature [8]. Usually these values are about 1.4–1.7. Such figures can be obtained by means of formula taken from [20, 21] if the most typical deuteron energy will be equal to $E_d \approx 100$ keV and at the condition that the basic part of fusion neutrons are generated by magnetized deuterons that are flying out of the pinch within a cone having an angle to Z axis equal to about 20° [22]. But in these experiments, the magnitudes of neutron fluxes are equal to 1.8, 2.1, and 2.4 observed in these directions.

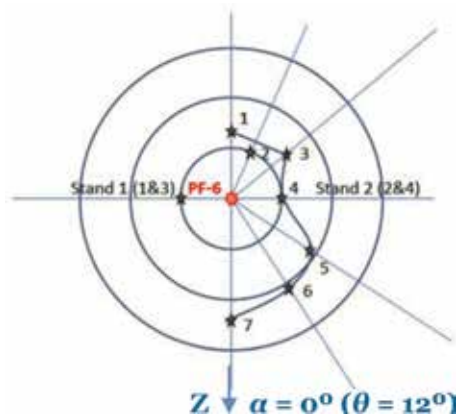


Figure 20. Polar chart of neutron fluxes measured for different angles in relation to Z-axis of the PF-6 device for the case of the “clean-room” environments (here it is a projection from the plane 70-cm above the plane of Z-axis of the PF-6 chamber); in this chart, the radii of successively enlarged rings correspond to anisotropy coefficients equal to 1, 2, and 3, respectively; the coefficients are normalized on the value for the position 4.

2. One may notice a bit strange result for the position 2 of **Figure 20**: just opposite to the previous case, we observed a low value of the neutron flux measured at the angle $\alpha = 157^\circ$.

It is possible to find an interpretation of these features by comparing these experimental results with the MCNP modeling of the process.

Some parts of the PF-6 device itself as well as the hall environment can influence the ideal theoretical representation. The Monte-Carlo (MCNP-5) computations have been provided especially to describe the PF-6 itself and its surroundings. As it is known, the MCNP technique does not permit undertaking an inverse problem. Thus, we have provided a number of numerical simulation for the following dissimilar experiment's situations:

1. The source of neutrons placed at the beginning of system of coordinates (in the center of the PF-6 anode surface) is point, isotropic, and monoenergetic (with $E_n = 2.5$ MeV).
2. Geometry of capacitors, separating transformers, floor, ceiling, and cables is approximate and simplified.

For identification of an influence of each component of the environment, we have provided six successive sets of the computations: with vacuum everywhere and with separating transformers on their places; vacuum everywhere with capacitors in their locations; vacuum everywhere with floor and ceiling of the hall; vacuum everywhere and hank of cables; all components are presented; only vacuum.

3. All calculations of the neutron flux density have been fulfilled for seven detectors placed in their real positions coinciding with those in the present experiments. Detectors were represented by spheres of 15 cm radius each.

Calculations have been done for two cases—with absence and in presence of the cadmium foils enveloping each SAC—see **Tables 5** and **6** correspondingly. The first one contains results of calculations of neutron flux density (cm^{-2}) of the whole spectrum of neutrons reaching the detector. The second one comprises data obtained for calculations of flux density of neutrons with energy spectrum above 500 keV.

The values of flux densities in seven directions around the PF-6 chamber (i.e., anisotropy) were calculated for each case taking into account the distance of the detector from the source using an inverse quadratic law for radii. Examination of these tables shows quite clearly:

1. The cadmium foil enveloping our SACs is a very effective screen preventing penetration to the counter of low-energy neutrons that appears due to multiple scattering in the environment.
2. The first above-mentioned peculiarity of the chart is partially explained by scattering (reflection) of fast neutrons in forward direction on concrete ceiling and floor (for example, at 0° the figure looks as follows:
 $1.7 \times 1.23 = 2.1$).
3. The second effect is explained by scattering of neutrons on the coil (bundle) of cables: the data of experiment and modeling coincide numerically almost exactly.

No	Coordinates and points of neutron flux measurements			PF-6 with separating transformers		PF-6 with capacitors		Hall ceiling and floor		Hanks of cables		All components of the PF-6		Vacuum everywhere		
	x	y	z	R	MCNP	A	MCNP	A	MCNP	A	MCNP	A	MCNP	A	MCNP	A
1	0	58	-135	146.932	3.92E-06	1.04	3.93E-06	1.02	5.10E-06	1.08	3.77E-06	1.02	5.27E-06	1.09	3.70E-06	1.00
2	54	58	-127	149.6964	3.69E-06	1.01	3.79E-06	1.02	4.95E-06	1.09	2.91E-06	0.81	4.31E-06	0.92	3.56E-06	1.00
3	105	58	-85	147.017	3.85E-06	1.02	3.89E-06	1.01	5.10E-06	1.08	3.77E-06	1.02	5.23E-06	1.08	3.71E-06	1.00
4	105	58	0	119.9542	5.68E-06	1.00	5.77E-06	1.00	7.07E-06	1.00	5.57E-06	1.00	7.28E-06	1.00	5.55E-06	1.00
5	105	58	68	137.8876	4.28E-06	1.00	4.40E-06	1.01	5.64E-06	1.05	4.20E-06	1.00	5.84E-06	1.06	4.20E-06	1.00
6	105	58	164	203.1871	1.97E-06	1.00	2.05E-06	1.02	3.08E-06	1.25	1.93E-06	1.00	3.22E-06	1.27	1.93E-06	1.00
7	0	58	325	330.1348	7.45E-07	0.99	7.84E-07	1.03	1.36E-06	1.46	7.33E-07	1.00	1.43E-06	1.49	7.37E-07	1.01

Table 5. Results of calculations of neutron flux density (cm^{-2}) of the whole spectrum of neutrons reaching the detector.

Coordinates and points of neutron flux measurements		PF-6 with separating transformers		PF-6 with capacitors		Hall ceiling and floor		Hanks of cables		All components of the PF-6				
No	x	y	z	R	MCNP	A	MCNP	A	MCNP	A	MCNP	A		
1	0	58	-135	146.932	3.91E-06	1.03	3.77E-06	1.00	4.26E-06	1.04	3.75E-06	1.01	4.40E-06	1.06
2	54	58	-127	149.6964	3.69E-06	1.01	3.63E-06	1.00	4.12E-06	1.04	2.90E-06	0.81	3.46E-06	0.86
3	105	58	-85	147.017	3.84E-06	1.02	3.77E-06	1.00	4.26E-06	1.04	3.76E-06	1.02	4.37E-06	1.05
4	105	58	0	119.9542	5.67E-06	1.00	5.64E-06	1.00	6.17E-06	1.00	5.55E-06	1.00	6.25E-06	1.00
5	105	58	68	137.8876	4.28E-06	1.00	4.28E-06	1.00	4.78E-06	1.02	4.20E-06	1.00	4.84E-06	1.02
6	105	58	164	203.1871	1.97E-06	1.00	1.98E-06	1.01	2.39E-06	1.11	1.93E-06	1.00	2.42E-06	1.11
7	0	58	325	330.1348	7.45E-07	0.99	7.50E-07	1.01	9.98E-07	1.23	7.33E-07	1.00	1.01E-06	1.22

Table 6. Results of calculations of neutron flux density [cm^{-2}] of the spectrum of neutrons above 0.5 MeV reaching the detector.

Examination of our geometry of the PF-6 chamber used in these experiments has also shown that too high intensity in the “forward” direction (points 5, 6, and 7—values up to 2.4) may be explained (additionally to the above-mentioned influence of concrete ceiling and floor) very likely by a specificity of the anode construction in this case. Instead of an aperture usually made in the anode center to prevent evaporation of debris by the electron beam we had in this case a special central insert made of rhenium. In this case, such an insert made of refractory materials helps to produce the most representative group of fast deuterons having higher energy compared with a common case. We observed some years ago this effect with the central anode insert made of tungsten. Because of this fact, the value of the projection of $E_{d \text{ max}}$ onto Z axis appears to be here in the range 150–200 keV, whereas the real value of these deuterons taking into consideration their preferential escaping angle [22] of about 25° can be estimated approximately as 300 keV.

5.2 Data on anisotropy measurements of neutron emission using PF-6 device in the presence of the simulator of a section of a toroidal chamber of a mainstream fusion facility (the PF-1000U chamber)

The process of measurements of neutron fluxes in different directions is about the same as above for the case of the empty hall with a bit different distances from the neutron source to the Faraday cages No. 1 and No. 2 (they were recalculated). Results of these measurements and their treatment including construction of an anisotropy graph are depicted in **Table 7** (together with the “clean-room” data for comparison) and in **Figure 21** presented here for demonstrativeness. This picture is a polar chart analogous to that of **Figure 20**. It presents quite perceptibly both data on anisotropy obtained in a “clean” room conditions (shown by green color) and in a hall with a simulator of a tokamak chamber section (red color). This large-scale object is represented here by a discharge chamber of the PF-1000U installation (see **Figure 14**). In particular, one may clearly see a strong influence of the PF-6 chamber supplement (**Figure 16**) and PF-1000U chamber electrodes (**Figure 14**) produced upon the neutron flux densities under the measurements. Indeed, it becomes apparent in the position V: here between the SAC-2 and the source, the flat part of the supplement (2 cm of stainless steel) is situated; it is even more evident for the locations VI and VII where the SAC-2 records the neutron flux passing through the supplement’s protrusion (here we have 4 cm of SS) and through the PF-1000U chamber electrodes. At the same time, just contrary—in the locations of the SAC-2 numbers III, II, I, and IV, the data obtained in this experiment feebly differ from the readings attained in the empty room (positions 1, 2, 3, 4, 5 of the SAC-2).

For the position III, which is close to the location 2 in the empty-room conditions, the same peculiarity (a small dip) in the neutron flux density is observed. It is a consequence of the presence of the same object as in the above-presented

Positions of the detectors SAC&PMT + S2 during the tests with the simulator	III	II	I	IV	V	VI	VII
A—an anisotropy coefficient in the simulation tests	1.17	1.31	1.0	2.16	1.63	0.415	0.13
Positions of the SAC&PMT + S2 during the “clean-room” framework tests	1	2	3	4	5	6	7
A—an anisotropy coefficient in the “clean-room” framework tests	1.3	1.0	1.4	1.0	1.8	2.1	2.4

Table 7.
Data on anisotropy of the neutron yield in the hall with the simulator.

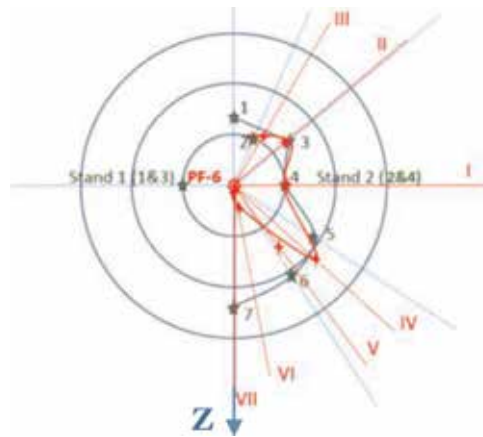


Figure 21. Polar diagram of neutron yield measured for the PF-6 device in the conditions with a simulator of a section of a tokamak chamber by means of the discharge chamber of the PF-1000U facility; it is shown by red color (the green color diagram refers to the “empty-room” condition).

“clean-room” conditions (an influence upon the neutron radiation produced by the cables bundle). A noticeable influence of the PF-1000U chamber may be seen in the location V (in this very direction the scatterers/absorbers obstacles are cables of the PF-1000U facility—see **Figure 14**). In the locations VI and VII where the SAC-2 is blocked by a thick SS supplement of the PF-6 chamber itself and by the central part of the chamber of PF-1000U device (electrodes), the SAC-2 readings were dramatically decreased.

This chart is again an image projection of a polar diagram presenting both data on anisotropy obtained in a “clean” room conditions (shown by green color) and with a simulator (red color) in the plane of SACs that are 70 cm higher than the level with Z axes of PF-6 and PF-1000U facilities and the detectors PMT + Ss. This is a vertical projection of the neutron flux angular distribution to the horizontal plane containing Z axes of both devices as it is shown in **Figures 13** and **14**. After this session, we came to processing of data obtained with fast probes (PMT + Ss).

5.3 Experimental results on measurements of spectra of neutron emission using PF-6 device with an object simulating a section of a toroidal chamber of a mainstream fusion facility (the PF-1000U chamber)

First, we made the measurements in the “clean room” condition. We preserved the PMT + S-2 position from one side of the DPF chamber (at 105 cm) but moved PMT + S-4 along the steps shown in **Figure 14**. In the direction perpendicular to Z-axis (at the angle 90^0) of the chamber as it was mentioned above the neutrons’ energy is 2.5 MeV [1]. Thus to tie the neutron pulse to the X-ray pulse in the center of the PF-6 chamber for the detectors Nos 1 and 2 placed at 1.05 m, one have to shift forward in time the hard X-ray pulse by 3.5 ns ($v_{hxr} = 3 \times 10^8$ m/s) and the neutron pulse by 48.5 ns ($v_n = 2.1667 \times 10^7$ m/s) in a way that is presented in **Figure 18a** and **b**. As a result of this process (averaged over 33 shots), the delay time of neutron pulse maximum inside the chamber in relation to the hard X-ray pulse front has been found as $\Delta t = 25$ ns for both stands. In this set of experiments and later we checked this figure in each shot by using fixed stand No. 1. After these experiments, we obtained the basic data for the subsequent measurements and corrections that have to be done for all other neutron pulses registered at different angles and at dissimilar distances from the neutron source based on the PF-6 device.

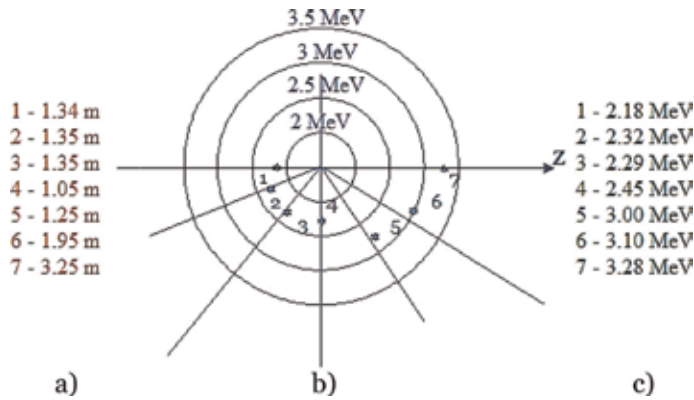


Figure 22. Angular tracking of energy distribution of neutrons at the PF-6 device in “clean” conditions: (a)—distances from the source (PF-6) to the detector (PMT + S No. 2); (b)—polar diagram of the angular tracking of neutron energy distribution; (c)—data table of energies measured in the specific points.

Each time we begin from the front of the hard X-ray pulse, moving neutron pulse to the point delayed to the front by Δt inside the chamber. Then the TOF of this neutron pulse from the chamber to the detector No. 2 in each specific location is calculated. This time-of-flight can easily be recalculated into the energy of this neutron group by formula (6). Results of calculations gave us the angle tracking of the neutron spectral distribution in the space around our PF-6 device in a “clean” room that is presented in **Figure 22**.

In the next step, we have compared these results obtained by PMT + Ss with the data attained with the PF-1000U discharge chamber (**Figure 14**). The procedure looks as it was before for the “clean-room” experiment.

Again in the beginning, we made measurements of the delay of the maximum of a neutron pulse in relation to the front of the pulse of hard X-rays inside the DPF chamber. For the fixed stand No. 1 placed now at a distance of 0.9 m from the source the delay time of hard X-ray pulse here was 3 ns. The neutron pulse maximum inside the chamber in relation to the hard X-ray pulse front was found now to be in the interval of 9...18 ns in different sets of shots—see e.g., **Figure 23**.

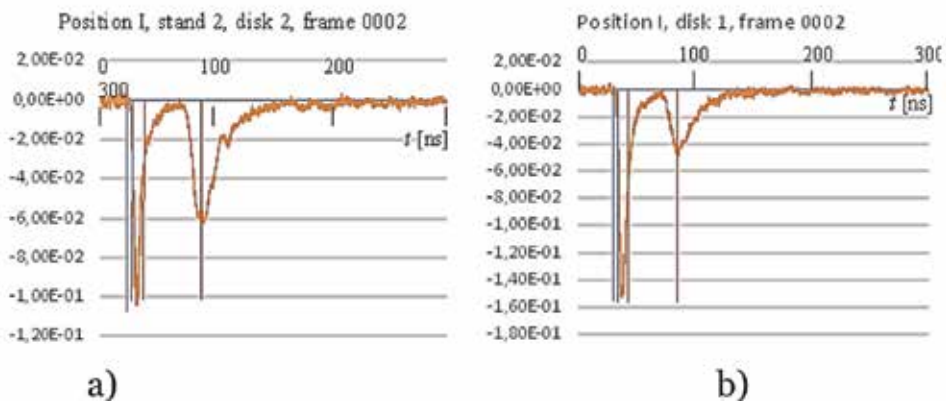


Figure 23. OTs obtained at 1.1-m distance from the source by a movable stand No. 2 (a) at the location perpendicular to Z-axis (position I of 14) and by a fixed stand No.1 placed at the distance of 0.9 m (b)—both with vertical lines showing shifts of the fronts of the hard X-ray pulses (first, blue) and of the maxima of the neutron pulses (second, red) by their time-of-flights for 2.5-MeV neutrons.

Positions of the PMT + S No. 2 in the simulation experiments	III	II	I	IV	V	VI	VII
Distances l [m] in a horizontal plane from the source to the PMT + S No. 2	1.9	1.42	1.1	1.5	4.5	3.655	3.6
Observation angles θ° to the PMT + S No. 2 from the neutron source	150°	129°48′	90°	47°10′	37°	11°30′	0°
Energy of the maxima of the first peak of neutron pulses measured in the simulation experiment (MeV)	2.08	2.21	2.45	2.83	2.99	3.28	3.07

Table 8.

Data on the angular tracking of energy distribution of neutrons at the PF-6 device in the hall with a simulator of a tokamak section (the PF-1000U discharge chamber) with angles and distances in a horizontal plane with Z-axis of both devices and PMT + Ss.

The values calculated from the OTs for the simulation experiment are shown in **Table 8** and in a polar diagram (**Figure 24**) where the “clean-room” conditions are depicted by blue color (a lower half-plane) and the simulator experimental data are presented by the red one (the upper half-plane).

The circles in this polar diagram have the same meanings as above: 2.0, 2.5, 3.0, and 3.5 MeV outwards.

From this diagram and the table, one may see that the difference in energy values between “clean-room” conditions and simulation experiments observed almost at all angles is not very much. The real change may be seen in forward direction along Z-axis. It is not surprising—namely in this zone, we have the most serious obstacles in the PF-6 and in the PF-1000U chambers (the stainless steel supplement of the PF-6 device, electrodes of the PF-1000U facility, and several metallic disks for vacuum preservation) that can lead to multiple scattering of even high-energy neutrons. But these features are not the only ones. Some other OTs demonstrate facts connected with the movable stand No. 2 when it is placed in large distances from the PF-6 device and at angles below 90°. In these positions (IV, V, VI, and VII), PMT + S-4 registered hard X-ray and neutron pulses passed through the PF-1000U chamber and interacting with its material. Among them:

- Amplitudes of the pulses became lower by more than 100 times than at 1 m.
- Multiple peaks are observed in the OTs of the movable stand beside the main peaks of hard X-rays and neutrons.
- Extended tail of the neutron pulse has additional peaks.

The first detail cannot be explained by the larger distance only: the quadratic law results in only an order of magnitude lower value [e.g., $(l_V = 4.5 \text{ m}/l_I = 1.1 \text{ m})^2$], that is, it gives merely a coefficient about 16. It means that we have in reality a strong absorption and scattering of hard X-rays and neutrons by our simulator.

The second characteristic gives a certain difficulty in interpretation. It appears that the first set of pulses following the main hard X-ray pulse cannot be attributed to the neutron ones because their energy calculated on the TOF bases gives a value much higher compared with the initial ones (above 10 MeV). Examination with high magnification of hard X-ray pulse shapes of the low intensity obtained at small distances by the probe No. 1 has shown that they have the same multiple peaks as in the probe No. 2 at large distances. Moreover, it appears that these subsequent pulses contain higher energy X-ray photons compared with the first pulse. We observe already in our earlier experiments such a phenomenon (see e.g., [23, 24]). Because

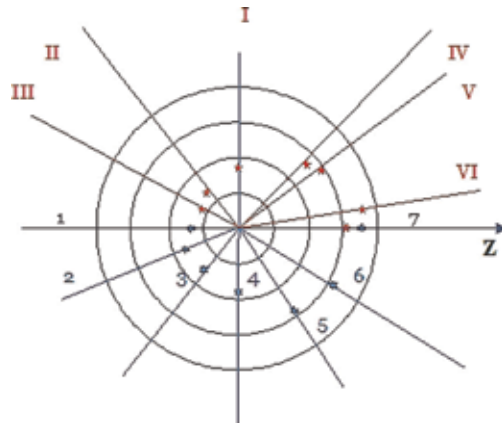


Figure 24.

A polar diagram showing angular energy distribution around a simulator (upper hemisphere, red) versus the angular tracking of neutron energy distribution in the “clean-room” conditions (lower hemisphere, blue).

of the higher energy of photons, a penetrability of each subsequent pulse appeared to be greater than the previous ones. That is why these pulses are sounder in these OTs. Their origin is the multiple current disruptions after the main one taking place during the DPF operation.

Multiple peaks and a very long “tail” of the neutron pulse is explained by neutron reflections and scattering on various elements of the PF-1000U chamber and its auxiliary equipment. We were able to attribute one neutron pulse (a quite high peak) to a real object-scatterer in the OT of the probe No. 2 at its VI position. It appears that the scatterer is a high-pressure cylinder with deuterium (10 liters, 150 atm) placed close to the PF-6 device.

6. Conclusions

1. The analysis provided above has demonstrated that the powerful nanosecond neutron pulses generated by a dense plasma focus device open very promising perspectives in taxonomy of the large main-stream nuclear fusion reactor’s chamber. Such extremely bright neutron flashes allow using simultaneously two neutron measurements methodologies—a number of activation techniques and a time-of-flight method—that are able to characterize big chambers of nuclear fusion reactors as neutron scatterers and absorbers. They can fix the most important elements distorting the main characteristics of 3-D neutron fields around them—anisotropy of neutron flux densities and neutrons spectra.
2. Measurements of absolute neutron yield and spectra in seven directions around the neutron source (i.e., the anisotropy of the yield) based on the PF-6 device in the most “clean” (with a minimum of scatterers and absorbers of neutrons) environment has been fulfilled successfully for characterization of the source itself.
3. Subsequent measurements of neutron flux densities and spectra in seven directions around the neutron source based on the PF-6 device in the presence of a simulator of a section of a main-stream fusion facility of the tokamak type (i.e., anisotropy of the yield) have been provided.

4. MCNP calculations with and without a simulator of a section of the mainstream fusion facility have been executed to fix the most important scatterers and absorbers in the experiment.
5. It was found by these modeling, what are the types of influences produced by the environment in both cases on the absolute neutron yield, its angular distributions, and the angle tracking of neutron spectral mapping.
6. Absolute neutron yield calculated over the whole spectrum of neutrons for the detectors in all directions is higher compared with the “vacuum” case by about 10–20% due to multiple scattering of neutrons in the PF-1000U chamber and its environment.
7. The distortions inserted by multiple neutron scattering become important in a very low energy “tail” of the oscilloscope traces and they cannot be observed by PMT + S probes. So, we have to use neutron activation counters to fix these features constructing the anisotropy of the neutron yield.
8. Just opposite to the above-mentioned case, a decrease of the number of fast neutrons due to absorption/scattering can be detected namely by the fast probes technique.

Acknowledgements

This research was provided partially in the frame of the R.F. state task No. 075-00746-19-00 and was supported by the International Atomic Energy Agency (grants IAEA CRP nos. 17167, 19248, 19253, 22745 and 23664).

Author details

Vladimir Gribkov^{1,2*}, Barbara Bienkowska^{1,2}, Slawomir Jednorog³, Marian Paduch³ and Krzysztof Tomaszewski⁴

1 Interregional Public Institution Moscow Physical Society, Moscow, Russia

2 A.A. Baikov Institute of Metallurgy and Material Science, Moscow, Russia

3 Institute of Plasma Physics and Laser Microfusion, Warsaw, Poland

4 ACS Ltd., Warsaw, Poland

*Address all correspondence to: gribkovv@rambler.ru

IntechOpen

© 2019 The Author(s). Licensee IntechOpen. This chapter is distributed under the terms of the Creative Commons Attribution License (<http://creativecommons.org/licenses/by/3.0>), which permits unrestricted use, distribution, and reproduction in any medium, provided the original work is properly cited. 

References

- [1] Gribkov VA, Bienkowska B, Paduch M. Examination of a chamber of a large fusion facility by means of neutron activation technique with nanosecond neutron pulse generated by dense plasma focus device PF-6. *Fusion Engineering and Design*. 2018;**125**: 109-117. DOI: 10.1016/j.fusengdes.2017.10.023
- [2] Available from: <http://www.ccfе.ac.uk/jet.aspx>
- [3] Available from: <http://www.ipp.mpg.de/16900/w7x>
- [4] Available from: <https://www.iter.org/>
- [5] Available from: <https://www.vniief.ru> and <https://lasers.llnl.gov/>
- [6] Available from: <http://www.sandia.gov/z-machine/>
- [7] Stygar W, Austin K, Awe T, Bailey J, et al. Conceptual design of a 960-TW accelerator powered by impedance-matched Marx generators. In: Proc. of the IEEE 21st International Conference on Pulsed Power (PPC); 18-22 June 2017; Brighton East Sussex, United Kingdom. Available from: <https://ieeexplore.ieee.org/document/8291256/>
- [8] Bernard A, Bruzzone H, Choi P, Chuaqui E, et al. Scientific status of dense plasma focus researches. *Journal of the Moscow Physical Society*. 1998;**8**: 93-170
- [9] Scholz M, Miklaszewski R, Gribkov VA, Mezzetti F. PF-1000 device. *Nukleonika*. 2000;**45**(3):155-158
- [10] Scholz M, Bienkowska B, Gribkov VA. Dense plasma focus for applications in positron emission tomography, Czechoslovak. *Journal of Physics*. 2002;**52**(Supplement D): D85-D92
- [11] Gribkov VA, Karpinski L, Strzyzewski P, Scholz M, Dubrovsky AV. New efficient low-energy dense plasma focus in IPPLM. *Czechoslovak Journal of Physics*. 2004; **54**(Suppl C):C191-C197
- [12] Gribkov VA, Dubrovsky AV, Scholz M, Jednorog S, et al. PF-6—an effective plasma focus as a source of ionizing radiation and plasma streams for application in material technology, biology and medicine. *Nukleonika*. 2006;**51**(1):55-62
- [13] Yurkov DI, Dulatov AK, Lemeshko BD, Golikov AV, et al. Pulsed neutron generators based on the sealed chambers of plasma focus design with D and DT fillings. *Journal of Physics: Conference Series*. 2015;**653**:012019. DOI: 10.1088/1742-6596/653/1/012019
- [14] Jednorog S, Szydłowski A, Bienkowska B, Prokopowicz R. The application of selected radionuclides for monitoring of the D–D reactions produced by dense plasma-focus device. *Journal of Radioanalytical and Nuclear Chemistry*. 2014;**301**(1):23-31
- [15] Tilley DR, Cheves CM, Godwin JL, et al. Energy levels of light nuclei $a = 5, 6, 7$. *Nuclear Physics A*. 2002;**708**:3-163
- [16] MCNP—A general Monte Carlo N—Particle Transport Code, Version 5, X-5 Monte Carlo Team LANL; 2003
- [17] MCNP5DATA: Standard Neutron Photoatomic, Photonuclear, and Electron Data Libraries for MCNP5 (CCC-710). Vol I. Available from: <http://www-xdiv.lanl.gov/projects/data/nuclear/mcnpdata.html>
- [18] Bienkowska B, Prokopowicz R, Scholz M, Kaczmarczyk J, Igielski A, Karpinski L, et al. Neutron counter based on beryllium activation. In: AIP

Conference Proceedings 1612. 2014.
pp. 105-108. DOI: 10.1063/1.4894033

[19] Available from: <http://www.acs-tm.pl>

[20] Curtiss LE. Introduction to Neutron Physics. Princeton, NJ: Van Nostrand; 1959. p. 380

[21] Vlasov NA. Neutrons (*Neitrony*), M: Nauka. 1971. p. 551 (in Russian)

[22] Gribkov VA, Banaszak A, Bienkowska B, Dubrovsky AV, Ivanova-Stanik I, Jakubowski L, et al. Plasma dynamics in PF-1000 device under the full-scale energy storage: II. Fast electrons and ions characteristics versus neutron emission parameters, and the gun optimization properties. Journal of Physics D: Applied Physics. 2007;**40**: 3592-3607

[23] Gribkov VA, Miklaszewski RA, Chernyshova M, Scholz M, et al. A single-shot nanosecond neutron pulsed technique for the detection of fissile materials. Journal of Instrumentation. 2012;7:C07005. DOI: 10.1088/1748-0221/7/07/C07005

[24] Gribkov VA. The "FLORA" facility (DPF of Filippov geometry of electrodes with pulsed laser on neodymium glass) for investigations of dense magnetized plasma and combined interaction with it of powerful laser light and streams of charged particles. In: Encyclopedia of Low Temperature Plasma. Fortov VE, Series B, editors. Vol. IX-3: Radiation plasma-dynamics": Moscow, Yanus-K, pp. 40-130 (in Russian)

Experimental Studies of and Theoretical Models for Detachment in Helical Fusion Devices

Masahiro Kobayashi and Mikhail Tokar

Abstract

Good plasma performance in magnetic fusion devices of different types, both tokamaks and helical devices, is achieved normally if the plasma density does not exceed a certain limit. In devices with a divertor, such as tokamaks JET, JT-60U, and heliotron large helical device (LHD), by approaching the density limit, the plasma detaches from the divertor target plates so that the particle and heat fluxes onto the targets reduce dramatically. This is an attractive scenario for fusion reactors, offering a solution to the plasma-wall interaction problem. However, the main concerns by realizing such a scenario are the stability of the detached zone. The activity on the heliotron LHD aimed on detachment stabilization, by applying a resonant magnetic perturbation (RMP) and generating a wide magnetic island at the plasma edge, will be reviewed. Also, theoretical models, explaining the detachment conditions, low-frequency oscillations at the detachment onset, and mechanisms of the detached plasma stabilization by RMP, will be discussed.

Keywords: helical device, LHD, detachment, resonant magnetic perturbation, nonlinear oscillations, modeling

1. Introduction

Handling of power loads onto divertor target plates is one of the most critical problems by the realization of a nuclear fusion reactor. The divertor configuration foreseen for ITER (International Thermonuclear Experimental Reactor) has been designed on the basis of present knowledge on physics and is currently available through most advanced engineering technology. It is presumed to handle a total heat load up to 100 MW, which is, however, expected to be reached during the DT (Deuterium-Tritium) plasma phase [1]. In devices beyond ITER, for example, DEMO (Demonstration Power Station), even much higher heat fluxes into the divertor volume are expected. Therefore, up to 90% of power, coming out of the confinement region, has to be removed before the plasma contacts the divertor plates to guarantee a long enough lifetime of the targets [2]. One of the most attractive ways to reach this is the realization of the state where the plasma is detached from the plates, and the energy is mostly dissipated through the radiation from impure particles in the whole divertor volume. The understanding of the detachment mechanisms and searching

for possibilities to reliably control the strongly radiating divertor plasma, being simultaneously compatible with the confinement requirements for the plasma core, is one of the most important issues for fusion studies.

Although axis-symmetric tokamaks are presently the most advanced concept for the realization of the magnetic fusion, studies of the detachment in helical devices [3, 4] are also of high interest and importance for the reactor design. Because of inherently nonaxisymmetric magnetic configurations, the magnetic field topology in heliotrons has unique features, in particular, the existence of magnetic islands and stochasticity of field lines. The magnetic field in helical systems is completely generated by currents in external coils. Therefore, the field topology and its effects on the plasma transport and, in particular, on the plasma detachment conditions and characteristics can be studied by varying the magnetic structure in a wide range. Moreover, such investigations are also useful for tokamak devices, where recently resonant magnetic perturbations (RMP) have been introduced to mitigate excessive divertor power load [5, 6]. Due to RMP, the magnetic field in tokamaks exhibits similar structure as in helical devices, that is, with the presence of magnetic islands and stochastic field lines. Thus, the understanding of detachment features in heliotrons is, therefore, of general interest for magnetic fusion program.

The structure of the present chapter is as follows. In next section, we briefly review the features and main differences in the detachment phenomena in tokamaks and helical devices. Experimental observations on the detached divertor plasmas in LHD without and with the application of RMP are presented. The RMP generates a broad magnetic island embedded in the intrinsic edge stochastic layer, which significantly influences features such as the impurity radiation, divertor foot prints, and detachment stability. The impacts on the core plasma transport characteristics during the detached discharge phase are also analyzed here. In Section 3, an interpretation of the detachment phenomena and features of detached plasmas based on the edge plasma energy balance is presented. In Section 4, different mechanisms of nonlinear oscillations during the detachment onset both in helical devices and in tokamaks are discussed. Conclusions are summarized in Section 5.

2. Experimental observations on detachment in the heliotron LHD and comparison with tokamaks

2.1 Main characteristics of divertor plasmas

By rising the plasma density in tokamaks, the plasma in the scrape-off layer (SOL) and divertor goes through several qualitatively different “regimes” [7]. At a low density level, neutral particles, appearing by the recombination of electrons and ions on the divertor target plates, escape freely into the confined plasma volume. Here, these so-called recycling neutrals are ionized and charged species generated diffuse across the magnetic field back into the SOL. Such a particle convection effectively transports heat coming from the plasma core, and the temperatures of the plasma components vary weakly along the magnetic field in the SOL. This regime is referred as either the sheath-limited one or as that of a weak recycling.

With the increasing plasma density, the fraction of recycling neutrals ionized in the vicinity of the targets is growing up. Therefore, beyond the recycling zone, the plasma convection becomes relatively weaker. As a result, a significant parallel temperature gradient develops in the main part of the SOL and the energy toward the targets is transported predominantly by the heat conduction. This regime is called as the conduction limited or a high recycling one. On the one hand, due to the strong temperature dependence of the parallel heat conductivity, $T^{2.5}$, the temperature in

the SOL changes weakly with parameters such as the plasma density at the separatrix, n_s , being comparable with the density in the confined plasma, and the heat flux from the core. On the other hand, the plasma density near the divertor targets, n_t , and the plasma flux to the targets, Γ_t , rise rapidly with n_s , as $n_t \propto n_s^3$ and $\Gamma_t \propto n_s^2$, respectively [8]. As a result, the divertor plasma can be brought into a state of a very high density of $10^{20-21} \text{ m}^{-3}$ and a temperature below 5 eV. Under these conditions, the impurity radiation plays an important role in the divertor power balance.

Contrarily to tokamaks in helical devices, such as LHD and W7-AS, it has been found that the SOL and divertor plasma characteristics do not show such strong nonlinear variation with n_s , even if this is already close to the threshold at the detachment onset, $n_t \propto n_s^{1-1.5}$ [9, 10]. It has been interpreted as a result of the momentum (pressure) loss in the stochastic field line region [11, 12] or in the island divertor structure [10]. In these regions, parallel plasma particle flows, along flux tubes of very different connection lengths or even streaming in opposite directions [13], are strongly interconnected through the cross-field momentum transfer. Therefore, the divertor plasma density remains relatively low, of 10^{19} m^{-3} , and the temperature relatively high, of 10 eV, till the detachment transition [9]. (Numerical simulations for W7-X [14] predict, however, a high recycling regime, due to the larger spatial separation of the counter-streaming flows in the larger island.)

Nonetheless, experimental observations demonstrate that in the LHD impurity radiation plays an important role for the divertor plasma cooling, detachment onset, and stability conditions. Here, however, the main radiation source is not located in the divertor legs but in the stochastic layer. **Figure 1** shows the tomographic reconstruction of carbon impurity emission in the edge stochastic layer of LHD just before the detachment transition, as well as the magnetic field line connection length (L_C) [15]. Although, the emission of low charge state, CII (C^{1+}), is distributed along divertor leg and the very periphery of the stochastic layer, that from the higher charge state, CIV (C^{3+}), being the main radiating species [16], comes from the stochastic layer only.

In the LHD, studies on the divertor detachment are performed by seeding impurities deliberately [17–19] and by applying RMP from special coils [20–22]. In this chapter, we focus on the detachment with the RMP application, which is a unique feature of the LHD.

2.2 RMP impact on the edge impurity radiation and stability of detached plasma

The large helical device, LHD, is a heliotron-type fusion machine, in which the magnetic field is produced by superconducting coils with poloidal and toroidal

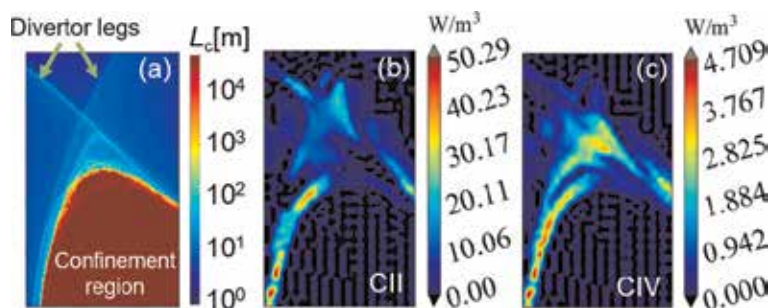


Figure 1. The pattern of the connection length L_C in the edge stochastic layer of LHD (a); the tomographic reconstruction of the emission from carbon ions CII (514 nm) (b) and CIV (466 nm) (c), recorded just before the detachment onset, at line averaged plasma density $\bar{n}_e = 5 \times 10^{19} \text{ m}^{-3}$.

winding numbers $l = 2$ and $n = 10$, respectively [23]. **Figure 2(b)** displays a poloidal cut of the calculated magnetic field structure in the edge region and the distribution of connection length L_C . The magnetic field in helical devices is completely generated by currents in external coils and has a broad spectrum of Fourier harmonics of different mode numbers m and n . Each of those generates magnetic islands, and by overlapping of the islands, the magnetic field structure becomes stochastic. The divertor legs, named left and right legs, are connected to the L and R divertor plates, respectively, rotating helically by moving in the toroidal direction. The lower half of the **Figure 2** presents the L_C distribution with RMP of $m/n = 1/1$, where the remnant island structure embedded into the stochastic layer is visible.

Figure 3 shows the time evolution of several plasma parameters in discharges with and without RMP where the density ramp up was performed without auxiliary impurity seeding, and the edge radiation was coming mainly from carbon impurity sputtered from the divertor target plates. On the one hand, without RMP (blue lines), the growth of the density leads to a sudden increase of the radiated power, see **Figure 3(b)**, and, finally, to the radiation collapse of the whole plasma. On the other hand, with the RMP application (red lines), the radiated power is saturated at a higher level and the state with the plasma detached from the divertor targets is sustained during the whole later phase of the discharge. This is demonstrated in **Figure 3(a)** by the evolution of the heat load onto the divertor target. The strong cooling of the edge plasma by impurity radiation leads to the decrease of the plasma column effective radius a_{99} displayed in **Figure 3(d)**.

Figure 4 shows the radial profiles of the electron temperature T_e , density n_e , and pressure in the edge region along the LHD mid-plane, in the attached and detached discharge phases [24]. With the RMP application, a clear flattening of the T_e profile due to the magnetic island is observed at the outboard, $R = 4.60$ – 4.75 m, in the attached phase. The increase in the density leads to the lowering of T_e , and during the detached phase, T_e inside the island is sustained at ~ 20 eV. It is also interesting to note that with the growing n_e , the width of the region with the profile flattening becomes slightly narrower, and at the same time, a region with the flattening appears

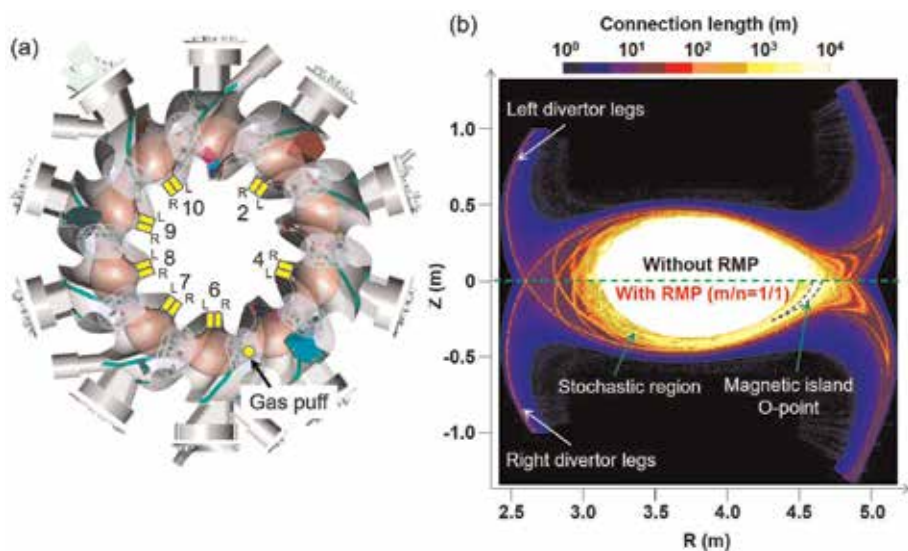


Figure 2.

Top view of the LHD torus with the position of divertor probe arrays at the inboard, indicated by numbers and letters “L” & “R” (a); L_C distribution in the edge region of LHD, without (upper half) and with (lower half) RMP application (b). The right and left legs, indicated in the figure, are connected to L and R divertor arrays, respectively.

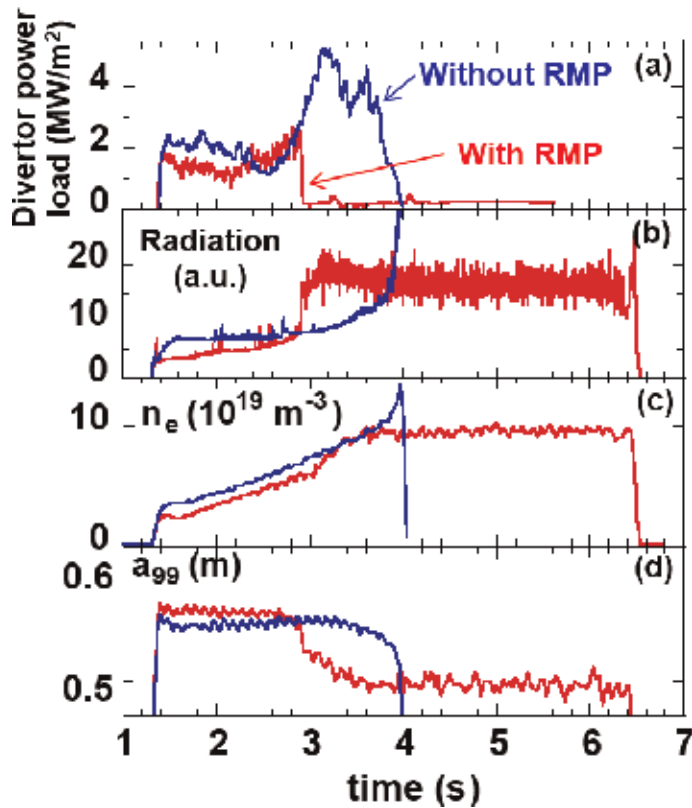


Figure 3. Time evolution of plasma parameters in the LHD density ramp-up discharges, with (red) and without (blue) the RMP application: The power load onto divertor targets measured by probes (a), the radiated power measured by AXUV (b), line averaged density (c), and the effective plasma minor radius a_{99} defined as that of the flux surface, containing 99% of the total plasma energy (d).

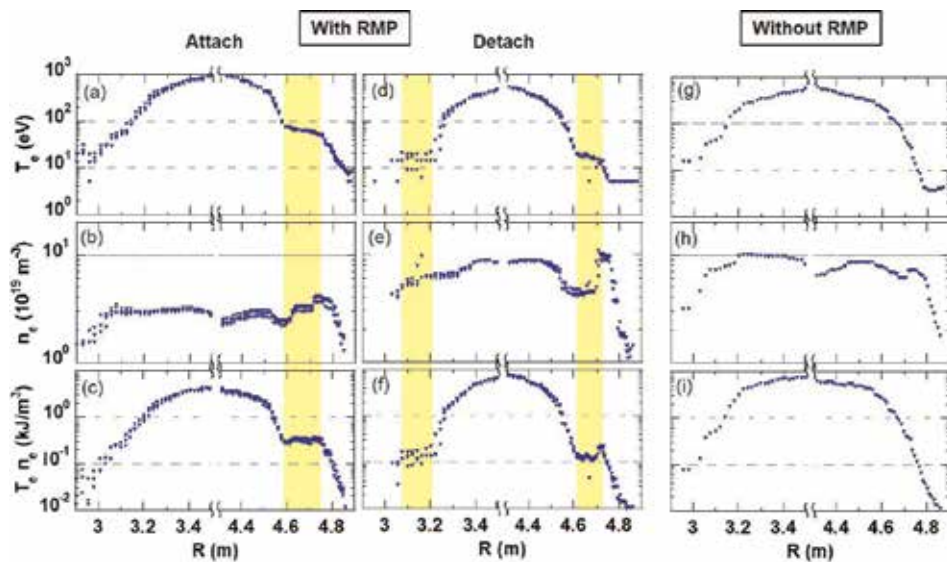


Figure 4. Radial profiles of the plasma parameters in the LHD edge region: electron temperature (a, d, g), density (b, e, h), and pressure (c, f, i); the panels (a–f) correspond to discharges with RMP, (g–i)—without RMP. The region of the T_e flattening caused by the magnetic island is indicated by yellow patch [24].

at the inboard, $R = 3.1\text{--}3.2$ m. This is interpreted as a result of the plasma response to the external RMP field. Indeed, the measurements with a saddle loop coil indicate the reduction of the total field perturbation by RMP induced by the currents in the plasma under the attached conditions and its amplification during the detached phase [20, 25, 26]. A similar flattening appears in the pressure profiles, while density is relatively flat in the entire edge region with some modulations around the magnetic island. Without RMP application, there is no such flattening except for a small modulation due to the inherent small remnant islands of higher mode numbers.

The edge impurity radiation profiles are estimated using the T_e and n_e profiles presented in **Figure 4** and by assuming a concentration of carbon of 1% with respect to n_e . **Figure 5** shows the temporal evolution of the radiation profiles together with L_C distributions [24]. Without RMP, **Figure 5(b)**, the impurity radiation starts to peak around the X-point of the divertor leg, at $R \sim 4.8$ m, and later moves gradually radially inward due to the decrease in the temperature as the density increases; the X-point of the divertor leg should be distinguished from that of the magnetic island created by the RMP. Finally, the radiation penetrates into the confinement region at $t = 4$ sec, leading to the radiation collapse, as shown in **Figure 3**. With the RMP application, **Figure 5(a)**, a bundle of flux tubes of long connection length appears at the edge, as a remnant island. The radiation starts to peak at the X-point of the divertor leg and moves radially inward, similarly to the case without RMP. It is, however, stopped at the periphery of the edge of the island, $R \sim 4.75$ m, without penetrating into the confinement region at the detachment transition, $t = 2.9$ sec. Then, the discharge is sustained until the end of NBI heating due to the stabilization of the radiation profile by the island.

Radiation profile measurements have been performed to capture the change of the global structure of impurity emission due to RMP and are compared with numerical transport simulations with the code EMC3-EIRENE [20–22]. **Figure 6** shows the calculated impurity radiation distribution, with and without RMP, and

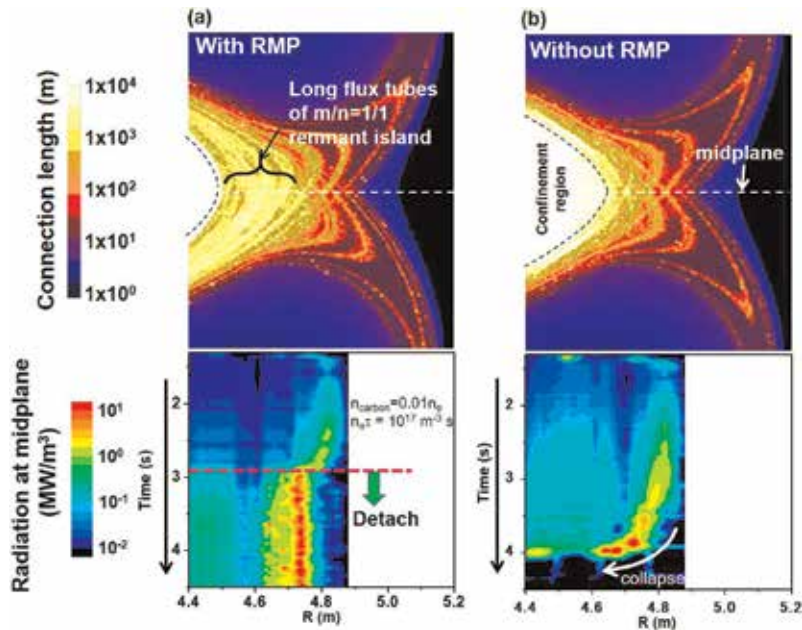


Figure 5. The calculated L_C distribution in the outboard edge region (upper panels); time evolution of the carbon radiation estimated from T_e and n_e profiles as shown in **Figure 4**, by assuming 1% carbon concentration and noncoronal cooling rate at $n_e \tau = 10^{17} \text{ m}^{-3} \text{ s}$ (lower panels), with (a) and without (b) RMP [24].

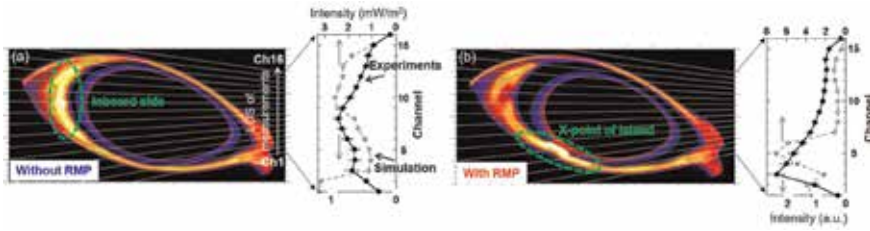


Figure 6. Carbon impurity radiation distribution calculated by EMC₃-EIRENE at poloidal cross section, together with line-integrated profile of the simulation and measurements by AXUV, on the right panel, without (a) and with (b) RMP [20].

the radiation profile measured by the AXUV diagnostics [20]. Without the RMP application, the impurity radiation is enhanced at the inboard as it is demonstrated in **Figure 6(a)**. The line integrated radiation profile found both in the measurements and in simulations are shown in the right panel. Both profiles have maxima at the center channels, which pass through the enhanced radiation at the inboard location. With the RMP, the peak of the radiation moves to the bottom of the plasma, where the X-point of the $m/n = 1/1$ island is located (note that the toroidal angle positions of the cross sections are different in **Figures 2(b)** and **6**). The simulation also shows a peak at the bottom channel in accordance with the measurement. The measurements by imaging bolometer also indicate enhanced radiation around X-point in agreement with the numerical simulation [21].

The impact of RMP on the impurity emission intensity was also investigated in the VUV range with the diagnostic equipment [22], viewing the entire plasma toroidal cross section. Density dependence of the radiated power measured by the resistive bolometer, together with emissions from different charge states, CIII (C^{2+}), CIV (C^{3+}), CV (C^{4+}), and CVI (C^{5+}), measured with the spectrometer [27] is plotted in **Figure 7**. Here, the plasma density is normalized to the density limit in helical devices, n_{sudo} [28]. It is seen that without RMP, the radiated power shows rapid increase around the density limit, that is, $\left. \frac{\partial P_{\text{bolo}}}{\partial n_e} \right|_{\text{without RMP}} \rightarrow \infty$. This means that any small density perturbation leads to a significant change in the radiation; that is, the system in question is becoming unstable. With RMP, the radiation is enhanced in the low-density range even in the attached phase. The increase of the radiation with RMP is interpreted due to the enlarged volume inside the edge magnetic island with a low T_e , of 10–20 eV where the radiation of low charged carbon ions approaches its maximum. After the detachment transition, there appears a region where the radiation is insensitive to the density, that is, $\left. \frac{\partial P_{\text{bolo}}}{\partial n_e} \right|_{\text{with RMP}} \rightarrow 0$. This provides a possibility to the radiation level control and, thereby, the detachment stability. One can see that the “flat” region extends slightly beyond the density limit, which results in an extension of density operation range for the case with RMP. Very similar density dependence as for the bolometer measurement is observed in the emission of CIII and CIV species, being the dominant radiating charge states, see **Figure 7(b)** and **(c)**. As it is analyzed in Ref. [16], CIV is providing the largest contribution to the total radiated power. On contrary, with RMP, the radiation of CV and CVI ions increases monotonically with the plasma density, and is larger than without RMP. Since the ionization energies of CV and CVI ions, 392 and 490 eV, respectively, are much higher than the T_e inside the magnetic island, the higher emission intensity might indicate enhanced penetration of impurity toward the core boundary. The contribution of CV and CVI to the total radiated power is, however, small compared to the states of lower charges [16].

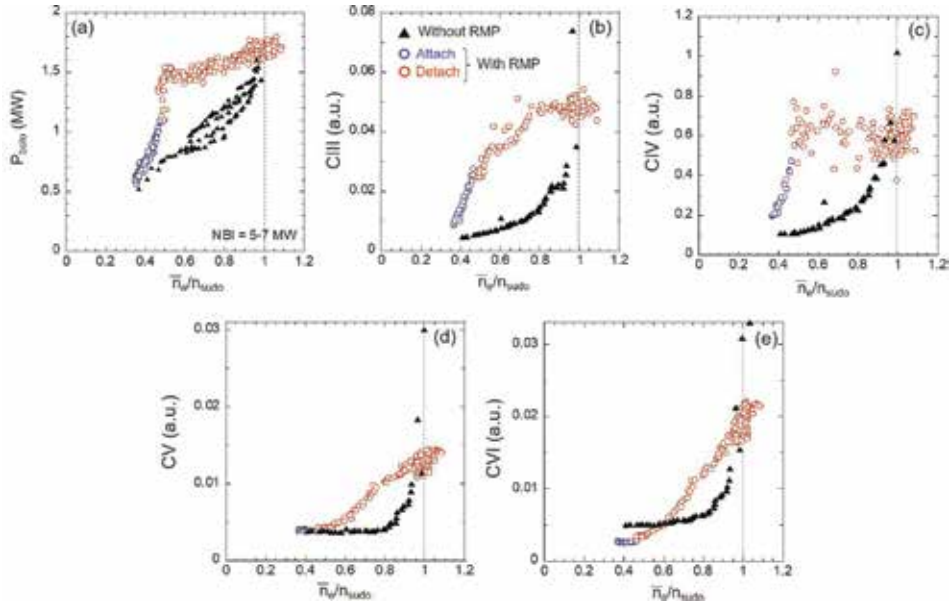


Figure 7. Density dependence of the radiated power measured by the bolometer (a), the emissivity of CIII (b), CIV (c), CV (d), and CVI (e) species measured by VUV spectrometer without (triangles) and with (circles) RMP. The density is normalized to the density limit in helical devices, n_{sudo} [27].

The results above clearly show the difference of edge impurity radiation and transport with and without RMP. This is of high importance for the detachment stabilization in the former situation. The mechanism of the stabilization of the radiation layer is under investigation by taking into account the magnetic geometry, the particle, and the energy transport, both parallel and perpendicular to the field lines within and out of the magnetic island. Similar observations of the detached plasma stabilization with large island were also found in W7-AS [29]. The recent results on the successful detachment control in W7-X with the island divertor also suggest an important role of the edge magnetic island for the detached plasma stability [30].

2.3 Change of divertor footprint with RMP application

The toroidal variation of the particle fluxes onto divertor plates with RMP has been investigated with Langmuir probe array installed around the mid-plane of the targets at the inboard side [17, 31]. It has been found that the time evolution of the divertor particle flux exhibits substantial difference between toroidal locations, that is, some plates are becoming detached earlier than others; at some plates, the flux even increases after detachment [27]. The summary of this behavior is shown in **Figure 8**, where the divertor particle flux normalized to its value without RMP is plotted for different toroidal sections. In the attached case, there is an $n = 1$ mode structure for both left (L) and right (R) divertor arrays, which are connected to the left and right legs, respectively, as indicated in **Figure 2**. In the detached phase, the $n = 1$ structure remains, but the toroidal phase is shifted by one section. The relation between the divertor flux and L_C profiles is presented in **Figure 9** for several toroidal cross sections [27]. At the section 6L (**Figure 9(a)** and **(b)**), a bundle of flux tubes of 6.5 mm width is connected to the divertor plate. By applying RMP, the footprint shifts toward the right side with increased L_C . The measured particle flux increases in the absolute values due to the longer L_C , as seen also in **Figure 9(a)**.

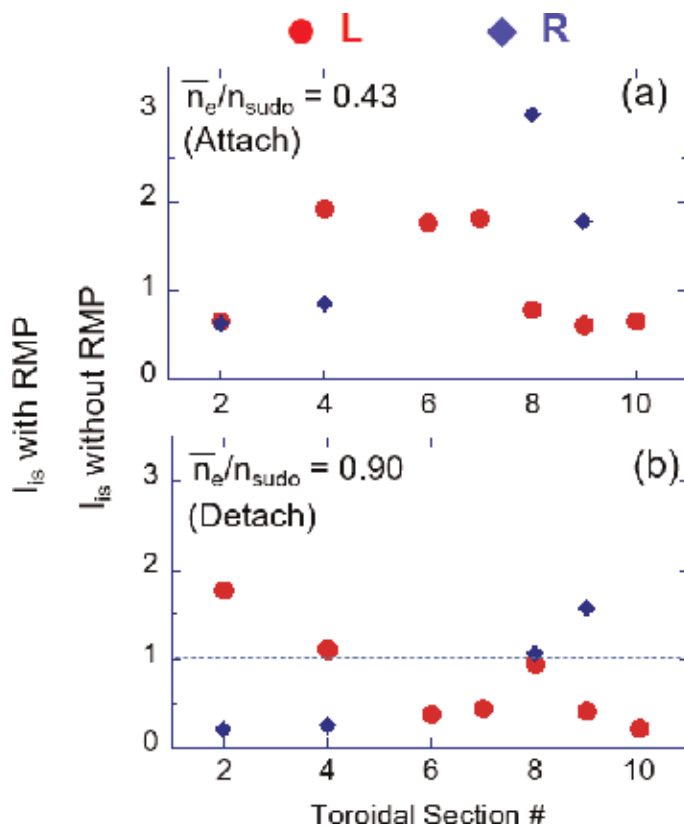


Figure 8. The toroidal distributions of the particle flux onto divertor targets with RMP normalized by the values without RMP on attached (a) and detached (b) discharge phases. Red circles correspond to the left divertor and blue diamonds to the right divertor arrays, as it is indicated in **Figure 2** by the toroidal section number [27].

The flux profile becomes more asymmetric with respect to the central peak, being increased at the right side, which reflects the right shift of the L_C footprint. On the other hand, the 2R plate shows decrease of the particle flux with the RMP application, as seen in **Figure 9(c)**. This is interpreted by the decrease in L_C , as shown in the figure, where the long L_C bundle at the central region almost disappears with RMP, and thus, the particle flux decreases as well. These results show that, to a certain extent, the particle transport is well correlated with the L_C distribution calculated in the vacuum approximation, i.e., without a plasma response to RMP, and thus can be controlled by the RMP application in the attached phase. In the detached phase, the particle flux both at 6L and 2R decreases in the entire region with respect to the case without RMP, as shown in **Figure 9(b)** and **(d)**.

In **Figure 9(e)** and **(f)**, the observations in section 2L are presented. By applying RMP, the particle flux becomes smaller in the attached phase with respect to the reference case without RMP. The flux, however, increases at the detached phase, as shown in **Figure 9(f)**. At this plate, the fraction of long flux tubes with $L_C > 100$ m decreases, but those with $L_C \sim 30$ m increases with RMP. The reduction of the flux at the attached phase may be due to the reduction of the contribution from the tubes with $L_C > 100$ m. On the other hand, in the detached phase, the increases of the flux could be attributed to the change of the particle transport channel from long, $L_C > 100$ m, to the medium, $L_C \sim 30$ m, flux tubes. This effect has to be investigated by analyzing in detail the relation between the magnetic field structure and the ionization front. It has to be taken into account that there is a significant

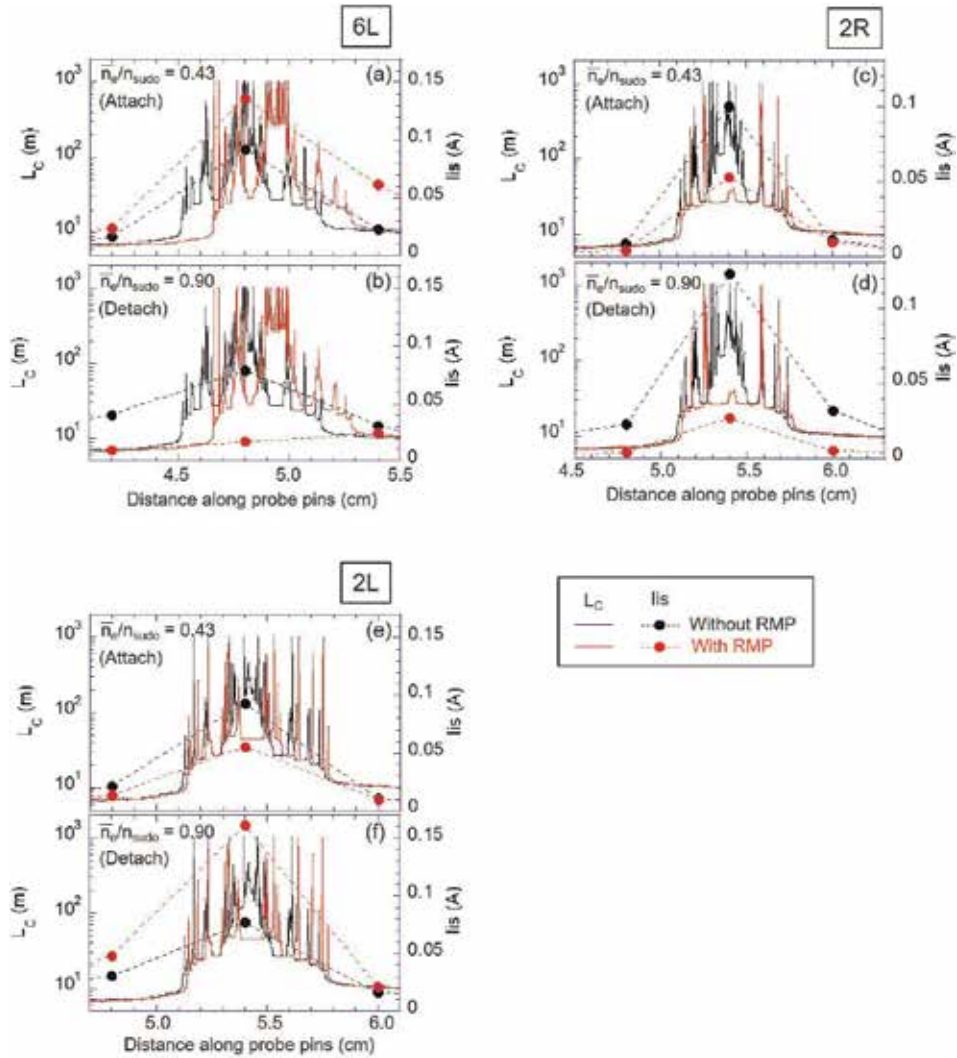


Figure 9. L_C (solid lines) and divertor particle flux (dashed lines with circles) profiles along the divertor probe pins, with (red) and without (black) RMP. (a and b) 6L, (c and d) 2R, and (e and f) 2L toroidal section, respectively [27].

plasma response to the RMP, which is different in the attached and detached phases, as mentioned above.

During the detached phase, there are large oscillation in both divertor particle flux and radiation. **Figure 10** presents the time traces of the particle flux to the divertor targets and of the radiation losses measured by AXUV during the detached phase, where oscillation with 60–90 Hz is visible. The particle flux and radiation are oscillating in phase. Similar behavior was also observed in the particle flux to the first wall [32]. The mechanism of the oscillation is discussed later in this chapter.

2.4 Operation space of detachment: amplitude and radial location of resonance layer of RMP

The parameter space of a stable discharge performance with the RMP and the plasma detached from the divertor targets has been investigated by varying the

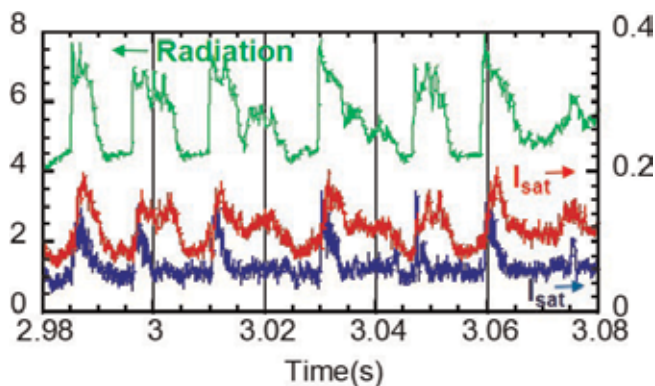


Figure 10. Time traces of the radiation losses, measured by the AXUV (green line), and that of the particle flux to divertor targets (red and blue lines) during detached phase with RMP.

RMP amplitude and location of its resonance layer. **Figure 11(a)** shows the density dependence of the radiated power at different RMP amplitudes quantified by the ratio B_r/B_0 scanned from 0 to 0.12%. The densities at the detachment onset and the radiation collapse are plotted as a function of B_r/B_0 in **Figure 11(b)**. The density range between the detachment transition and thermal collapse corresponds to the operation range with a stable detached plasma. One can see that the density at the collapse is almost independent of the RMP amplitude. With decreasing the amplitude, the detachment transition density shifts to higher density and finally merges with that where the collapse happens. For $B_r/B_0 < 0.07\%$, the RMP is almost completely suppressed by the plasma response, and thus, no stable detachment was realized. As it is seen in **Figure 11(a)**, the radiation level attained in the detached phase is almost independent of the RMP amplitude.

The radial position of the resonance layer of the $m/n = 1/1$ RMP was scanned by changing the rotational transform ι , which is an inverse value of safety factor q normally used for tokamaks. The radial profiles of T_e for different ι -configurations are plotted in **Figure 12**, where radial shift of the region with a flat T_e profile is demonstrated. As the resonance layer with $\iota = n/m = 1$ moves radially inward, the T_e in the flattening region becomes higher. This is because the island gradually penetrates into the confinement region through the LCFS, and flux surfaces in the island are becoming closed. In the configurations with the magnetic axis at $R_{\text{axis}} = 3.90$ and 3.85 m, the island is marginally outside LCFS and is embedded into the stochastic layer. The stable detachment has been realized so far only for these two configurations. The openness of the flux surfaces in the island thus ensures a low enough level

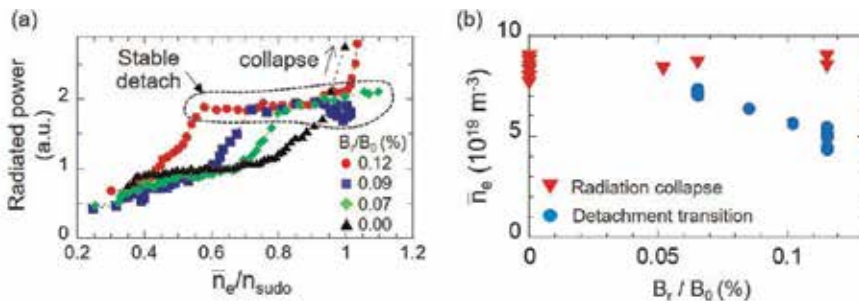


Figure 11. The radiated power as a function of density for different RMP amplitudes (a) and density at the detachment transition (circles) and radiation collapse (triangles) as a function of RMP amplitude (b).

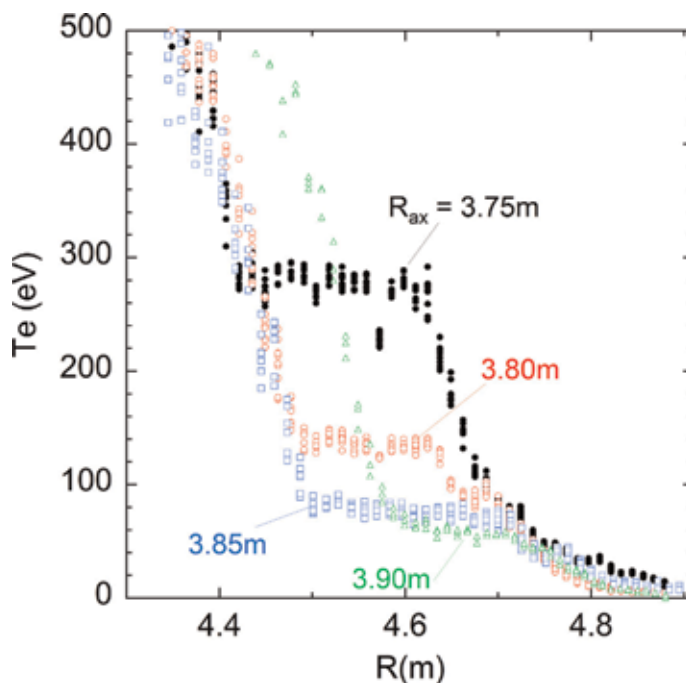


Figure 12. Radial profiles of T_e for different profiles of the rotational transform. Configurations differ by the position of the magnetic axis, R_{ax} . The stable detachment was realized for $R_{ax} = 3.85$ and 3.90 m so far.

T_e in the island and consequently a high level of the edge radiation from impurity ions of low charges.

The findings discussed above are summarized in **Figure 13**, where the radial location of the island is represented by the distance between the island X-point and the LCFS [12]. Here, the results from W7-AS are also incorporated. The operation spaces for two devices are not overlapping, which means that probably some hidden parameters important for the detachment stabilization are still missed. Nevertheless, it is seen that for stable sustainment of a detached plasma, there is a threshold value of B_r/B_0 , which is nearly the same in the LHD and W7-AS, and a certain distance between the island and the confinement region is necessary.

2.5 Compatibility with core plasma performance

The compatibility of a stable detached plasma with a good performance in the plasma core is an important issue for a fusion reactor. Temporal evolution of the radial profiles of T_e , n_e , and the electron pressure measured by Thomson scattering are plotted in **Figure 14**; $\bar{n}_e/n_{sudo} = 0.43$ and ≥ 0.5 correspond to the attached and detached phases, respectively. From the T_e and pressure profiles, one can see the shrinkage of the plasma volume observed as the RMP is applied, which is due to low T_e within the edge magnetic island. It is found that with the RMP application, the increasing density leads to a peaking of the pressure profile. This is due to the increase in n_e at the central region since the T_e profiles are almost the same with and without RMP. The energy confinement time, τ_E , and central pressure, P_{e0} , are plotted in **Figure 15**, as functions of the line averaged plasma density [27]. Systematically, τ_E is smaller with RMP, because of the plasma volume shrinkage. Without RMP, τ_E becomes saturated around the density limit, while with RMP, it increases with density slightly beyond the density limit. In **Figure 15**, one can see that the pressure peaking with RMP is enhanced especially in the detached phase. Near the

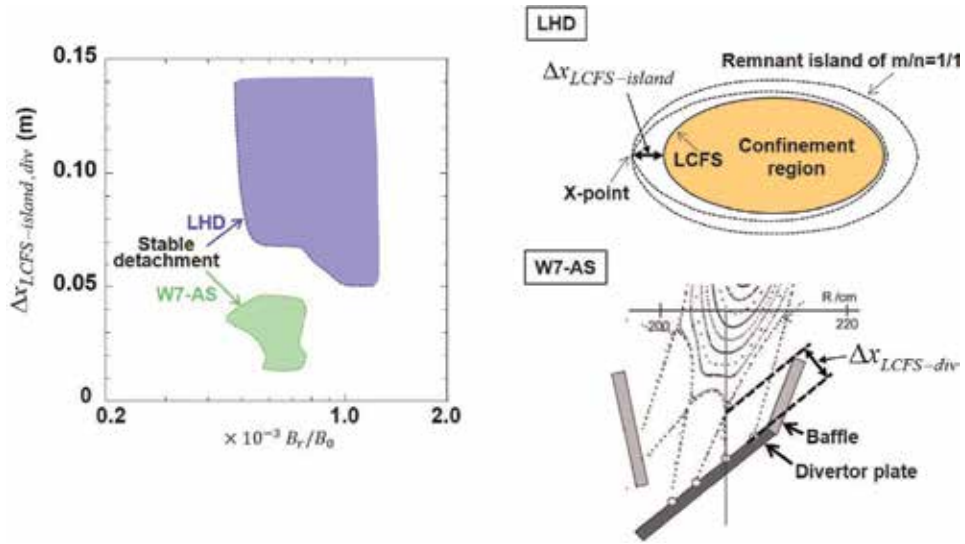


Figure 13. The operation space in the plane $\Delta x_{LCFS-island} (\Delta x_{LCFS-div})$, B_r/B_0 with a stable detached plasma in the heliotrons LHD and W7-AS [12].

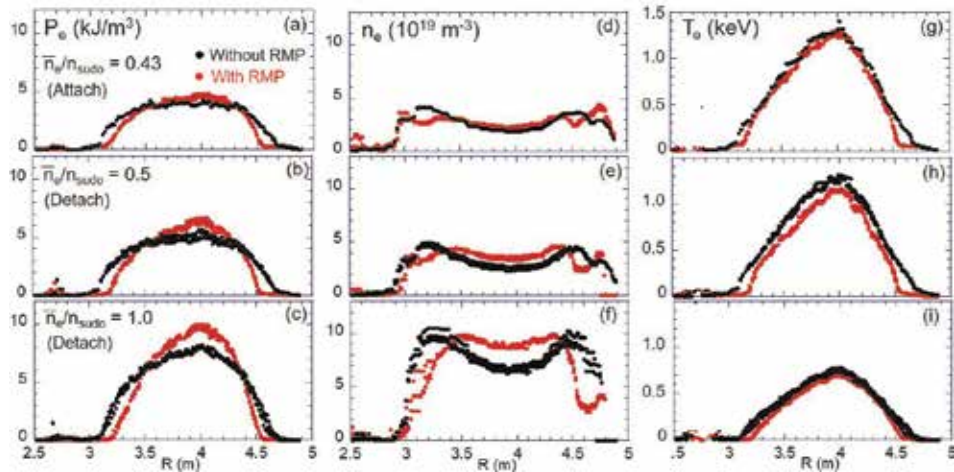


Figure 14. Radial profiles of (a–c) electron pressure, (d–f) n_e , and (g–i) T_e with (red) and without (black) RMP, for different densities, $\bar{n}_e/n_{Sudo} = 0.43, 0.5, \text{ and } 1.0$.

thermal collapse density limit, the fusion triple product, $n_0 \tau_E T_0$, becomes comparable for both cases, with and without RMP.

The global parameters are significantly affected by the change in the plasma volume caused by the RMP application. In order to study the local plasma transport characteristics, a core plasma energy transport has been analyzed with the 1-D transport code TASK3D [33]. This code calculates the heating source profile, in the present case by the NBI, by taking into account the beam slowing down and solves a heat conduction equation with n_e and T_e values measured experimentally.

Figure 16 shows the resulting NBI power deposition profiles and effective heat conductivity, $\chi_{eff} = 0.5(\chi_e + \chi_i)$, where χ_e and χ_i are those for electrons and ions and $\rho = r_{eff}/a_{99}$ is the normalized minor radius. In the attached phase, $\bar{n}_e/n_{Sudo} = 0.43$, the NBI power deposition profiles are almost identical for the both cases with and

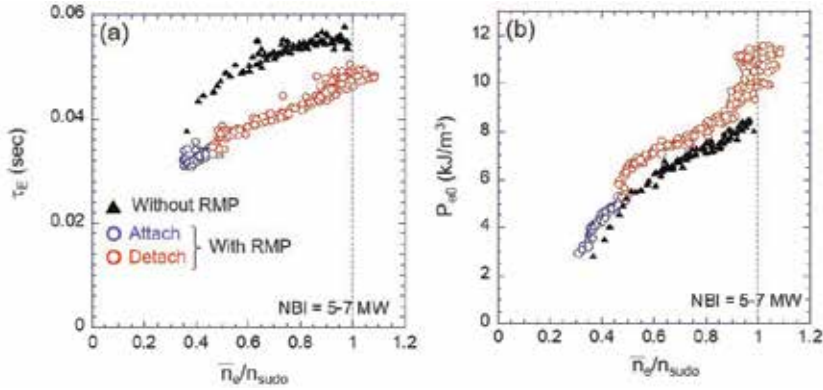


Figure 15. Density dependence of energy confinement time, τ_E , (a) and of the central pressure, P_{e0} , (b), obtained with (circles) and without (triangles) RMP [27].

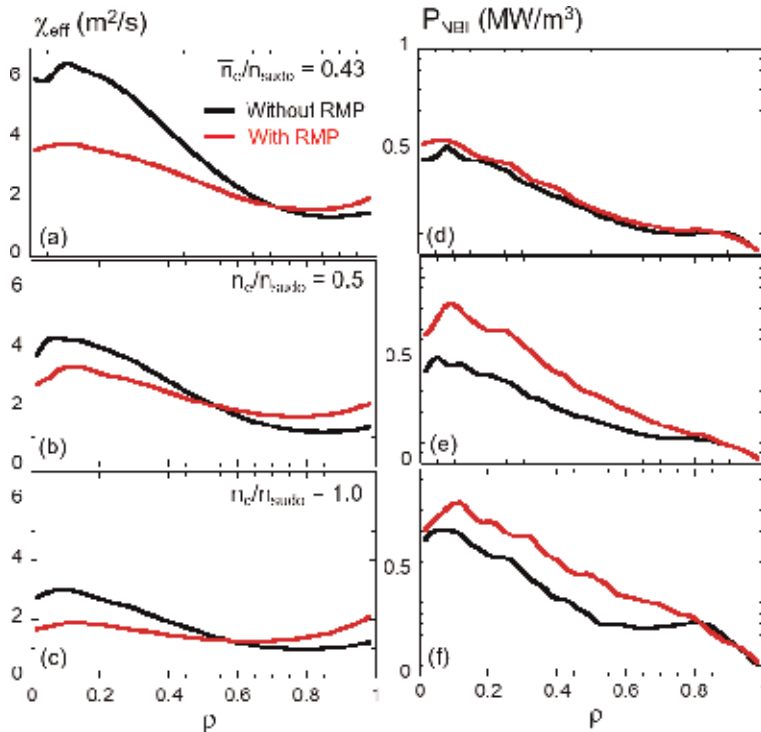


Figure 16. Radial profiles of (a–c) $\chi_{eff} = 0.5(\chi_e + \chi_i)$, and (d–f) NBI deposition, with (red) and without (black) RMP, for $\bar{n}_e/n_{Sudo} = 0.43$ (attached), 0.5 (detached), and 1.0 (detached), calculated by core transport code TASK3D.

without RMP, while χ_{eff} is smaller with the RMP in the plasma central region. The larger χ_{eff} in the very core without RMP is attributed to the flat pressure profile there, see **Figure 14(a)**. In the detached phase with $\bar{n}_e/n_{Sudo} = 0.50$ and 1.0, the NBI heating power is deposited more at the central region with RMP. This is because of a deeper penetration of the NBI due to the shrinkage of the plasma volume with the edge radiation cooling. The increased energy deposition at the central region with RMP, ~ 0.3 MW/m³, provides an addition to the particle source density ΔS_p of the order of 10^{19} 1/s/m³, estimated for an NBI particle energy of 180 keV. According to a simple

picture of a diffusive particle transport, this ΔS_p leads to a density increment of $\Delta n \sim S_p \Delta r^2 / D = 10^{17} \sim 10^{18} \text{ m}^{-3}$, with $\Delta r = 0.1 \sim 0.4 \text{ m}$ ($\Delta \rho = 0.2 \sim 0.8$), $D = 1 \text{ m}^2/\text{s}$. This level is too low to be responsible for the density increase of 10^{19} m^{-3} observed at the plasma axis with RMP, **Figure 14(e)** and **(f)**. In the inner plasma region, $\rho < 0.6$, χ_{eff} decreases significantly both with and without RMP with the increasing density, although χ_{eff} remains slightly smaller in the case with RMP. Together with the negligible effects of the NBI particle source, this indicates that the pressure peaking is probably due to the reduction of the transport. On the other hand, at the periphery, $\rho > 0.8$, χ_{eff} becomes larger with RMP. This could be due to additional stochastization caused by the RMP application. Here, the radial transport can be enhanced by flows along braiding magnetic field lines [34, 35]. The larger impurity emission with RMP, see **Figure 7**, could also lead to larger χ_{eff} because TASK3D currently does not take into account the volumetric power loss. The present findings suggest that with the RMP application, there is no significant transport degradation in the central plasma region during the detached plasma phase, compared to the case without RMP.

3. Consideration of detachment as a dissipative structure

The most visible approach to understand the detachment mechanisms is to analyze the power balance at the plasma edge by applying the concept of dissipative structures [36]. The power transported from the plasma core by the plasma heat conduction is lost from the edge region mostly through two channels: (i) the plasma particle outflow through the separatrix and (ii) the radiation of light impurities such as carbon sputtered from the divertor target plates.

On the one hand, the density of the former channel q_{con} is normally monotonously increasing with the plasma temperature T at the plasma edge. On the other hand, it is well known [7] that the impurity radiation density q_{rad} has a maximum as a function of T : by a too low temperature, electrons do not have enough energy to excite impurity species, by a too high temperature, impurities are strongly ionized and have a very large excitation energy. In particular, for carbon, the best “radiators” are the Li-like ions C^{3+} . Qualitatively, q_{con} , q_{rad} , and their sum q_{loss} are displayed as functions of T in **Figure 17**.

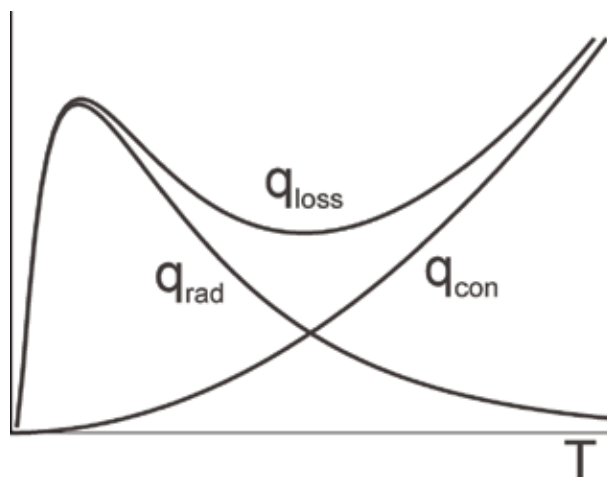


Figure 17. Temperature dependence for the energy loss channels from the plasma edge with the plasma conduction and convection through the separatrix, q_{con} , with impurity radiation, q_{rad} , and their sum q_{loss} .

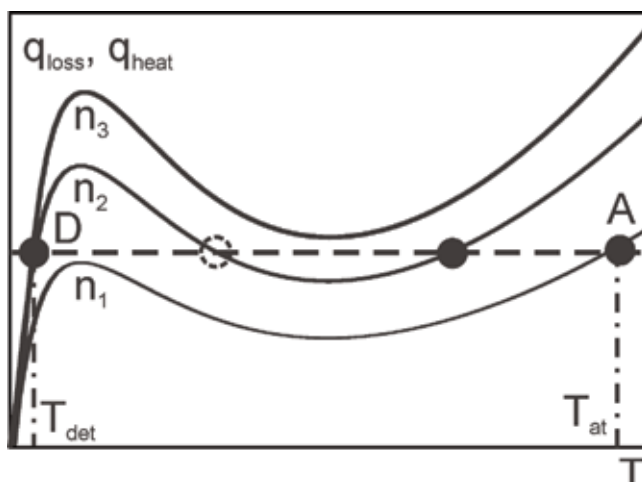


Figure 18.

Temperature dependence for the density of the energy loss from the plasma edge, q_{loss} , for three magnitudes of the plasma density $n_1 < n_2 < n_3$ (solid curves) and of the heat flux to the edge from the plasma core, q_{heat} . In a steady state, these balance each other, $q_{\text{loss}} = q_{\text{heat}}$.

Both q_{con} and q_{rad} increase with plasma density n [7]. Indeed, the larger the content of plasma particles, the higher their loss from the device. Likewise, q_{rad} increases both with the density of exciting electrons n and that of the exciting impurity species $n_I = c_I n$. Typically, the relative concentration c_I of carbon impurity in LHD plasmas is of order of 1%.

In a steady state, the energy loss from the plasma edge has to be balanced by the heat transfer from the plasma core, with the density q_{heat} , which in many cases is weakly dependent both on the edge temperature and on the plasma density.

Figure 18 shows q_{loss} and q_{heat} versus T for three magnitudes of n . One can see that a moderate increase of the plasma density from n_1 to n_3 , by less than 40%, results in a very strong drop in the stationary edge temperature, from its level T_{at} of several tens of eVs in an attached plasma state A to T_{det} of 1 eV in a detached state D. In the latter case, electrons and ions in the plasma effectively recombine one with another as it is indicated by spectroscopic measurements.

For the intermediary level of the density, n_2 , there are three steady states. It is straightforward to comprehend that the one with the in-between temperature is unstable. Indeed, an infinitesimal spontaneous deviation from this state, e.g., with diminishing T , leads to an increase of the energy losses and a further decrease of the edge temperature. Finally, the plasma will get the one of two stable states with a low temperature.

4. Nonlinear low-frequency oscillations at the detachment onset

As it was discussed in the first part of the present chapter, there is a significant difference between the detachment scenario in LHD without and with RMP. In the former case, one needs very fine tuning of the radiation level by gas puffing of fuel or impurity, and detachment onset may lead to a total radiation collapse of the discharge. Unlikely, with RMP after the transition to the detached state, the plasma density can be increased further, with corresponding growth of the radiated power and without a significant deterioration of the discharge performance. Finally, a radiation collapse occurs roughly at the same plasma density as without RMP.

Interestingly, that by the detachment onset with RMP, there is some density range where nonlinear oscillations of high amplitude and relatively low frequency of 100 Hz have been observed in diverse plasma parameters such as the radiation intensity and ion saturation current to the divertor target plates. Also in tokamaks, similar large-scale self-sustained periodic oscillations in various plasma characteristics have been seen, by approaching to critical conditions, see, for example, [37, 32]. Several models [38–40] have been proposed previously to explain these phenomena.

Here, we consider two new mechanisms. The first one is relevant for LHD, with plasma of relatively low density in its divertor legs. In such a situation, by approaching to the critical density, the plasma detaches practically directly from the periphery of the edge stochastic layer. This reminds the phenomenon of radial detachment in limiter tokamaks such as TFTR and TEXTOR. The threshold conditions for radial detachment have been analyzed in [41].

The second mechanism is pertinent for the case of tokamaks with divertors like JET, ASDEX-U, DII-D, operating before detachment in the regime of strong plasma recycling on the target plates [7].

4.1 Radial detachment

4.1.1 Stationary states

In the simplest case, the behavior of the plasma temperature T in the edge region is governed by the following heat conduction equation:

$$3n\partial_t T + \partial_x q_x = -c_I n^2 L_{rad} \quad (1)$$

where $q_x = -\kappa_\perp \partial_x T$ is the density of heat flux perpendicular to the magnetic surfaces, in the direction x , with κ_\perp being the corresponding component of the plasma heat conduction; the term on the right-hand side (rhs) is the energy loss due to impurity radiation, whose temperature dependence is determined by that of the cooling rate L_{rad} . The behavior described qualitatively in the previous section is well mimicked by the following formula [41]:

$$L_{rad} = L_{rad}^{\max} \exp \left[- \left(\sqrt{T_1/T} - \sqrt{T/T_2} \right)^2 \right] \quad (2)$$

For carbon impurity, dominating the radiation losses from the plasma edge in LHD, $L_{rad}^{\max} \approx 6.6 \times 10^{-7} eV \text{ cm}^3 s^{-1}$, $T_1 \approx 5eV$, $T_2 \approx 64eV$. In Eq. (1), we assume n , κ_\perp , and c_I invariable in time and space.

Subsequently, we multiply Eq. (1) with $2\kappa_\perp \partial_x T$ and integrate over the coordinate x , from the interface with plasma core, $x = x_c$, to the outer boundary of the stochastic layer, $x = x_s$. As a result, one gets

$$6n \int_{x_c}^{x_s} q_x \partial_t T dx = P(T_s) \equiv q_c^2 - q_s^2 - 2\kappa_\perp c_I n^2 \int_{T_s}^{T_c} L_{rad}(T) dT \quad (3)$$

where $T_{c,s} = T(x_{c,s})$, $q_c = q_x(x_c)$ is given by the heating power transported from the core to the edge region; $q_c = q_x(x_c) = \kappa_\perp T_s / \delta_s$ is prescribed as a boundary condition [41, 42], with the temperature e -folding length δ_s at the separatrix defined by the transport in the SOL with open field lines and being fixed in the present analysis. By assessing the term on the left-hand side (lhs), we adopt for q_x its value average in the

edge region, $(q_c + q_s)/2$. Furthermore, it is reasonable to assume that by the oscillations in question the strongest time variation in the temperature occurs close to the outer boundary and $\partial_t T_s$ makes the largest contribution to the integral on the lhs of Eq. (3). In average over the edge we assume $\partial_t T \approx \frac{\partial T_s}{2}$ and the lhs of Eq. (3) is estimated as $C \partial_t T_s$, with $C(T_s) \approx 1.5n(x_s - x_c)(q_c + q_s)$. Normally $T_c = T(x_c) \approx 300 - 400 \text{ eV} \gg T_2$ and the integral in the rhs is practically unaffected by the upper integration limit. Finally, from Eq. (3) one gets the following equation for $T_s(t)$:

$$dT_s/dt \approx P(T_s)/C(T_s) \quad (4)$$

In **Figure 19**, the rhs of Eq. (4) is displayed for $q_c = 80 \text{ kW m}^{-2}$, $\kappa_{\perp} = 8 \times 10^{19} \text{ m}^{-1} \text{ s}^{-1}$, $\delta_s = 0.02 \text{ m}$, $x_s - x_c = 0.2 \text{ m}$, $c_I = 0.01$, $n = 8 \times 10^{19} \text{ m}^{-3}$ and $n = 10^{20} \text{ m}^{-3}$, parameters typical for the conditions of experiments aimed on the investigation of the detachment process in LHD [20].

4.1.2 Time evolution at the plasma density above the critical one

According to **Figure 19**, if a critical plasma density of $9 \times 10^{19} \text{ m}^{-3}$ is exceeded, no stationary state can be sustained for the assumed impurity concentration $c_I = 0.01$. The latter, however, does not remain at the same level since the plasma detachment from divertor target plates leads to the vanishing of the impurity source due to physical and chemical sputtering of the plate material [7]. As a result, impurities diffuse out of the plasma core and their concentration decreases. The characteristic time for the impurity concentration decay is of $\tau_I \approx l_I^2/D_{\perp}$, where l_I is the characteristic penetration depth of the mostly radiating Li-like ions of carbon and D_{\perp} is the charged particle diffusivity. Impurity transport analysis [42] shows that if $l_I \approx 0.05 - 0.1 \text{ m}$ and for $D_{\perp} \approx 0.5 \text{ m}^2 \text{ s}^{-1}$, we get $\tau_I \approx 5 - 20 \text{ ms}$. In the simplest way, the time evolution of impurity concentration can be described by the equation:

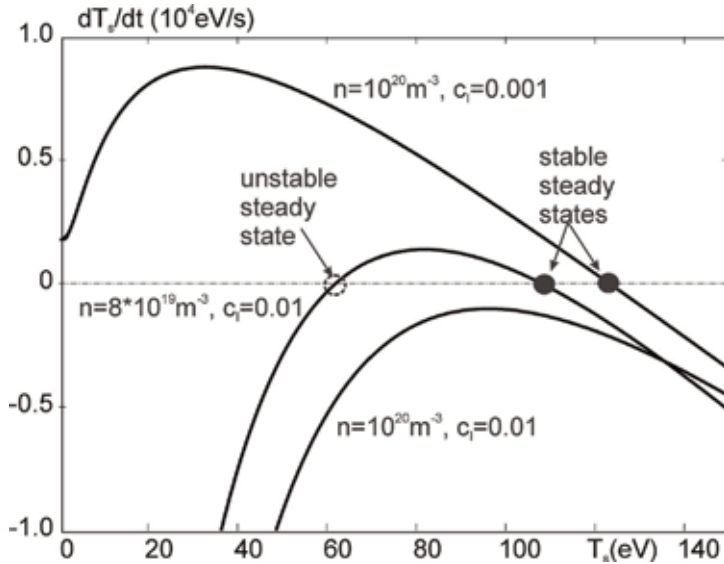


Figure 19. Dependence of time derivative of the plasma temperature at the outer boundary of the stochastic layer, x_s , the rhs of Eq. (3), on T_s for different plasma density and impurity concentration. Steady states, $dT_s/dt = 0$ with $\frac{\partial}{\partial T_s} \frac{dT_s}{dt} > 0$, $\frac{\partial}{\partial T_s} \frac{dT_s}{dt} < 0$ (black circles) are stable and that with $d^2T_s/dt^2 < 0$ (transparent circle) are unstable.

$$dc_I/dt = [c_I^0(T_s) - c_I]/\tau_I \quad (5)$$

For the stationary impurity concentration, we assume $c_I^0(T_s \geq T_s^*) = 10^{-2}$ and $c_I^0(T_s < T_s^*) = 10^{-3}$ with $T_s^* \approx 5$ eV. **Figure 20** demonstrates the time evolution of the impurity concentration c_I and of the radiation level q_{rad}/q_c , calculated for $n = 10^{20} \text{ m}^{-3}$ and $\tau_I = 15$ ms. Without knowing the exact temperature profile $T(x)$, needed to assess the flux density of radiation losses q_{rad} firmly, we estimated this by assuming a linear one $T(x) = [T_s(x - x_c) + T_c(x_s - x)]/(x_s - x_c)$.

One can see that the frequency of these oscillations is of 100 Hz, in agreement with observations.

By concluding this section, we discuss qualitatively possible causes for the difference in the behavior of the detached plasma in LHD without and with RMP, respectively, an unstoppable penetration of cold plasma into the core, leading to the radiation collapse, and the existence of the plasma density range where the radiation layer is stably confined at the plasma edge. As it has been demonstrated in [42], the mechanisms both of plasma heating and heat transfer through the plasma are of the importance for the discharge behavior by achieving the critical density. In ohmically heated discharges in the tokamak TEXTOR, where the plasma current was maintained at a preprogrammed level, a radial detachment was stopped by the increase in the density of the heat flux from the hot plasma core due to decreasing minor radius of the current carrying plasma column. If, however, the main heating is predominantly supplied from other sources such as NBI, this stabilization mechanism is ineffective and, as calculations in [42] have shown, a radiation collapse occurs, similar as this happens in LHD without RMP.

What occurs as a detachment set is determined by the competition between the decay of the impurity concentration in the plasma, characterized by the time τ_I , and time for the cooling front spreading into the plasma core. As it has been discussed in the first part, in addition to the magnetic island with strongly increased transport, RMP induce a region deeper into the plasma core. With the experimentally measured T_e profiles, one can assess that with the RMP, the heat conduction in this region is reduced by a factor of 10 and the heat conductivity $\chi_{\perp} = \kappa_{\perp}/n$ is of $1 \text{ m}^2 \text{ s}^{-1}$. For the penetration of the cooling front through this region, with a width Δ of 0.15 m, a time of $\Delta^2/\chi_{\perp} \approx 20$ ms is needed. This is at the upper limit of the impurity decay time, and

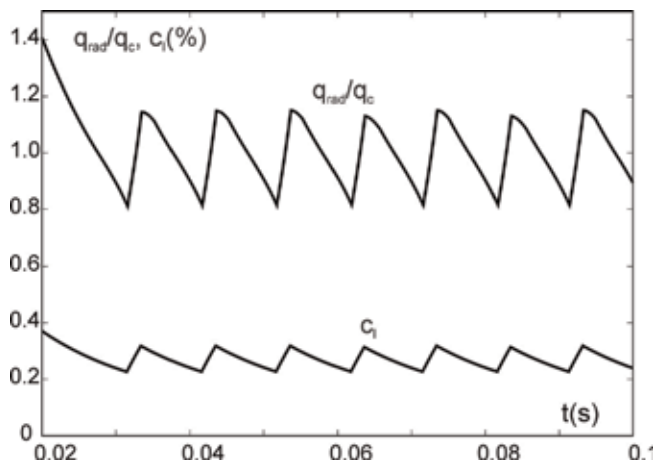


Figure 20. The time evolution of the impurity radiation level q_{rad}/q_c and concentration, calculated by integrating Eqs. (4) and (5) for $n = 10^{20} \text{ m}^{-3}$ and $\tau_I = 15$ ms.

therefore, the cooling wave most probably fades out. This mechanism is to some extent similar to that of the excitation of self-sustained oscillations in a plasma-wall system with strongly inhomogeneous diffusivity of charged particles [40].

4.2 Model for self-sustained oscillations by detachment in the regime of strong recycling on divertor targets

4.2.1 Stationary states in the recycling zone near the target

In a stationary state, the plasma parameters, such as electron density n and temperature T , near the divertor target are governed by the particle and heat balances in the recycling zone (RZ), see **Figure 21**. On the one hand, the heat flux transported to the RZ by plasma heat conduction and convection is dissipated by the energy loss (i) with the plasma outflow to the target, (ii) by the ionization and excitation of recycling neutrals, and transfer of the thermal energy of neutrals, escaping from the plasma layer, $|x| \leq \delta_p/2$, to gas particles:

$$q_r \delta_p = \gamma T_t \Gamma_t \delta_p + E_{ion} (\Gamma_t \delta_p - J_a) + 1.5 J_a T_r \quad (6)$$

Here, q_r is the heat influx into RZ projected onto the normal to the target, γ is the heat transmission factor, $\Gamma_t = n_t c_s \sin \psi$ is the same projection for the plasma particle outflow to the target, $c_s = \sqrt{2T_t/m_i}$ is the ion sound velocity, n_t , T_t are the plasma density and temperature near the target, ψ is the inclination angle of the magnetic field to the target, E_{ion} is the energy spent on the ionization of an atom, and J_a is the density of the atom outflow from the plasma layer.

In addition to Eq. (6), the particle balance in the RZ has to be fulfilled in a stationary state:

$$\Gamma_r \delta_p = J_a \quad (7)$$

where Γ_r is normal to the target projection of the influx into the RZ of charged particles from the main SOL. To assess J_a , one has to consider behavior of atoms, recycling from the target. In the plasma layer, $|x| \leq \delta_p/2$, these are ionized by

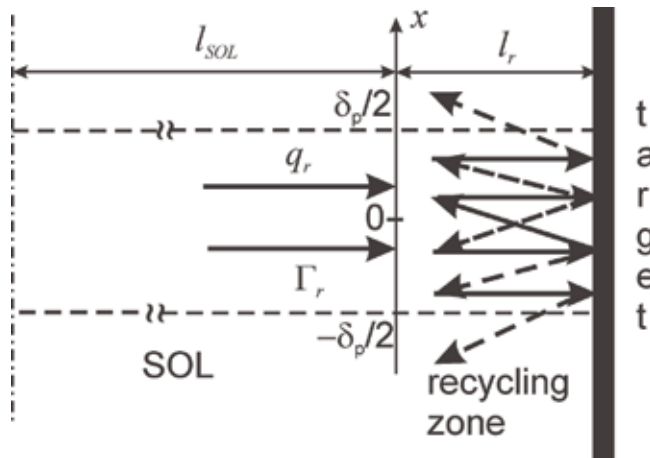


Figure 21. A schematic view of the charged and neutral particle flows in the recycling zone (RZ) in vicinity of a divertor target plate; q_r and Γ_r are the projections normal to the target of the densities of heat and charged particle influxes into the RZ from the main SOL.

electrons and charge-exchange (cx) with ions. The cx rate coefficient k_{cx} is noticeably larger than that for ionization, k_{ion} . Thus, during the lifetime, recycling atoms many times chaotically changes the velocity direction; i.e., their motion near the target is like Brownian one. Quantitatively, it is described by the diffusivity:

$$D_a = V_i \lambda_a = V_i^2 / [(k_{cx} + k_{ion}) n_r] \quad (8)$$

where $V_i = \sqrt{T_r / m_i}$ is the ion thermal velocity, which atoms acquire after a cx collision, λ_a is the mean free path length of atoms, and n_r, T_r are the characteristic plasma density and temperature in the RZ, which we have to define.

The width l_r of the recycling zone, **Figure 21**, is defined roughly as a distance from the target where the atom density $n_a(x, l)$ decays to a low enough level, e.g., by a factor of 10. By integrating over $0 \leq l \leq l_r$, the continuity equation is reduced to the following one for the variable $N_a(x) = \int_0^{l_r} n_a(x, l) dl$:

$$-D_a d^2 N_a / dx^2 = \Gamma_t - k_{ion} n_r N_a \quad (9)$$

The boundary conditions presume that atoms escape out of the plasma layer with their thermal velocity. With constant D_a and k_{ion} , corresponding to n_r, T_r , one finds an analytical solution to the equation above and gets:

$$J_a = \left[N_a \left(\frac{\delta_p}{2} \right) + N_a \left(-\frac{\delta_p}{2} \right) \right] V_i = \frac{\delta_p \Gamma_t}{\chi_{ion} + \chi_{dif} / \tanh \chi_{dif}} \quad (10)$$

with $\chi_{ion} = \delta_p k_{ion} n_r / (2V_i)$, $\chi_{dif} = \chi_{ion} \sqrt{1 + k_{cx} / k_{ion}}$.

For fixed q_r and Γ_r , Eqs. (6), (7), and relation (10) allow to determine the plasma parameters in the RZ, by taking into account that $n_r \approx n_t$, $T_r \approx T_t$. For $q_r = 5 \text{ kW/cm}^2$, $\delta_p = 5 \text{ cm}$ and $\psi = \pi/2$, **Figure 22** shows n_r, T_r calculated as functions of Γ_r .

4.2.2 The plasma particle influx into RZ and stability analysis of stationary states

The density of the charged particle influx into the RZ, Γ_r , is defined by the transfer of plasma particles and momentum along the magnetic field in the main part of the SOL. In a zero-dimensional approximation, these are as follows:

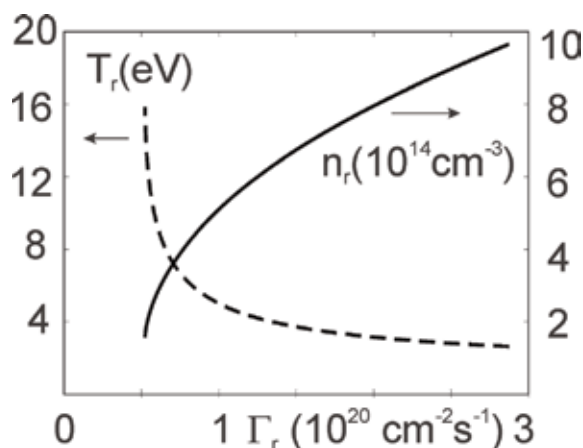


Figure 22. The Γ_r dependence of the plasma parameters in the recycling zone calculated for $\psi = \pi/2$, $q_r = 5 \text{ kW/cm}^2$, and $\delta_p = 5 \text{ cm}$.

$$\frac{dn_{SOL}}{dt} = S_{\perp} - \frac{\Gamma_r}{l_{SOL}}, \quad \frac{d\Gamma_r}{dt} = \frac{2n_{SOL}T_{SOL} - M_r}{m_i l_{SOL}} \quad (11)$$

where n_{SOL} and T_{SOL} are the characteristic plasma density in the main SOL, far from the target, and S_{\perp} is the plasma source density due to losses from the confined plasma through the separatrix. The SOL extension in the poloidal direction, l_{SOL} , is much longer than that of RZ, l_r , and therefore, a characteristic time for Γ_r change is much larger than that for n_r , T_r . Thus, the latter are always governed by quasi-stationary Eqs. (6) and (7). The total momentum at the entrance of the RZ is,

$$M_r = 2n_r T_r + \frac{m_i}{n_r} \left(\frac{\Gamma_r}{\sin \psi} \right)^2 \quad (12)$$

In a stationary state, $dn_{SOL}/dt = d\Gamma_r/dt = 0$ and $\Gamma_r^{st} = S_{\perp} l_{SOL}$, $n_{SOL}^{st} = M_r(\Gamma_r^{st})/(2T_{SOL})$.

To analyze the stability of stationary states, we assume as usually that there is a spontaneous small deviation from such a state, i.e., $\Gamma_r(t) = \Gamma_r^{st} + \delta\Gamma_r \exp(\gamma t)$ and $n_{SOL}(t) = n_{SOL}^{st} + \delta n_{SOL} \exp(\gamma t)$. Due to strong dependence of the parallel heat conduction on the temperature, $\kappa_{\parallel} \sim T^{2.5}$, T_{SOL} is considered as unperturbed. By substituting these forms of $\Gamma_r(t)$, $n_{SOL}(t)$ into Eq. (11) and requiring that the resulting system of linear equations for $\delta\Gamma_r$ and δn_{SOL} has a nontrivial solution, one gets a quadratic algebraic equation for the growth rate γ with the solutions:

$$\gamma = -\omega_r/2 \pm \sqrt{\omega_r^2/4 - \omega_s^2} \quad (13)$$

where $\omega_r = \frac{\partial M_r / \partial \Gamma_r}{m_i l_{SOL}}$ and $\omega_s = \frac{\sqrt{2T_{SOL}/m_i}}{l_{SOL}}$. Usually, $|\omega_r| \ll \omega_s$, i.e., the second term in γ is imaginary and defines the frequency for small oscillations. Thus, $\text{Re}\gamma > 0$ for $\omega_r \sim \partial M_r / \partial \Gamma_r < 0$, and the corresponding states with the negative slope of the $M_r(\Gamma_r)$ dependence are unstable. **Figure 23** shows this dependence for the parameter magnitudes used to calculate the results presented in **Figure 22**. In addition, we display by the dashed curve the $M_r(\Gamma_r)$ dependence obtained, by taking into account the energy losses on ionization and excitation of carbon impurity eroded from the target plate by physical and chemical sputtering, see [7]. The vertical lines correspond to Γ_r^{st} for different S_{\perp} . For the larger one, the stationary state is unstable.

It is of interest to consider how $M_r(\Gamma_r)$ dependence changes with the magnitude of q_r and **Figure 24** demonstrates this. For low enough q_r , the losses on ionization of all recycling neutrals, the second term on the right-hand side of Eq. (6), exceed significantly the heat influx into the RZ, and atoms freely escape into the gas, i.e.,

$$\Gamma_r \approx n_t c_s \sin \psi \quad \text{and} \quad M_r \approx 4n_t T_t \approx \frac{4\sqrt{q_r \Gamma_r m_i}}{\sqrt{2\gamma + 3 \sin \psi}}.$$

For large enough q_r , practically all recycling atoms are ionized in the plasma layer and Eq. (6) provides $n_r \approx q_r / [c_s \sin \psi (E_{ion} + \gamma T_r)]$ and

$$M_r \approx 2n_r T_r \approx \frac{q_r \sqrt{2\Gamma_r m_i}}{\sin \psi (E_{ion} + \gamma T_r)}.$$

Thus, as a function of T_r , M_r has a maximum at $T_r = E_{ion}/\gamma$. Because of the unique relation between Γ_r and T_r , a maximum exists also for the $M_r(\Gamma_r)$ dependence. For a stationary state with $\partial M_r / \partial \Gamma_r < 0$, the instability would lead to an enduring increase of Γ_r and n_r and decrease of T_r . A new steady state can be achieved due to mechanisms, which are not taken into account in the present model, e.g., recombination of charged particles. In [38], the maximum in $M_r(T_r)$ has been interpreted as a density limit in the main SOL. Indeed, since in the case of interest $M_r \approx 2n_{SOL} T_{SOL}$ and T_{SOL} is changing very weakly, n_{SOL} cannot exceed $M_r^{\max} / (2T_{SOL})$.

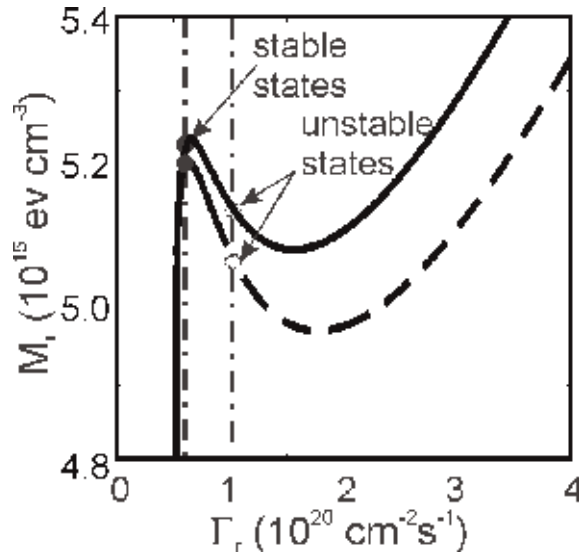


Figure 23. M_r versus Γ_r calculated for $q_r = 5 \text{ kW/cm}^2$, $\delta_p = 5 \text{ cm}$ and $\psi = \pi/2$, without (solid curve) and with (dashed curve) impact of C impurity eroded from the target. Vertical lines correspond with stationary Γ_r^{st} values for different S_{\perp} . The states with larger Γ_r^{st} are unstable.

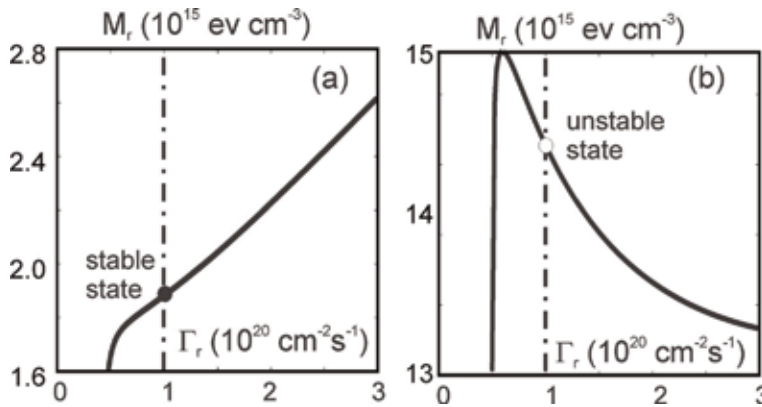


Figure 24. $M_r(\Gamma_r)$ computed for $q_r = 1.5 \text{ kW/cm}^2$ (a) and 15 kW/cm^2 (b). For the same, $\Gamma_r^{st} = 10^{22} \text{ cm}^{-2} \text{ s}^{-1}$ stationary states can be both stable (a) and unstable (b).

4.2.3 Limit cycle nonlinear oscillations

The case of the intermediate $q_r = 5 \text{ kW/cm}^2$ presented in **Figure 23** is considered qualitatively. The plasma in the RZ, being initially in the unstable stationary state with $\Gamma_r^{st} = 10^{20} \text{ cm}^{-2} \text{ s}^{-1}$, will deviate from this along the $M_r(\Gamma_r)$ curve to one of its optima, e.g., to the maximum point A, **Figure 25**. Here, Γ_r is smaller than its stationary level and $dn_{SOL}/dt > 0$, see Eq. (11). The increase in n_{SOL} leads to $d\Gamma_r/dt > 0$, and Γ_r also increases till the trajectory in the (Γ_r, M_r) phase plane comes to the point B at the stable branch on the $M_r(\Gamma_r)$ curve. Here, both dn_{SOL}/dt and $d\Gamma_r/dt$ are negative and Γ_r, M_r decrease to the minimum point C. Since in this point $d\Gamma_r/dt$ is still negative, a development till the point D on the left stable branch of the $M_r(\Gamma_r)$ curve takes place. Here, $d\Gamma_r/dt > 0$ and Γ_r, M_r increase till the point A.

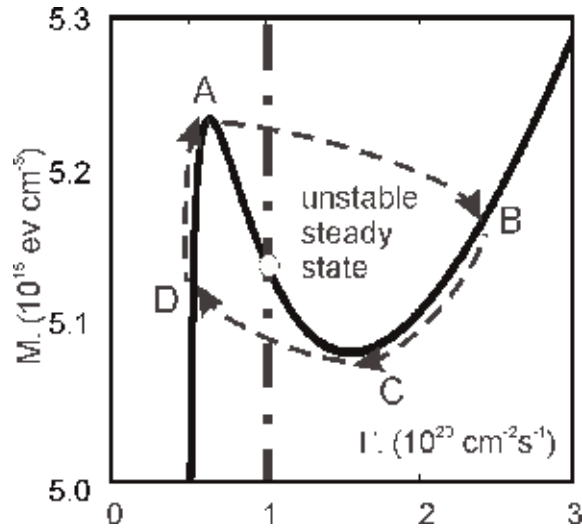


Figure 25. Schematic view of the limit cycle oscillations around an unstable steady state at $q_r = 1.5 \text{ kW/cm}^2$ and $\Gamma_r^{st} = 10^{22} \text{ cm}^{-2} \text{ s}^{-1}$.

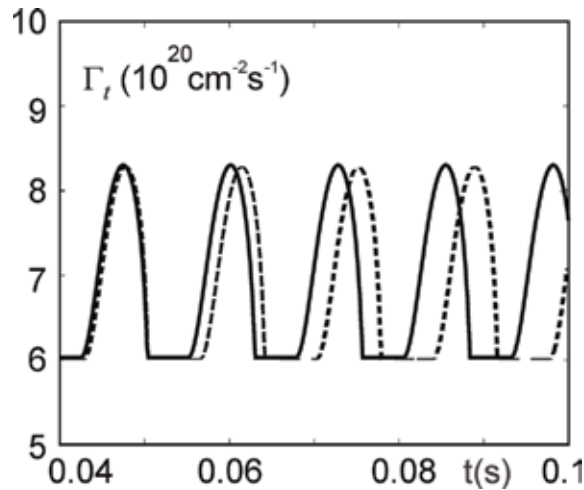


Figure 26. Time evolution of the plasma flux density onto the target, Γ_t , obtained by numerical integration of Eq. (11) for the unstable steady state at $q_r = 1.5 \text{ kW/cm}^2$ and $\Gamma_r^{st} = 10^{22} \text{ cm}^{-2} \text{ s}^{-1}$ without (solid curve) and with (dashed curve) impact of C impurity eroded from the target.

Thus, nonlinear oscillations around the unstable stationary point arise. In **Figure 26**, the time evolution for the flux density onto the target, $\Gamma_t(t)$, for the set of input parameters as for **Figure 25** is presented.

5. Conclusions

Plasma detachment from divertor targets is an important and very interesting phenomenon in fusion devices including helical systems and tokamaks. On the one hand, it can lead to the deterioration of the plasma performance and even to the total collapse of the discharge. On the other hand, detachment, if it is controlled and

stable can be useful for the reduction of the heat power losses to the target plates and even may lead to peaking of the pressure profiles in the plasma core that manifests in a confinement improvement. Resonant magnetic perturbations providing a broad enough magnetic island close to the separatrix has proven to be an effective method to control detachment in LHD.

Often at the onset of the detachment, large nonlinear oscillations of relatively low frequency can be observed in different plasma parameters, such as radiated power and ion saturation current to the target plates. Two models of such self-sustained oscillations are proposed. The first one is relevant to the radial detachment in LHD with divertor legs of low plasma density and transparent for neutrals. The second model offers an explanation for phenomena in tokamaks observed at the transition from strong recycling to plasma detachment at divertor targets.

Acknowledgements

The authors are grateful for the fruitful discussions with Prof. S. Masuzaki, Prof. S. Morita, Dr Y. Narushima, Prof. N. Ohno, Prof. B.J. Peterson, Prof. R. Sakamoto, Dr R. Seki, Dr H. Tanaka, Dr T. Tokuzawa, Prof. K.Y. Watanabe, Prof. H. Yamada, Dr I. Yamada, Prof. M. Yokoyama, Dr. J.W. Ahn, Dr Y. Feng, Prof. K. Ida, Prof. K. Itoh, Prof. S. Kajita, Dr G. Kawamura, Prof. T. Morisaki, Dr K. Mukai, Dr K. Nagaoka, Prof. M. Osakabe, Dr H. Takahashi, and Prof. K. Tanaka. The authors also thank the LHD experimental group for the excellent operation of LHD. The work has been financially supported by JSPS KAKENHI with grant numbers JP16H04622 and JP19H01878 and NIFS budget code ULPP026.

Author details

Masahiro Kobayashi^{1,2*} and Mikhail Tokar^{1,3}

1 National Institute for Fusion Science, National Institutes of Natural Sciences, Toki, Japan

2 Department of Fusion Science, SOKENDAI, Toki, Japan

3 Institute for Energy and Climate Research—Plasma Physics, Jülich Research Centre, Germany

*Address all correspondence to: kobayashi.masahiro@nifs.ac.jp

IntechOpen

© 2019 The Author(s). Licensee IntechOpen. This chapter is distributed under the terms of the Creative Commons Attribution License (<http://creativecommons.org/licenses/by/3.0>), which permits unrestricted use, distribution, and reproduction in any medium, provided the original work is properly cited. 

References

- [1] Pitts RA et al. Physics basis for the ITER tungsten divertor. *Nuclear Materials and Energy*
- [2] Asakura N et al. Studies of power exhaust and divertor design for a 1.5 GW-level fusion power DEMO. *Nuclear Fusion*. 2017;**57**:126050. DOI: 10.1088/1741-4326/aa867a
- [3] Takeiri Y et al. Realization of high T_i plasmas and confinement characteristics of ITB plasmas in the LHD deuterium experiments. *Nuclear Fusion*. 2018;**58**:106028. DOI: 10.1088/1741-4326/aad87e
- [4] Wolf RC et al. Major results from the first plasma campaign of the Wendelstein 7-X stellarator. *Nuclear Fusion*. 2017;**57**:102020. DOI: 10.1088/1741-4326/aa770d
- [5] Evans TE et al. 3D vacuum magnetic field modelling of the ITER ELM control coil during standard operating scenarios. *Nuclear Fusion*. 2013;**53**:093029. DOI: 10.1088/0029-5515/53/9/093029
- [6] Schmitz O et al. Three-dimensional modeling of plasma edge transport and divertor fluxes during application of resonant magnetic perturbations on ITER. *Nuclear Fusion*. 2016;**56**:066008. DOI: 10.1088/0029-5515/56/6/066008
- [7] Stangeby PC. *The Plasma Boundary of Magnetic Fusion Devices*. Bristol, Philadelphia: Institute of Physics Publishing; 2000
- [8] Shimomura Y et al. Characteristics of the divertor plasma in neutral-beam-heated ASDEX discharges. *Nuclear Fusion*. 1983;**23**:869. DOI: 10.1088/0029-5515/23/7/002
- [9] Masuzaki S et al. The divertor plasma characteristics in the large helical device. *Nuclear Fusion*. 2002;**42**:750. DOI: 10.1088/0029-5515/42/6/313
- [10] Feng Y et al. Physics of island divertors as highlighted by the example of W7-AS. *Nuclear Fusion*. 2006;**46**:807. DOI: 10.1088/0029-5515/46/8/006
- [11] Kobayashi M et al. Transport characteristics in the stochastic magnetic boundary of LHD: Magnetic field topology and its impact on divertor physics and impurity transport. *Fusion Science and Technology*. 2010;**58**:220. DOI: 10.13182/FST10-A10809
- [12] Kobayashi M et al. 3D effects of edge magnetic field configuration on divertor/scrape-off layer transport and optimization possibilities for a future reactor. *Nuclear Fusion*. 2015;**55**:104021. DOI: 10.1088/0029-5515/55/10/104021
- [13] Ezumi N et al. Experimental observation of plasma flow alternation in the LHD stochastic magnetic boundary. *Journal of Plasma and Fusion Research Series*. 2009;**8**:429
- [14] Feng Y et al. Comparative divertor-transport study for helical devices. *Nuclear Fusion*. 2009;**49**:095002. DOI: 10.1088/0029-5515/49/9/095002
- [15] Kobayashi T et al. Three dimensional distribution of impurity emission in the edge region of LHD obtained by single field-of-view tomography. *Nuclear Materials and Energy*. 2019;**19**:239. DOI: 10.1016/j.nme.2019.02.015
- [16] Zhang HM et al. Estimation of partial carbon radiation at each ionization stage of C₂₊ to C₅₊ ions in large helical device. *Plasma and Fusion Research*. 2016;**11**:2402019
- [17] Tanaka H et al. Toroidally symmetric/asymmetric effect on the divertor flux due to neon/nitrogen seeding in LHD. *Nuclear Materials and Energy*. 2017;**12**:241. DOI: 10.1016/j.nme.2016.12.020

- [18] Mukai K et al. Development of impurity seeding and radiation enhancement in the helical divertor of LHD. *Nuclear Fusion*. 2015;**55**:083016. DOI: 10.1088/0029-5515/55/8/083016
- [19] Kawamura G et al. Three-dimensional impurity transport modeling of neon-seeded and nitrogen-seeded LHD plasmas. *Plasma Physics and Controlled Fusion*. 2018;**60**:084005. DOI: 10.1088/1361-6587/aac9ea
- [20] Kobayashi M et al. Control of 3D edge radiation structure with resonant magnetic perturbation fields applied to the stochastic layer and stabilization of radiative divertor plasma in LHD. *Nuclear Fusion*. 2013;**53**:093032. DOI: 10.1088/0029-5515/53/9/093032
- [21] Pandya SN et al. Dynamics of three-dimensional radiative structures during RMP assisted detached plasmas on the large helical device and its comparison with EMC3-EIRENE modeling. *Nuclear Fusion*. 2016;**56**:046002. DOI: 10.1088/0029-5515/56/4/046002
- [22] Zhang HM et al. Vertical profiles and two-dimensional distributions of carbon line emissions from C^{2+} – C^{5+} ions in attached and RMP-assisted detached plasmas of large helical device. *Physics of Plasmas*. 2017;**24**:022510. DOI: 10.1063/1.4976989
- [23] Ohya N et al. The large helical device (LHD) helical divertor. *Nuclear Fusion*. 1994;**34**:387. DOI: 10.1088/0029-5515/34/3/i07
- [24] Kobayashi M et al. Core plasma confinement during detachment transition with RMP application in LHD. *Nuclear Materials and Energy*. 2018;**17**:137. DOI: 10.1016/j.nme.2018.10.003
- [25] Narushima Y et al. Magnetic diagnostics of magnetic island in LHD. *Plasma and Fusion Research*. 2007;**2**:S1094
- [26] Narushima Y et al. Behavior of plasma response field in detached plasma. *Plasma and Fusion Research*. 2013;**8**:1402058
- [27] Kobayashi M et al. Impact of resonant magnetic perturbation field on impurity radiation, divertor footprint, and core plasma transport in attached and detached plasmas in LHD. *Nuclear Fusion*. <https://doi.org/10.1088/1741-4326/ab26e6>
- [28] Sudo S et al. Scalings of energy confinement and density limit in stellarator/heliotron devices. *Nuclear Fusion*. 1990;**30**:11. DOI: 10.1088/0029-5515/30/1/002
- [29] Feng Y et al. Physics of the geometry-related detachment stability in W7-AS. *Nuclear Fusion*. 2005;**45**:89. DOI: 10.1088/0029-5515/45/2/003
- [30] Pedersen TS et al. First divertor physics studies in wendelstein 7-X. *Nuclear Fusion*
- [31] Masuzaki S et al. Effects of drifts on divertor plasma transport in LHD. *Nuclear Materials and Energy*. 2019;**18**:281. DOI: 10.1016/j.nme.2019.01.009
- [32] Kobayashi M et al. Detachment stabilization with $n/m = 1/1$ resonant magnetic perturbation field applied to the stochastic magnetic boundary of the large helical device. *Physics of Plasmas*. 2010;**17**:056111. DOI: 10.1063/1.3368681
- [33] Yokoyama M et al. Extended capability of the integrated transport analysis suite, TASK3D-a, for LHD experiment. *Nuclear Fusion*. 2017;**57**:126016. DOI: 10.1088/1741-4326/aa800a
- [34] Rechester AB, Rosenbluth MN. Electron heat transport in a tokamak with destroyed magnetic surfaces. *Physical Review Letters*. 1978;**40**:38. DOI: 10.1103/PhysRevLett.40.38

[35] Tokar MZ. On transport, in particular of impurities, in a stochastic magnetic field. *Physics of Plasmas*. 1999; **6**:2808. DOI: 10.1063/1.873238

[36] Prigogine I. *Introduction to Thermodynamics of Irreversible Processes*. 2nd ed. New York: Interscience; 1961

[37] Loarte A, Monk RD, Kukushkin AS, Righi E, Campbell DJ, Conway GD, et al. Self-sustained divertor plasma oscillations in the JET tokamak. *Physical Review Letters*. 1999;**83**:3657-3660

[38] Krasheninnikov SI, Kukushkin AS, Pistunovich VI, Pozharov VA. Self-sustained oscillations in the divertor plasma. *Nuclear Fusion*. 1987;**27**: 1805-1816

[39] Nedospasov AV, Tokar MZ, Vasin NL. Plasma recycling and MARFE phenomenon in a tokamak. *Contributions to Plasma Physics*. 1988; **28**:453-458

[40] Tokar MZ. Self-sustained oscillations in a plasma-wall system with strongly inhomogeneous diffusion of charged particles. *Physical Review Letters*. 2005;**95**:2650029. DOI: 10.1103/95.265002

[41] Tokar MZ. On threshold of radial detachment in tokamaks. *Physics of Plasmas*. 2000;**7**:2432-2438. DOI: 10.1063/1.874082

[42] Tokar MZ. Modelling of detachment in a limiter tokamak as a nonlinear phenomenon caused by impurity radiation. *Plasma Physics and Controlled Fusion*. 1994;**36**:1819-1843

Section 2

Modeling and Simulation Studies

Wave Spectra in Dusty Plasmas of Nuclear Fusion Devices

*Aamir Shahzad, Muhammad Asif Shakoori
and Mao-Gang He*

Abstract

Wave's spectra are investigated through an equilibrium molecular dynamic (EMD) simulation of three-dimensional (3D) strongly-coupled complex-dusty plasmas (SCCDPs). In this chapter, we have analyzed the correlation functions over a wide range of plasma parameters of Γ ($\equiv 1, 100$) and of κ ($\equiv 4.5, 5.5$) along with a higher wave's numbers of k ($\equiv 1, 4$). In EMD simulations, we have examined the propagation modes of wave in the longitudinal $C_L(k, t)$ and transverse $C_T(k, t)$ current direction at higher screening (κ). We have also analyzed the wave's spectra in different regimes of plasma states of SCCDPs. A new simulation shows that the longitudinal (C_L) and transverse (C_T) waves in SCCDPs are damped for low values of Γ . However, these damping affects decrease comparatively with an increasing Γ . Outcomes show that amplitude and frequency modes of the C_L and C_T depend on κ , Γ , k and probably on a number of particles (N). The results obtained from EMD are in reasonable agreement with earlier known theoretical and experimental data. It has been shown that the present EMD method is the best tool for computing C_L and C_T in the SCCDPs over a suitable range of plasma parameters.

Keywords: wave properties, plasma parameters, longitudinal current correlation, transverse current correlation, strongly coupled dusty plasmas, equilibrium molecular dynamic

1. Introduction

A partially or fully ionized gas containing neutral atoms, electrons, ions and with the addition of dust particles is known as dusty plasma (DPs). This additional component (dust particle) increases the complexity in the behavior of the system, and thus refers to this system as “dusty” or complex plasma [1]. Nowadays the term “complex plasma” is commonly used in literature to differentiate the dusty plasma. Due to embedded dust particles in the plasma, these dust particles create changes in the charge composition. The new physical processes were introduced in the system such as the recombination of plasma on the particle surface and effects associated with the degeneracy, fluctuations of particle charges which also change the energy and transport phenomena. That's the way the DPs became a new type of non-Hamiltonian systems. The presence of dust particles in the complex plasma is vital for the collective processes. These micro size dust particles create very low-frequency wave mode, which represents charge particle oscillations against the quasi-equilibrium background of ions and electrons. Generally, a dynamical time

scale related to the dust component is in the range of 10–100 Hz. Recently the dusty plasma becomes an interesting field for researchers, technologists and scientists [2, 3]. The initial challenge of fusion in nuclear devices is to confine ionized isotopes of hydrogen atom known as plasma, increase the plasma pressure to initiate and sustain the fusion reaction [4].

Dusty plasma is classified on the basis of density, temperature, potential, and thermal energy. For classification of dusty plasma first, we define Coulomb coupling parameters. Coulomb coupling defines as “the ratio of average potential energy to the average thermal energy of neighboring charged particles” and mathematically written as $\Gamma = Q^2 / 4\pi\epsilon_0 a_{ws} k_B T$ [5].

1.1 Weakly coupled dusty plasmas (WCDPs)

Weakly coupled dusty plasmas have higher average thermal energy than average potential energy due to neighboring charged particles. WCDPs have a high temperature, low density and value of Coulomb coupling parameter less than 1 ($\Gamma < 1$). WCDPs have no structural form due to high temperatures. The background of WCDPs is considered as ionized gases. The temperature of dust particles is much higher than those of ions, electrons, and the neutral population in the system. Due to this, difference in temperature values, DPs becomes a particular interest in the research field of science and technology [6].

1.2 Strongly coupled complex dusty plasmas (SCDPs)

In strongly coupled dusty plasma (SCDP), the average potential energy of neighboring charged particles is dominated on the average thermal energy of the same charged particles. This type of dusty plasma has high charged particles density and low temperature. The SCDPs speedily become emerging fields from last three decades. Due to the presence of dust particles in the atmosphere, the dusty plasma becomes a very significant research field of astrophysical plasma and also in nuclear fusion devices [7–9]. At higher density and low temperature, the SCDPs undergo in crystallization phase. In Coulomb coupling systems, the SCDPs change phase from liquid to crystal phase at specific values of the Coulomb coupling parameters. SCDPs known as a warm liquid at $\Gamma = 5$, liquefy at $\Gamma = 80$, it becomes cold liquid at $\Gamma = 100$, very cold ($\Gamma = 120$) and then liquid phase has a limitation at $\Gamma = 137$. The SCDP has a crystalline form at $\Gamma = 175$ value; it has very high density and very low temperature [10, 11]. SCDPs appear in many astrophysical objects such as neutron star crusts, white dwarf interiors, supernova cores, and giant planetary interiors. Charged particles in dusty plasma are also found in many physical systems such as condensed matter systems of liquid metals and molten salts, cryogenic traps, electrons trapped on the free surface of the helium. DPs play a very important progressing role in laboratory experiments. Nowadays, recently the dusty plasma plays a very significant role in the nuclear fusion devices for plasma confinement and to control the fusion reaction [12]. For basic experiments in the laboratory, the DPs shows very interesting phenomena such as melting and formation of crystals, collective modes excitation with reference to dust component. Nanostructure layered, and colloidal suspension of dusty plasma was also investigated in these set of references [13–15].

1.3 Properties of dust particles

Dust is present everywhere in the space and environment. Dust particles are much larger than electrons, ions, and neutral particles. Their sizes of dust particles

vary from hundreds of millimeters to 10 nm and the mass of dust particle is approximately 7.53×10^{-10} kg. Their dynamic behaviors are easily observed through a CCD camera because of temporal and spatial scale. These dust particles are mostly negatively charged; however, sometimes they have positive charged also, that depends upon the charging phenomena. The large shielding clouds are created for balance the ion thermal current and electron thermal current. Charging phenomena of dust particles are photoionization, electron bombardment, sputtering, etc. The amount of charge at dust particles depends upon shape and size. Most often, they have spherical shape; however, sometimes they are of the form of rod type and or irregular shape [13, 16]. Dust particles are exposed to ion and electron currents from discharge plasma that's why reached quickly in dynamical equilibrium. The electric charge on the dust particle depends upon their radius (size) and shape, and the charge amount is in the order of 10^3 – 10^4 electrons. Increasing the charge on the particles increases the electrostatic repulsion between them in a confined system and may lead to crystallization [17]. The dust particles are strongly coupled due to high electric charges and unable to move easily so that they look like a solid and liquid phase in the DPs. The phonon spectra in the DPs are easily calculated due to the thermal motion of dust particles [18]. The motion of dust particles generates the longitudinal and transverse waves in the dusty plasma. Due to the complex behavior of a dust particle in DPs, it becomes an independent field for researchers whose study dusty plasma with strong correlation. The charged dust particles are highly susceptible to the different forces in the plasma such as the electric field, neutral and ion drag and can serve as sensitive diagnostic tools [19].

1.4 The existence of DPs in nature and laboratory

DPs are found in the ionosphere, that's a lower part of the earth. Noctilucent clouds (NLs) are composed of ice and dust from manmade pollution and heavy clusters. In the space environment, the examples of dusty (complex) plasma are Jupiter rings, were first observed in 1779, comets, planetary rings and spokes, Saturn's rings and Neptune. The size of dust particles in Saturn ring varies from micron to sub-micron. The radial spokes also consist of micron and submicron sized dust charged particles that are electrostatically levitated. The presence of dust particles in the atmosphere at the altitudes in the range of 80 and 90 km was observed during polar summer mesopause [20]. The presence of dust particles was observed in the nuclear fusion devices, both Tokamaks and stellarators. Due to the presence of dust particles in these devices may disturb the performance and stop working on it. Nowadays, study of dust particles in fusion devices becomes very important. The charging mechanisms of dust particles in these devices are also investigated by Liu et al. [21]. It becomes very necessary for operational Tokamak or other fusion devices to study and found waves and transport properties of dusty plasma. Thermal conductivity, diffusion coefficient, shear viscosity in dusty plasma and charging mechanisms of dust particles in nuclear fusion devices are also needed to investigate [22]. The dust particles are also observed in radio frequency (RF) device and direct current (DC) glow discharge tube and Z-Pinch device etc. Under the laboratory condition, the plasma crystals are observed in different devices such as in RF, DC, thermal plasma, nuclear-induced dusty plasma over wide range of plasma parameters [23].

1.5 Nuclear fusion devices

Fusion energy is a source of energy for a future generation which is almost inexhaustible. Currently, it is an undefeatable challenge for engineering and

thermophysical researchers. The basic challenge to achieve the fusion energy is “to achieve a rate of heat emitted by fusion plasma that exceeds the rate of energy injected into the plasma”. The central expectations are focused on two fusion reactor devices, one is Tokamak and the other is stellarator. Today the whole world community is working for nuclear fusion device, which is known as Tokamak. Fusion energy is investigated and comes closest to the explosion. These devices consist of a ring-type magnetic field used to confine the plasma. Tokamak plasma is confined by an electric current flowing in plasma, and in the stellarators, a magnetic field of very complicated shape used to confine plasma stationary. The Tokamak work only in the pulsed mode without auxiliary facilities and stellarators is suitable for continuous operation. The most effective magnetic field configuration is toroidal in the shape of the doughnut. The Tokamaks, stellarators and the reversed field pinch (RFP) are commonly under developing fusion nuclear devices based on toroidal confinement configuration. The Z-pinch is also nuclear fusion device in which is a strong electrical current in plasma to generate X-rays. The magnetized target fusion, referred to as a MIF (magneto-inertial fusion) system, is also currently in progress. In these nuclear devices, a magnetic field is applied to confine the plasma with the help of electromagnetic or mechanical linear implosion. A compression heating is provided with laser hot dense magnetized plasma which is created in the plasma focus (PF) devices. The PF devices belong to the family of dynamic noncylindrical Z-pinch. If in this device deuterium is used as gases then DD fusion reaction takes place [24–28].

1.6 Dusty plasma in fusion devices

The working conditions of nuclear fusion devices are such that the fuel of these devices must be heated up to heat fuel in nuclear fusion devices heat in the range of 100×10^8 K temperature, at this temperature the fuel is in the plasma state. The temperature of the plasma is very high, and materials are vaporized that contact with it, that’s why plasma must be confined kept in the magnetic fields. In the Tokamak reactor fuel is use in the range of grams (g), so it is a very safe device. The solid impurities are known as “dust” were also found and investigate Scrape-Off Layer transport that is a key element of edge physics research program. For safety precautions against the dust particles, it is very significant for engineers to predict where the quantity of dust particles increases. To resolve the dust transport problem in fusion devices it is necessary for physicists to develop a fully accurate dust transport code (DTC) [29]. It is also required to calculate the plasma parameters from geometrical relations and engineering constraints of nuclear fusion Tokamak device. Plasma density (n), pressure (p), temperature (T), energy confinement time, β (normalized plasma pressure) as a function of α (minor radius of plasma) are the basic main plasma parameters. In addition, some plasma parameters such as plasma current, bootstrap fraction and kink safety factor are required for a plasma physicist in order to understand Tokamak process. The reactor demands toroidal current I to achieving high energy confinement time (very large) for ignition [3, 27]. There are several techniques used for heating plasma in Tokamak. The most common technique use to heat plasma is Ohmic heating, neutral beam injection, RF heating. The fusion plasma has such as high temperature so that they emit little visible light [30, 31].

1.7 Waves spectra in dusty plasma

To understand dynamical information and basic properties of gas, liquids, and solids, it is compulsory to study the basic two phenomena such as phase transition

and waves [32]. Dust particles in SCDPs support longitudinal (compressional) waves, also known as dust acoustic waves (DAWs) and transverse waves (shear) [13]. The propagations of longitudinal modes are faster than the transverse mode in the crystalline phase of dusty plasma. The WCDPs does not sustain the transverse wave and only sustain longitudinal waves. The compressional electrostatic waves and DAWs have low-frequency modes due to a larger mass of dust particles. In order to study the thermal motion of dust particles through MD simulation and it was found that cut off wave number is calculated for transverse mode near the solidification phase of dusty plasma [33]. The generalized hydrodynamics (GHD) model of the equation is predicted by the existence of transverse wave mode in the liquid and strong coupling regimes and dispersion properties of longitudinal modes [19]. Investigation of dusty longitudinal waves (DLWs—dust lattice waves) in two-dimensional bi-crystal in an arbitrary direction and it was found that hybrid modes have both components along with transverse and longitudinal directions. The hybrid modes become purely transverse to longitudinal waves for the angle of propagation is 0 or $\pi/2$ [34]. Background of the colloidal suspension liquid exerts large friction on the motion of charged particles than the background of dusty plasma gases. Due to low friction between charged particles in the gas phase of dusty plasma waves damped slowly. The complex (dusty) plasma the current correlation functions of complex (dusty) plasma are classified into the longitudinal current and transverse current, also known as longitudinal and transverse (shear) wave's mode. In the classical fluids, when k approaches zero then longitudinal modes known as acoustic modes. Strongly coupled plasma in the liquid phase supports shear maintained transverse mode. In SCDPs, when k approaches zero then transverse modes are also considered approach as acoustic modes [35] (**Figure 1**).

The uniform liquid phase does not support transverse modes of waves. The reason for this is to ignore the migration of diffusion damping. For isotropy liquid, the transverse mode approaches the same Einstein frequency ω_E as a longitudinal mode, when the wavenumber k approaches to infinite. The current correlation functions of DPs are studied theoretically, numerically and experimentally.

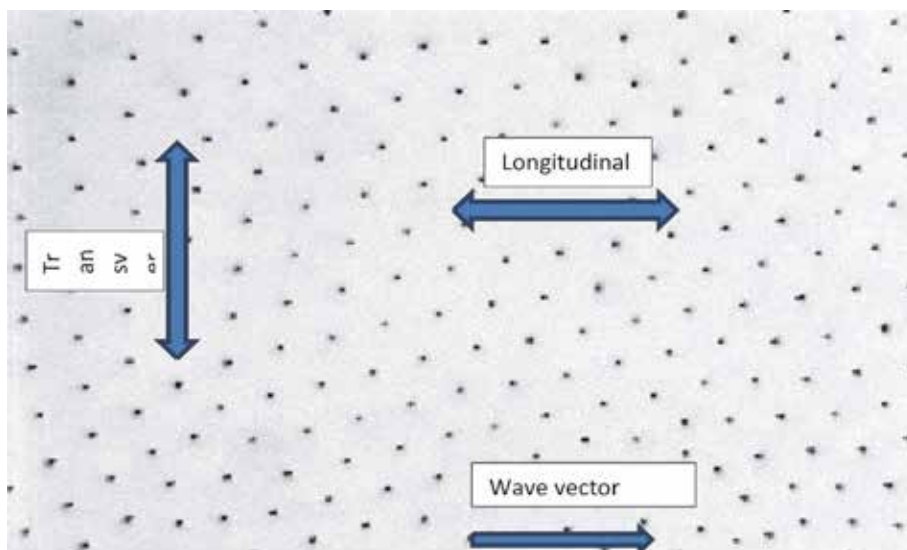


Figure 1. Directions of longitudinal and transverse waves in DPs relative to the direction of wave numbers vectors. The direction of the wave vector shows that direction of $C_L(k, t)$ is along the wave vector and direction of $C_T(k, t)$ is perpendicular to the wave vector (k) [36].

The results are in good agreement with the theoretical prediction, in support of simulation measurements and also verified by experiments [14, 16, 24].

1.8 MD simulation and types

An MD simulation is a tool that studies the microscopic model in a macroscopic system, and this model is quantified in terms of intermolecular interaction and the molecular structure. The results are obtained with accuracy through different simulation techniques (algorithm) and compared with theoretical and experimental results. Simulations are also used to study the wave properties of complex models at the microscopic level which cannot be investigated by experiments [37]. There are several computational techniques that have advantages and also disadvantages with their respective fields. Monte Carlo (MC) and molecular dynamics (MD) simulations are influential tools for the study of transport properties of dusty plasma. Transport properties can also be calculated by Langevin dynamics (LD), MC, path integral MC (PIMC) and MD methods. The disadvantage of the MC technique is that it cannot evaluate the transport properties of dynamical systems and cannot solve and apply the equations of motion [38].

2. Mathematical model and numerical method

In this chapter the EMD Simulations are performed for a selected system, having the number of particle $N = 500$ with apply periodic boundary condition (PBCs) on the cubic box in three dimensions coordinates directions. These particles are placed in a cube volume V and interact with each other by pairwise Yukawa potential is given:

$$\phi(|\mathbf{r}|) = \frac{Q^2}{4\pi\epsilon_0} \frac{e^{-|\mathbf{r}|/\lambda_D}}{|\mathbf{r}|}, \quad (1)$$

Q is the charge, on dust particles, ϵ_0 is permittivity of free space, λ_D is the Debye length which accounts for the screening of the interaction by other plasma species. The dimensionless plasma parameters have fully characterized the system under study. One is Coulomb coupling parameter and defines as $\Gamma = Q^2/4\pi\epsilon_0 a_{ws} k_B T$ (already defined in Section 1.1), where a is the Wigner-Seitz radius and is define as $a_{ws} = (3/4n\pi)^{1/3}$ with n is the dust particle density, T is the temperature of the system and k_B is Boltzmann constant. The screening parameter is and defines as $\kappa \equiv a_{ws}/\lambda_D$. In an EMD technique, Newton's motion equation is, $m(d^2r/dt^2) = F_i = \sum_j F_{ij}$, integrated numerically for N Yukawa particles with mass m positioned at r_i , velocity v_i and acceleration a_i in the volume (V) of simulation box of particle i ($i = 1, 2, 3 \dots N$) is exerted a force on other particle j and it is given as $F_i = \sum_j F_{ij}$ and $i \neq j$. The EMD is performed in the microcanonical ensemble (NVT) for constant volume and temperature [39]. In this chapter, the EMD has been used to investigate the time-dependent current correlation functions [$C_L(k, t)$ and $C_T(k, t)$]. The dimension of the simulation box is L_x, L_y, L_z . The periodic boundary condition is used to minimize the surface size effect and applied to the simulation box. The main calculation is performed for $N = 500$ particles at $\kappa = 4.5$ and 5.5 , plasma coupling parameters Γ (temperature of the Yukawa system) varies from 1 to 100 and wavenumbers $k = 0, 1, 2$, and 3 . The simulation time step is taken as $\Delta t = 0.001$ to allow computing the important data for sufficient 425,000 simulation run. EMD method is reported of the current correlation of SCDPs over sufficient

domain of plasma parameters of Debye screening ($4.4 \leq \kappa \leq 5.5$) and Coulomb coupling ($1 \leq \Gamma \leq 100$).

2.1 Current correlation functions

The SCDPs support both longitudinal and transverse waves. The experimental importance of time-dependent correlation function is that the spectroscopic technique an example of this technique is neutron scattering. Investigate microscopic dynamical quantities through the MD approach and then comparison by Fourier analysis of the simulation result. The local density gives information about the atom's distribution. There is also possible to analyze the motion of atoms. The Fourier component of Particle current or momentum current for a single atomic particle in MD unit is given as.

$$\pi(\mathbf{r}, t) = \sum_j v_j \delta(\mathbf{r} - \mathbf{r}_j(t)) \quad (2)$$

where v_j and r_j are the velocity and position of a j th particle, by using the Fourier transformation of particle current becomes as for a given wavenumber vector (\mathbf{k}).

$$\pi(\mathbf{k}, t) = \sum_j v_j e^{-i\mathbf{k} \cdot \mathbf{r}_j(t)} \quad (3)$$

The correlation function of the current vector component is defined as

$$C_{\alpha\beta}(\mathbf{k}, t) = \frac{k^2}{N_m} (\pi_\alpha(\mathbf{k}, t) \pi_\beta(-\mathbf{k}, 0)) \quad (4)$$

For the isotropic fluid under consideration of symmetry above equation can be expressed in term of longitudinal current correlation and transverse current correlation in the relative direction of \mathbf{k} , where \mathbf{k} is the wave vector and equal to multiple of integers $k = 2\pi/L$ and L is the size of the simulation box. Wave vector \mathbf{k} becomes equal to $\mathbf{k} = 2\pi/L (k_0, k_1, k_2, k_3)$, $k_j \in \mathbb{Z}$, $j = 0, 1, 2, 3$; L is the length of simulation box and $V = L^3$.

$$k = |\mathbf{k}| = \frac{2\pi}{L} |(x, y, z)| \quad (5)$$

Here x , y , and z are integers.

$$C_{\alpha\beta}(\mathbf{k}, t) = \frac{k_\alpha k_\beta}{k^2} C_L(\mathbf{k}, t) + \left(\delta_{\alpha\beta} - \frac{k_\alpha k_\beta}{k^2} \right) C_T(\mathbf{k}, t) \quad (6)$$

By putting $\mathbf{k} = k \mathbf{z}$ the time-dependent longitudinal current correlation becomes as.

$$C_L(\mathbf{k}, t) = \frac{k^2}{N_m} \left\langle \sum_i v_i e^{-i\mathbf{k} \cdot \mathbf{z}_i(t)} (\mathbf{k}, t) \sum_j v_j e^{-i\mathbf{k} \cdot \mathbf{z}_j} (\mathbf{k}, t) \right\rangle \quad (7)$$

Where N_m represents the number of particles, v_i and v_j are the velocity of the i th and j th particles, $\langle \dots \rangle$ gives the statistical average of particle current. Longitudinal current correlation function explains the direction of the waves along the wave vector (wavenumber) and a transverse direction perpendicular to \mathbf{k} .

$$C_T(k, t) = \frac{k^2}{2N_m} \langle \pi_x(k, t)\pi_x(-k, 0) + \pi_y(k, t)\pi_y(-k, t) \rangle \quad (8)$$

The longitudinal current correlation also related to the dynamical structure factor.

$$S(k, \omega) = \frac{1}{\omega^2} C_L(k, \omega) \quad (9)$$

In Eq. (9), the dynamical structure factor and longitudinal current correlation contain the same physical information of the systems. Transverse current and longitudinal current also explain the wave spectra in 3D SCDPs. In our EMD simulation model, the current correlation function is the only function of wavenumber and time (k, t). Through this mathematical model of current correlation, we checked out variation in frequency and peak amplitude of transverse and longitudinal waves in SCDPs for at Γ, κ, N , and k [14, 19, 32, 35].

3. Results and discussions

In this section, we describe the consequences of extensive MD simulations methodology work, carried out to explore the current correlation functions (compressional and share waves) of 3D Yukawa liquid via the EMD simulation technique. $C_L(k, t)$ (Eq. 7) and $C_T(k, t)$ (Eq. 8) is simulated at an extensive combinational range of parameters (Γ, κ, N and k). The $C_L(k, t)$ and $C_T(k, t)$ which are normalized by plasma frequency (ω_p) has been extensively used for prior studies of SCDPs but while here we are investigating its correspondence with time (t). The information waves spectra for nuclear fusion device conditions is generated from simulation goes, that prediction which is true for frequency spectra, current correlation function [$C_L(k, t), C_T(k, t)$] simulation are executed for higher screening strength of spherical charged dust particles ($\kappa = 4.5$ and 5.5) and Coulomb coupling parameters (inverse of plasma temperature) parallel closely same experimental plasma state (κ, Γ). This was executed to facilitate comparison with presented simulation results and available data of recent and earlier.

In this section, we present our EMD simulation results and their discussion of wave spectra from the current correlation function in the longitudinal and transverse wave's modes. The specific attention in this chapter is given to $C_L(k, t)$ and $C_T(k, t)$ for a different combination of plasma parameters which are investigate the behavior of transverse and longitudinal waves in 3D SCDPs. Explanation qualitatively features of the longitudinal (compressional or sound) waves in 3D complex (dusty) plasma shown in **Figures 2** and **3**. Here our EMD outcomes we compute the $C_L(k, t)$ for $\kappa = 4.5$ and 5.5 for a number of particles ($N = 500$) and in the direction of wave vector numbers ($k = 0, 1, 2$ and 3). We determined properties of longitudinal waves in SCDPs at a different combination of plasma parameters (κ, Γ), the results have plotted the magnitude of $C_L(k, t)$ against simulation time (t). In our EMD simulations result, the effect about plasma temperature is observed on the magnitude, wavelength, frequency, and damping phenomena of waves in SCDPs. **Figure 2** consists four panels which covering from non-ideal to the liquid and then liquefy state of dusty plasma. The panel (a) of both **Figures 2** and **3** represent the results of longitudinal wave spectra in the non-ideal state of dusty plasma at $\kappa = 4.5, 5.5$ respectively. It is observed from first panel of these two figures that collective modes of wave spectra are highly damped due to high temperature of dust particles confirmed good agreement with earlier published worked by Nunomura due to

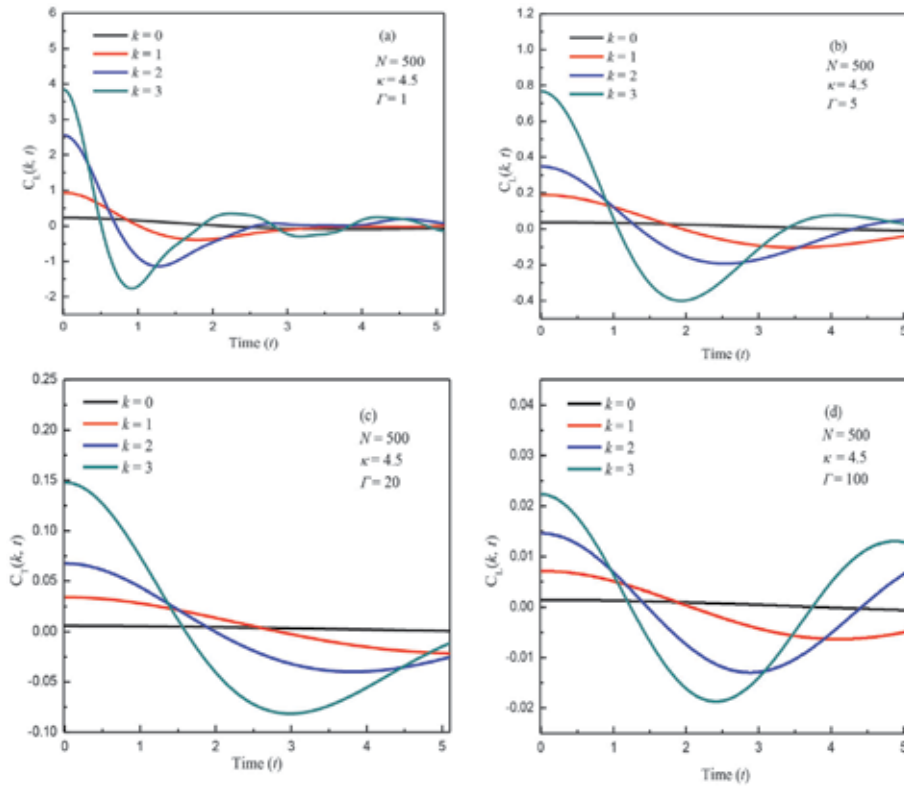


Figure 2. EMD simulations results of wave spectra of the longitudinal mode against the simulations time (t) for $\kappa = 4.5$ covering from non-ideal to liquid states ((a) $\Gamma = 1$, (b) $\Gamma = 5$, (c) $\Gamma = 20$ (d) $\Gamma = 100$) of 3D SCDPs and $N = 500$ for higher wave number ($k = 0, 1, 2$ and 3).

collisions between particles [30] and Shahzad et al., for low screening strength [2]. The modes of these waves in amplitudes of longitudinal waves increased at higher wavenumber ($k = 3$) and also at lower wavenumber has low peak amplitude mode clearly seems from results plotted in **Figures 2** and **3**. The damping of waves at a higher temperature would attribute this to viscous/collision and Landau damping. The effects of Γ on the propagation of waves in SCDPs are observed from four panels of **Figure 2**. The frequency modes are increases and amplitude decreases of $C_L(k, t)$ with increasing Γ . With increasing Γ the thermal effect decreases in the magnitude and the correlation effect clearly seems. **Figures 2** and **3** show the wave's spectra of longitudinal mode at different values of coupling which covering the non-ideal phase dusty plasma and also liquefy state. It is observed that the damping effect in wave's mode decrease with decreasing the plasma temperature. Here higher damping at $\Gamma = 1$ and at $\Gamma = 5$ comparatively low damped and then oscillate very at a low magnitude for $\Gamma = 5$. If we further increase the coupling values the damping decrease and longitudinal waves propagate in form of sinusoidal. At $\Gamma = 20$ and 100 waves in longitudinal modes properly propagate and with the passage of time, the magnitude of waves decreases we can observe **Figures 2** and **3** (d) at $\Gamma = 100$ in the liquid liquefy phase.

There is a slight effect of screening strength (κ) on longitudinal wave's mode in plasma with respect to damping and propagation phenomena. The frequency and amplitude of waves in SCDPs are high at lower values of κ when we increase screening strength at the same N , k and Γ amplitude and wavelength are gradual decreases with respect of κ . The magnitude of $C_L(k, t)$ 0.2332, 0.0379, 0.0057 and

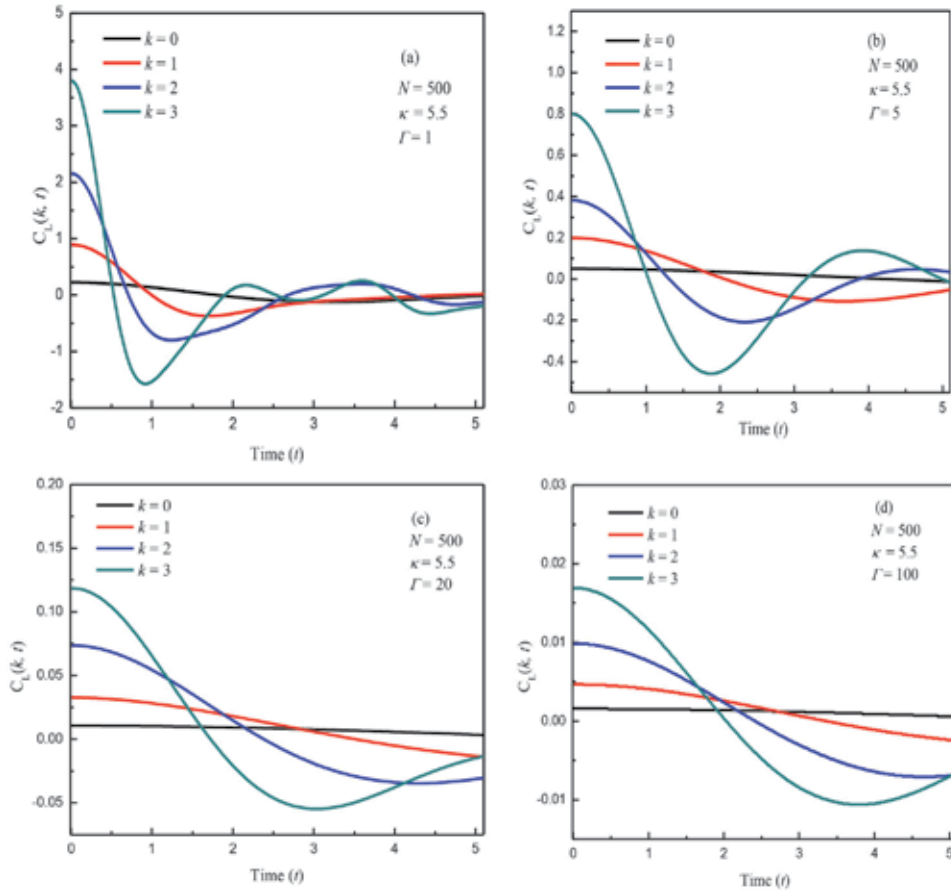


Figure 3.

EMD simulations results of wave spectra of the longitudinal mode against the simulations time (t) for $\kappa = 5.5$ covering from non-ideal to liquid states ((a) $\Gamma = 1$, (b) $\Gamma = 5$, (c) $\Gamma = 20$ (d) $\Gamma = 100$) of 3D SCDPs and $N = 500$ for higher wave number ($k = 0, 1, 2$ and 3).

0.0014 for $\Gamma = 1, 5, 20$ and 100 respectively at $\kappa = 4.5$ and $k = 0$. When we increase value of screening $\kappa = 4.5$ to 5.5 then the magnitude of $C_L(k, t)$ at $k = 0$ increase $0.2244, 0.0508, 0.0105$ and 0.0016 . In this chapter, we have simulated at an $N = 500$ for the same combination of parameters (N, κ, Γ).

In this part, we have investigate $C_T(k, t)$ through EMD simulations for 3D SCDPs coulomb system in the classical ensemble (NVT) for $N = 500$ particles. The charged particles are interacting with each other via Yukawa pair potential. We have analyzed the behavior of the wave's spectra in the transverse (shear wave) direction in SCDPs, using Eq. (8), by EMD simulations technique. It is found that our results is calculated for $C_T(k, t)$ are in a good agreement using the EMD algorithm over an extensive range of plasma parameters and selecting a number of particles. We have ensured that the presented results of $C_T(k, t)$ are in satisfactory agreement with prior known simulation, theoretical and numerical results. In our MD simulation result, the effect of plasma temperature is observed on amplitude, wavelength, frequency, and propagation of waves in SCDPs.

Figures 4 and **5** demonstrate the Simulation results which are obtained for $C_T(k, t)$ of SCDPs plasma using EMD simulations at $k = 0, 1, 2$ and $3, \Gamma = 1, 5, 20$ and 50 for $\kappa = 4.5$ and 5.5 . The given simulation results of $C_T(k, t)$ spectra are compared with increasing and decreasing sequences of κ, Γ , and k . It is observed that the magnitude of transverse current waves has increases behavior with increasing wave

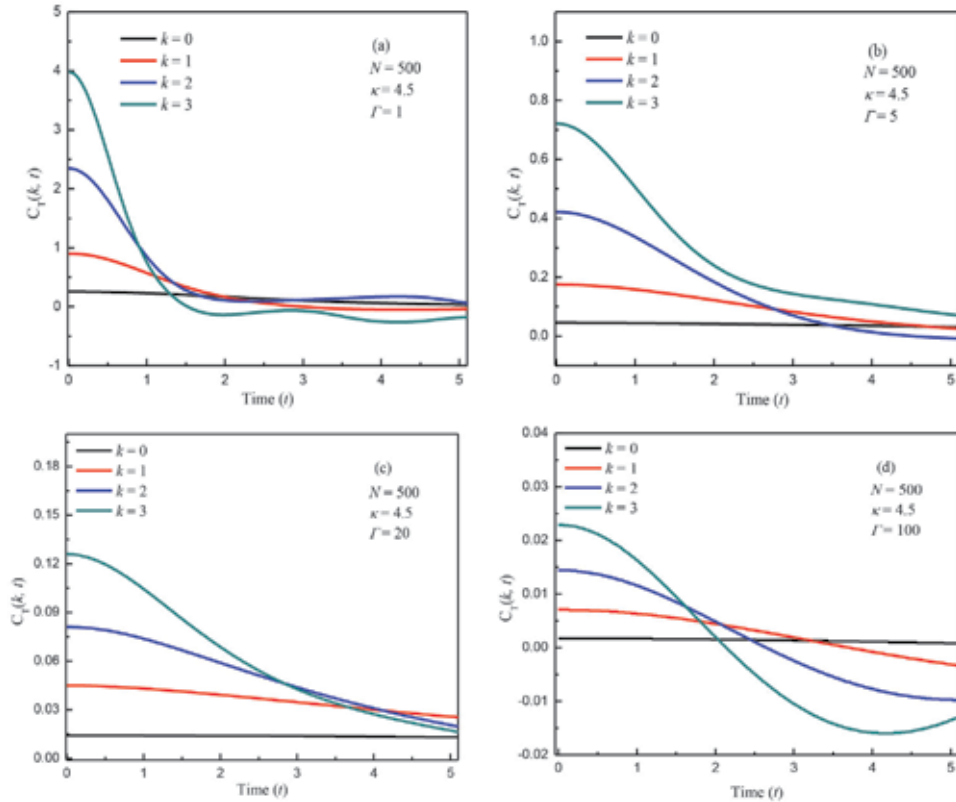


Figure 4. EMD simulations results of wave spectra of the transverse mode against the simulations time (t) for $\kappa = 4.5$ covering from non-ideal to liquid states ((a) $\Gamma = 1$, (b) $\Gamma = 5$, (c) $\Gamma = 20$ (d) $\Gamma = 100$) of 3D SCDPs and $N = 500$ for higher wave number ($k = 0, 1, 2$ and 3).

numbers. We have observed from further EMD simulations calculation that magnitudes of this wave have decreasing behavior for a high number of particles. The absence of any structure of strongly coupled plasma in the liquid phase the shear waves are not propagated through it. Wave's in SCDPs are highly damped at high plasma temperature or low values of coulomb coupling. In **Figure 4** plotted four panel of shear waves which covering from non-ideal to liquid state of dusty plasma.

The panel (a) of both **Figures 4** and **5** represent the results of $C_T(k, t)$ spectra in the non-ideal state of dusty plasma. It is observed from these figures that collective modes of wave spectra are highly damped at higher plasma temperature and damping of transverse waves reduce with corresponding to decrease the plasma temperature. In the non-ideal state of dusty plasma, the transverse current wave's mode is highly damped as compare to longitudinal modes especially at higher wave's number in our case. $C_T(k, t)$ spectra having increasing behavior in the magnitude for wave vector. The damping of waves at a higher temperature would attribute this to viscous/ collision and Landau damping that confirmed from earlier published work of [2, 30]. The effects of Γ on the propagation of waves in SCDPs are observed from four panels of **Figure 2**. The frequency modes are increases and amplitude decreases of $C_L(k, t)$ with increasing Γ . With increasing Γ the thermal effect decreases in the magnitude and the correlation effect clearly seems. Values of $C_T(k, t)$ at different parameters as for $k = 0(1)$, $C_T = 0.2558(0.9016)$, $0.0454(0.1749)$, $0.0141(0.0449)$, $0.0017(0.0071)$, and for the case $k = 2(3)$ as $C_T = 2.3453(3.9837)$, $0.4218(0.7214)$, $0.0810(0.1260)$, $0.0144(0.0229)$, at $\Gamma = 1, 5, 20, 100$ respectively for $\kappa = 4.5$. With the comparison of **Figures 4** and **5**, we have observed that there is a slight difference

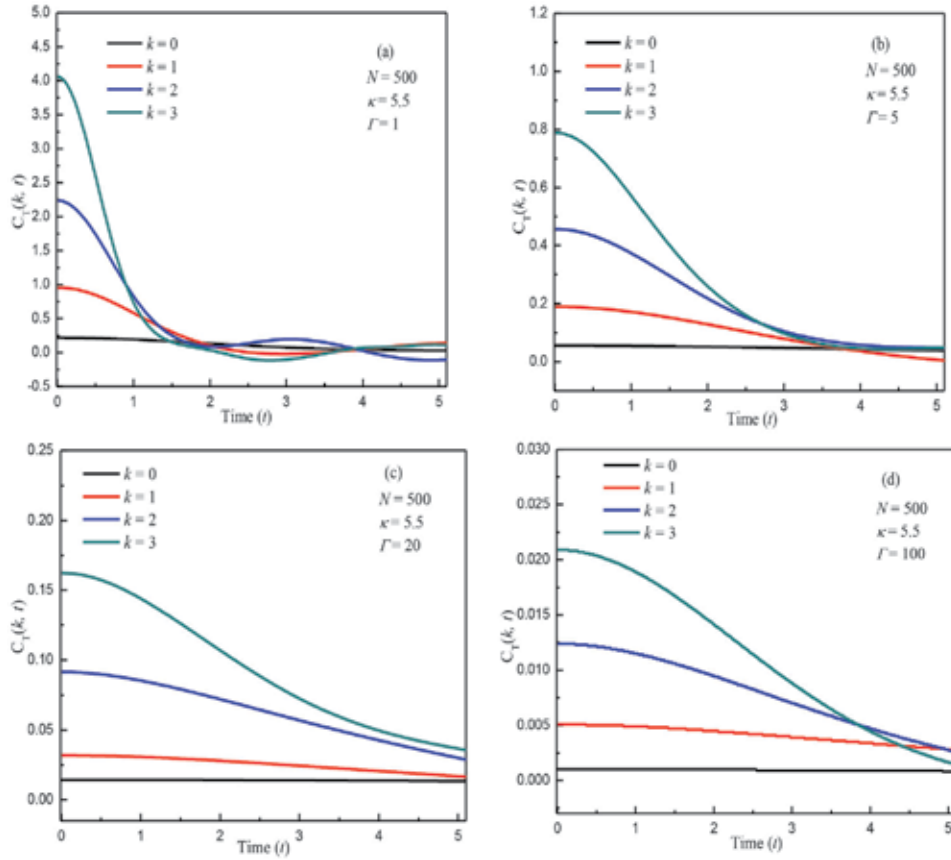


Figure 5. EMD simulations results of wave spectra of the transverse mode against the simulations time (t) for $\kappa = 5.5$ covering from non-ideal to liquid states ((a) $\Gamma = 1$, (b) $\Gamma = 5$, (c) $\Gamma = 20$ (d) $\Gamma = 100$) of 3D SCDPs and $N = 500$ for higher wave number ($k = 0, 1, 2$ and 3).

occurs when we increase the screening of dust charged particles. The propagation and damping behavior of waves in transverse direction remain nearly same with increasing screening. For particular wave's number (k), magnitudes of transverse waves have increasing behavior with increasing screening strength.

4. Summary

The EMD simulations are used to investigate the $C_L(k, t)$, and $C_T(k, t)$ for 3D SCDPs over an extensive range of plasma parameters κ , Γ , and k (wavenumber), N (number of particles in simulation box) and k . The first involvement of the presented simulation is that it delivers an understanding of propagation and damping phenomena of waves in SCDPs. In general, the amplitude, frequency of waves is analyzed. The presented simulation specifies that the waves are highly damped at high temperature $\Gamma = 1$, frequently propagates at intermediate and high value of $\Gamma = 20$ – 100 . This investigation shows that the values of frequency and amplitude depend on κ , Γ , N , and k . It has been shown that the presented EMD method and earlier EMD techniques have comparable performance over the wide range of plasma points, both yielding reasonable results for correlation parameters. New simulations give more reliable and excellent data for the $C_L(k, t)$, and $C_T(k, t)$ for a wider range of κ and Γ are (4.5, 5.5) and (1, 100). The existing simulations

deliver more reliable data for existence for waves in SCDPs. In the absence of structure in dusty plasma, the shear wave does not support. The sound wave frequently propagates at medium and higher values of Γ in SCDPs. It is suggested that the presented EMD technique based on Ewald summation described here can be used to explore other ionic and dipolar materials. It is very interesting what other types of interaction potentials support correction parameters of strongly coupled plasma and how its strengths depend on the range of new interaction potentials.

Acknowledgements

The authors thank the National Advanced Computing Centre of National Centre for Physics (NCP), Pakistan and National High-Performance Computing Center (NHPCC) of Xian Jiaotong University, P.R. China for allocating computer time to test and run our MD code.

Abbreviation and symbol

EMD	equilibrium molecular dynamic
κ	screening strength
Γ	Coulomb coupling
k	wavenumber (wave vector)
N	number of particles
DP	dusty plasma
SCDPs	strongly coupled dusty plasmas
3D	three dimensional
$C_L(k, t)$	longitudinal current wave
$C_T(k, t)$	transverse current wave
CDPs	complex dusty plasmas
WCDPs	weakly coupled dusty plasmas
NLS	noctilucent clouds
RFP	reverse field pinch
MFT	magnetized target fusion
PF	plasma focus
MIF	magneto-inertial fusion
K_B	Boltzmann constant
n	plasma density
p	plasma pressure
T	plasma temperature
β	normalized plasma pressure
α	the minor radius of the plasma
I	plasma toroidal current
DAW	dust acoustic wave
PBCs	periodic boundary condition
RF	radiofrequency
DC	discharge current
DTC	dust transport code
MD	molecular dynamic

Author details

Aamir Shahzad^{1,2*}, Muhammad Asif Shakoori² and Mao-Gang He²

1 Molecular Modeling and Simulation Laboratory, Department of Physics, Government College University Faisalabad (GCUF), Faisalabad, Pakistan

2 Key Laboratory of Thermo-Fluid Science and Engineering, Ministry of Education (MOE), Xi'an Jiaotong University, Xi'an, P.R. China

*Address all correspondence to: aamirshahzad_8@hotmail.com;
aamir.awan@gcuf.edu.pk

IntechOpen

© 2020 The Author(s). Licensee IntechOpen. This chapter is distributed under the terms of the Creative Commons Attribution License (<http://creativecommons.org/licenses/by/3.0>), which permits unrestricted use, distribution, and reproduction in any medium, provided the original work is properly cited. 

References

- [1] Rodriguez IJ. Some assembly required: computational simulations of dusty plasma [university honors theses]. Portland State University; 2018. p. 622. DOI: 10.15760/honors.622
- [2] Shahzad A, Shakoori MA, He M-G, Bashir S. Sound waves in complex (dusty) plasmas. In: *Computational and Experimental Studies of Acoustic Waves*. Croatia, London, UK: IntechOpen; 2018
- [3] Pironti A, Walker M. Fusion, tokamaks and plasma control: An introduction and tutorial. *IEEE Control Systems*. 2005;25(5):30-43
- [4] Mitic S. Physical processes in complex plasma [doctoral dissertation, lmu]. Ludwig Maximilian University of Munich; 2010
- [5] Goree J, Donkó Z, Hartmann P. Cutoff wave number for shear waves and Maxwell relaxation time in Yukawa liquids. *Physical Review E*. 2012;85(6):066401
- [6] Williams JD, Thomas E Jr. Initial measurement of the kinetic dust temperature of a weakly coupled dusty plasma. *Physics of Plasmas*. 2006;13(6):063509
- [7] Janaki MS, Banerjee D, Chakrabarti N. Shear waves in an inhomogeneous strongly coupled dusty plasma. *Physics of Plasmas*. 2011;18(9):092114
- [8] Kourakis I, Shukla PK. Nonlinear theory of solitary waves associated with longitudinal particle motion in lattices. *The European Physical Journal D: Atomic, Molecular, Optical and Plasma Physics*. 2004;29(2):247-263
- [9] Rapaport DC, Rapaport DCR. *The Art of Molecular Dynamics Simulation*. UK: Cambridge University Press; 2004
- [10] Shahzad A, He M-G. Thermal conductivity calculation of complex (dusty) plasmas. *Physics of Plasmas*. 2012;19(8):083707
- [11] Fisher RK, Thomas EE. Weakly coupled dusty plasma with a high dust temperature and low thermal energy density. *IEEE Transactions on Plasma Science*. 2013;41(4):784-787
- [12] Shukla PK, Mamun AA. *Introduction to Dusty Plasma Physics*. Bristol, UK: IOP Publishing; 2001
- [13] Kählert H, Melzer A, Puttscher M, Ott T, Bonitz M. Magnetic field effects and waves in complex plasmas. *The European Physical Journal D*. 2018;72(5):83
- [14] Kalman GJ, Hartmann P, Donkó Z, Rosenberg M. Two-dimensional Yukawa liquids: Correlation and dynamics. *Physical Review Letters*. 2004;92(6):065001
- [15] Shahzad A, He M-G, Shakoori MA. Thermal transport and non-newtonian behaviors of 3D complex liquids using molecular simulations. In: *2017 14th International Bhurban Conference on Applied Sciences and Technology (IBCAST)*; January; IEEE. 2017. pp. 472-474
- [16] Bacha M, Tribeche M, Shukla PK. Dust ion-acoustic solitary waves in a dusty plasma with nonextensive electrons. *Physical Review E*. 2012;85(5):056413
- [17] Ott T, Bonitz M. Diffusion in a strongly coupled magnetized plasma. *Physical Review Letters*. 2011;107(13):135003
- [18] Hamaguchi S, Ohta H. Waves in strongly-coupled classical one-component plasmas and Yukawa fluids. *Physica Scripta*. 2001;2001(T89):127

- [19] Das A, Tiwari SK, Kaw P, Sen A. Exact propagating nonlinear singular disturbances in strongly coupled dusty plasmas. *Physics of Plasmas*. 2014; **21**(8):083701
- [20] Grecu D, Grecu AT. Dusty Plasma in Space Sciences. Magurele, Bucharest, Romania: “Horia Hulubei”, National Institute of Physics and Nuclear Engineering; 2008
- [21] Liu Z, Wang D, Miloshevsky G. Simulation of dust grain charging under tokamak plasma conditions. *Nuclear Materials and Energy*. 2017; **12**:530-535
- [22] Bray CM. Dust Grain Charging in Tokamak Plasmas. Imperial College London: Department of Physics; 2014
- [23] Freidberg JP, Mangiarotti FJ, Minervini J. Designing a tokamak fusion reactor—How does plasma physics fit in? *Physics of Plasmas*. 2015; **22**(7): 070901
- [24] Clery D. Fusion’s Restless Pioneers. 2014. DOI: 10.1126/science.345.6195.370
- [25] Vooradi R, Bertran MO, Frauzem R, Anne SB, Gani R. Sustainable chemical processing and energy-carbon dioxide management: A review of challenges and opportunities. *Chemical Engineering Research and Design*. 2018; **131**:440-464
- [26] Zonca F, Briguglio S, Chen L, Fogaccia G, Hahm TS, Milovanov AV, et al. Physics of burning plasmas in toroidal magnetic confinement devices. *Plasma Physics and Controlled Fusion*. 2006; **48**(12B):B15
- [27] Lebedev SV, Giardi A, Ampleford DJ, Bland SN, Bott SC, Chittenden JP, et al. Magnetic tower outflows from a radial wire array Z-pinch. *Monthly Notices of the Royal Astronomical Society*. 2005; **361**(1): 97-108
- [28] He K, Chen H, Liu S. Effect of plasma absorption on dust lattice waves in hexagonal dust crystals. *Plasma Science and Technology*. 2018; **20**(4): 045001
- [29] Donkó Z, Hartmann P, Kalman GJ. Two-dimensional dusty plasma crystals and liquids. *Journal of Physics: Conference Series*. 2009; **162**(1):012016
- [30] Nunomura S, Zhdanov S, Samsonov D, Morfill G. Wave spectra in solid and liquid complex (dusty) plasmas. *Physical Review Letters*. 2005; **94**(4):045001
- [31] Marciniak Ł, Wójcik-Gargula A, Kulińska A, Bielecki J, Wiącek U. Diagnostic systems for the nuclear fusion and plasma research in the PF-24 plasma focus laboratory at the IFJ PAN. *Nukleonika*. 2016; **61**(4):413-418
- [32] Piel A, Nosenko V, Goree J. Experiments and molecular-dynamics simulation of elastic waves in a plasma crystal radiated from a small dipole source. *Physical Review Letters*. 2002; **89**(8):085004
- [33] Kaw PK, Sen A. Low-frequency modes in strongly coupled dusty plasmas. *Physics of Plasmas*. 1998; **5**(10):3552-3559
- [34] Donko Z, Kalman GJ, Hartmann P. Dynamical correlations and collective excitations of Yukawa liquids. *Journal of Physics: Condensed Matter*. 2008; **20**(41):413101
- [35] Hartmann P, Donkó Z, Kalman GJ, Kyrkos S, Golden KI, Rosenberg M. Collective dynamics of complex plasma bilayers. *Physical Review Letters*. 2009; **103**(24):245002
- [36] Li W, Huang D, Wang K, Reichhardt C, Reichhardt CJO, Murillo MS, et al. Phonon spectra of two-dimensional liquid dusty plasmas on a one-dimensional periodic substrate. 2018. arXiv preprint arXiv: 1809.09012

[37] Ciccotti G, Ferrario M, Schuette C.
Molecular dynamics simulation.
Entropy. 2014;**16**:233

[38] Shahzad A, He M-G. Thermal
conductivity of three-dimensional
Yukawa liquids (dusty plasmas).
Contributions to Plasma Physics. 2012;
52(8):667-675

[39] Shahzad A, He M-G. Computer
Simulation of Complex Plasmas:
Molecular Modeling and Elementary
Processes in Complex Plasmas. 1st ed.
Saarbrücken, Germany: Scholar's Press;
2014. p. 170

Measurement of Vacancy Migration Energy by Using HVEM

Pingping Liu

Abstract

Vacancy migration energy is a key factor for irradiation resistance of nuclear materials and also a fundamental parameter for modeling and should be experimentally calculated in advance. A new method together with a formula was developed for measuring the vacancy migration energy on high-voltage electron microscope (HVEM) from the temperature dependence of the growth speed of a dislocation loop in consideration of other sink effects including surface and grain boundary on point defects. Anti-noise property and the other characteristics of the three different methods have also been analyzed and discussed to help choose the appropriate method to measure the vacancy migration energy when in need in different situations.

Keywords: vacancy migration energy, in situ HVEM, measurement of E_m

1. Introduction

Fusion energy is one of the most promising carbon-free energy in the future. One problem limiting the development and application of fusion energy is the radiation damage of materials. Irradiation resistance of a material is determined by the motion and recombination of point defects (vacancy and interstitial) [1]. The motion and recombination of point defects are governed by the vacancy mobility at material service temperature which is always higher than the vacancy mobile temperature [1, 2]. Thus, vacancy migration energy is a critical factor for the ability of nuclear materials to resist radiation damage. Moreover, it is becoming a popular and an effective method to simulating the irradiation-induced microstructure changes to predict the mechanical properties of materials during irradiation with the development of computational materials. Vacancy migration energy is also a fundamental parameter for modeling and should be experimentally measured in advance.

Kiritani et al. have firstly proposed one method as early as the 1970s by experimentally measuring growth speed of interstitial dislocation loops at different irradiation temperatures to measure the motion of vacancies in iron by using HVEM [2, 3]. High-energy electron irradiation produces pure Frenkel point defect pairs, which is very beneficial to the fundamental research of point defect mobility. In combination with in situ heating sample holder, HVEM has been proven to be a powerful apparatus to investigate microstructural evolution and measure the vacancy migration energy under in situ high-energy electron irradiation. Since then, the method proposed by Kiritani et al. was often used to measure the vacancy migration energy of materials. The effects of impurities, helium, and hydrogen on

vacancy migration energy in pure Fe-based alloys, F82H and electron-beam-welded F82H joint, have been investigated by Hashimoto et al. [4–6]. The effect of deuterium on vacancy migration energy in Fe-10Cr alloy has also been investigated [7]. Point defect behavior in pure vanadium and its alloys were also analyzed under HVEM irradiation by using the method [8–10]. However, it is important to note that the method did not consider the effect of sample surface on the measurement of the vacancy migration energy. And, it is always very difficult to ensure that the observed loops are deep in the specimen (located so far apart from specimen surface) by HVEM stereo observation operation [11]. Thus, Wan et al. derived a new formula for calculation vacancy migration energy by considering the surface effect in the 1990s [11]. In this brilliant derivation, the effect of specimen surface was treated as a constant, and three data of growth rate at different irradiation temperatures were used once to numerically calculate the vacancy migration energy by iterated operation. This method considered the surface effect intrinsically, but iterated solution by using a computer is needed. This operation would produce two roots, in which one should choose the right one according to physical meaning. It is a little bit difficult to calculate and choose the right root. Probably for this reason, reference of using this numerical method is not many. Moreover, the effects of other sinks such as irradiation-induced small void, fine precipitates, and grain boundary on the growth speed of dislocation loops also needed to be considered when using HVEM to measure the vacancy migration energy.

In this chapter, other sinks such as surface, small void, precipitates, and grain boundary were taken into consideration to develop a new method for calculating vacancy migration energy according to the relationship of the reciprocal of irradiation temperature and growth speed of dislocation loops. An influential factor relating to the effects of other sinks was also presented in this new method. In addition, the formula derived by Wan et al. has also been rediscussed to avoid one root and help to choose the right root, which may encourage a broader range of applications of this numerical method. The characteristic of these three methods is discussed to help choose the appropriate method to measure the vacancy migration energy when in need in different situations. In addition, the motion interstitial is also important and could be measured by using HVEM [12, 13]. In this chapter, however, we only discussed the mobility of vacancy because vacancy moves much slower than that of interstitial, and the recombination of vacancies and interstitial defects is governed by the vacancy mobility at material service temperature which is higher than vacancy mobile temperature.

2. The calculation method

2.1 Linear method

This method was reported by Kiritani et al. [2] and Tabata et al. [14] in which several factors affecting the migration energy were discussed in detail. According to their analysis, the variations of the concentrations of interstitial atoms (C_i) and lattice vacancies (C_v) with the point defect mobility (M) at high temperature (at which vacancies are highly mobile) are given as follows:

$$\frac{dC_i}{dt} = P - Z_{iv}(M_i + M_v)C_iC_v - Z_{iL}M_iC_{sL}C_i - M_iC_{Si}C_i \quad (1)$$

and

$$\frac{dC_v}{dt} = P - Z_{iv}(M_i + M_v)C_iC_v - Z_{vL}M_vC_{sL}C_v - M_vC_{sv}C_v \quad (2)$$

where Z_{iv} , Z_L , and C_s denote the recombination coefficient, the number of reaction sites of dislocation loops and point defects, and concentration of sinks, respectively. And, t denotes the time. First term P is the production rate of free Frenkel pairs induced by HVEM. The second term is the mutual annihilation rate between interstitials and vacancies with the mutual annihilation cross-section of Z_{iv} . The third terms are the annihilation rate of each kind of point defect to dislocation loops whose concentration of atomic sites as sinks is C_{sL} and with absorption cross-sections Z_{iL} and Z_{vL} at each site for each point defect. The last terms are the annihilation at the surface sink. When a steady state of point defect concentrations is established, there is:

$$\frac{dC_i}{dt} = \frac{dC_v}{dt} = 0 \quad (3)$$

Then, both Eqs. (1) and (2) are equal to zero, and one can obtain the following equation:

$$(Z_{iL}C_{sL} + C_{si})M_iC_i = (Z_{vL}C_{sL} + C_{sv})M_vC_v \quad (4)$$

The most dominant terms of the point defect annihilation are the second terms in Eqs. (1) and (2), at least for the “thick-foil” case in which the last terms in the equations never become dominant. Then one can obtain the following, under the condition of $M_i \gg M_v$:

$$P = Z_{iv}M_iC_iC_v \quad (5)$$

Using Eqs. (4) and (5), the following equation could be obtained:

$$M_vC_v = \beta M_iC_i = \frac{\beta P}{Z_{iv}C_v} = \sqrt{\frac{\beta P M_v}{Z_{iv}}} \quad (6)$$

where $\beta = (Z_{iL}C_{sL} + C_{si}) / (Z_{vL}C_{sL} + C_{sv})$. Since C_{si} and C_{sv} are considered to be equal to each other and stay constant as long as the loop remains at the same fixed position in a specimen foil, the value β is thought to be slightly larger than unity because of the slightly larger capture cross-section Z_{iL} for interstitial than that for vacancy, Z_{vL} , at a dislocation loop and can be taken as constant (at least at a fixed temperature) though it varies slowly with the increase of C_{sL} by the growth of the dislocation loops [2].

The growth speed of interstitial loop of size R is expressed by the arrival rate to the loop of interstitial atoms in excess of vacancies and is:

$$\frac{dR}{dt} = a(Z_{iL}M_iC_i - Z_{vL}M_vC_v) = a \left(\frac{\frac{Z_{iL}}{\sqrt{\beta}} - \sqrt{\beta}Z_{vL}}{\sqrt{Z_{iv}}} \right) \sqrt{P} \sqrt{M_v} \quad (7)$$

where a is the increase of loop size by the absorption of one point defect per one site on the dislocation [2]. $Z_{iL}M_iC_i$ and $Z_{vL}M_vC_v$ are the ensemble of point defect fluxes captured by the loop. In order to reduce the effect of loop's size, the loops with same/similar initial size should be selected during experimental operation, which can be done relatively easily. Then, the equation can be written as:

$$\frac{dR}{dt} = C \cdot \exp\left(\frac{-E_m^v}{2kT}\right) \quad (8)$$

where k is the Boltzmann constant and C is an experimental constant. The above equation can be rewritten as:

$$\ln\left(\frac{dR}{dt}\right) = \ln C - \frac{E_m^v}{2kT} \quad (9)$$

Using this equation, the vacancy migration energy can therefore be obtained from the slope of a linear relationship between the logarithm of the growth rate of dislocation loops and the inverse of temperature. Here, we called this method “linear method.”

2.2 Numerical method

Using the “linear method” with Eq. (9), the vacancy migration energy can be calculated simply. However, the position of the dislocation loop must be deep in the thick foil to ensure the surface effect could be avoided. This makes the experiment more complex and difficult. Considering the surface effect of the sample, another brilliant derivation was developed by not avoiding the third and fourth terms of Eqs. (1) and (2) by Wan et al. [11].

When the point defect concentration is in a steady state, there is $dC_i/dt = dC_v/dt = 0$. And one can obtain an equation under the condition of $M_i \gg M_v$:

$$P = Z_{iv}M_iC_iC_v + Z_{vL}M_vC_{sL}C_v + M_vC_{sv}C_v = \frac{Z_{iv}}{\beta M_v}(M_vC_v)^2 + (Z_{vL}C_{sL} + C_{sv})M_vC_v \quad (10)$$

The former equation can be written as:

$$\frac{A_1}{M_v}(M_vC_v)^2 + B_1M_vC_v - P = 0 \quad (11)$$

where A_1 and B_1 are constant. The root of this equation is:

$$M_vC_v = \left(-B_1 \pm \sqrt{B_1^2 + \frac{4PA_1}{M_v}}\right) \frac{M_v}{2A_1} \quad (12)$$

Substituting Eq. (12) into Eq. (7), one can obtain:

$$\frac{dR}{dt} = a(Z_{iL}M_iC_i - Z_{vL}M_vC_v) = a\left(\frac{Z_{iL}}{\beta} - Z_{vL}\right)M_vC_v = \left(B_2 \pm \sqrt{B_2^2 + \frac{A_2}{M_v}}\right)M_v \quad (13)$$

where A_2 and B_2 are constant. This equation can be changed to be:

$$\exp\left(\frac{E_m}{kT}\right)\left(\frac{dR}{dt}\right)^2 - B_3\left(\frac{dR}{dt}\right) - A_3 = 0 \quad (14)$$

Letting $dR/dt = V$, the above equation can be expressed as:

$$\exp\left(\frac{E_m}{kT}\right)V^2 - B_3V - A_3 = 0 \quad (15)$$

By HVEM observation, V_1 , V_2 , and V_3 at temperatures T_1 , T_2 , and T_3 can be obtained, respectively. Using these data in Eq. (15) and getting rid of the constant, there is:

$$\frac{V_1 - V_2}{V_2 - V_3} = \frac{V_1^2 \exp\left(\frac{E_m}{kT_1}\right) - V_2^2 \exp\left(\frac{E_m}{kT_2}\right)}{V_2^2 \exp\left(\frac{E_m}{kT_2}\right) - V_3^2 \exp\left(\frac{E_m}{kT_3}\right)} \quad (16)$$

Letting $(V_1 - V_2)/(V_2 - V_3) = V_0 > 0$ and substituting it in Eq. (16), the vacancy migration energy is given as follows:

$$a_1 \cdot \exp(E_m \cdot b_1) + a_2 \cdot \exp(E_m \cdot b_2) - 1 = 0 \quad (17)$$

where

$$a_1 = \frac{V_1^2}{(1 + V_0)V_2^2}, a_2 = \frac{V_0V_3^2}{(1 + V_0)V_2^2}, b_1 = \frac{1}{k} \left(\frac{1}{T_1} - \frac{1}{T_2} \right), b_2 = \frac{1}{k} \left(\frac{1}{T_3} - \frac{1}{T_2} \right)$$

and where k is the Boltzmann constant. Eq. (17) can be solved by using a computer. A Python program example for solving Eq. (17) is given in the Appendix. According to Eq. (17), two mathematical results would be obtained. In this case it is necessary to select one of these two results by the physical meaning. Sometimes, one will have a little difficulty in choosing the correct result. Probably for this reason, the application of this method had been limited.

The derivation was discussed here again to help select the result of Eq. (17). Two roots were induced by the Eq. (11) firstly. We can avoid one root directly in Eq. (12) by the physical meaning:

$$2A_1C_v > 0$$

where $A_1 = Z_{iv}/\beta > 0$, C_v is the concentration of the vacancy. So, Eq. (12) could be rewritten as:

$$M_v C_v = \left(-B_1 + \sqrt{B_1^2 + \frac{4PA_1}{M_v}} \right) \frac{M_v}{2A_1} \quad (18)$$

The Eq. (13) can also be changed to:

$$\frac{dR}{dt} = a(Z_{iL}M_iC_i - Z_{vL}M_vC_v) = \left(B_2 + \sqrt{B_2^2 + \frac{A_2}{M_v}} \right) M_v \quad (19)$$

There should be only one root for E_m in the Eq. (15) in which A_3 and B_3 are constant. Thus, one knows to choose the big one of the two results from Eq. (17). Only one result will be obtained. This may encourage a broader range of applications of this method as it considers the surface effect intrinsically. We called this method “numerical method” here because of numerical calculating of the vacancy migration energy by iterated operation [15].

2.3 Nonlinear method

Using linear method, the vacancy migration energy could be obtained simply with no consideration of the surface effect. In order to ensure the surface effect could be avoided, however, the position of the dislocation loop must be deep which is difficult sometimes and will make the HVEM experiment more complex. Considering other sink effects such as surface, small void, precipitates, and grain boundary, some terms were added in Eqs. (1) and (2):

$$\frac{dC_i}{dt} = P - Z_{iv}(M_i + M_v)C_iC_v - Z_{iL}M_iC_{sL}C_i - Z_{io}M_iC_{so}C_i - Z_{iP}M_iC_{sP}C_i - Z_{iB}M_iC_{sB}C_i - M_iC_{si}C_i \quad (20)$$

$$\frac{dC_v}{dt} = P - Z_{iv}(M_i + M_v)C_iC_v - Z_{vL}M_vC_{sL}C_v - Z_{vo}M_vC_{so}C_v - Z_{vP}M_vC_{sP}C_v - Z_{vB}M_vC_{sB}C_v - M_vC_{sv}C_v \quad (21)$$

where Z_{iv} , Z_L , and C_s denote the recombination coefficient, the number of reaction sites of dislocation loops, and point defects and density of sinks, respectively. The first term P is the production rate of free Frenkel pairs induced by HVEM. The second term is the mutual annihilation between interstitials and vacancies. The third terms are the annihilation rate of each kind of point defect to dislocation loops whose concentration of atomic sites as sinks is C_{sL} and with absorption cross-sections Z_{iL} and Z_{vL} at each site for each point defect. The fourth, fifth, and sixth terms are the ensemble of annihilation of each kind of point defect to void, precipitates, and grain boundary, respectively. It is worth noting that these three kinds of sinks mean a very small one or inconspicuous one which could not be observed by HVTEM at the same magnification times as observing the whole loop. One can avoid it directly during the TEM observation if the void or precipitates are big enough, which will not be discussed here. The seventh terms express the escape of point defects to the surface sink. Under the condition of $M_i \gg M_v$ and the steady state of point defect concentrations ($\frac{dC_i}{dt} = \frac{dC_v}{dt} = 0$), Eqs. (20) and (21) can be written as:

$$P = Z_{iv}M_iC_iC_v + Z_{vL}M_vC_{iL}C_v + Z_{vo}M_vC_{so}C_v + Z_{vP}M_vC_{sP}C_v + Z_{vB}M_vC_{sB}C_v + M_vC_{sv}C_v \quad (22)$$

Then, there is:

$$\frac{Z_{iv}}{\beta M_v}(M_vC_v)^2 + (Z_{vL}C_{sL} + Z_{vo}C_{so} + Z_{vP}C_{sP} + Z_{vB}C_{sB} + C_{sv})M_vC_v - P = 0 \quad (23)$$

where $\beta = (Z_{iL}C_{sL} + Z_{io}C_{so} + Z_{iP}C_{sP} + Z_{iB}C_{sB} + C_{si}) / (Z_{vL}C_{sL} + Z_{vo}C_{so} + Z_{vP}C_{sP} + Z_{vB}C_{sB} + C_{sv})$.

Set $a_1 = \frac{Z_{iv}}{\beta}$ and $b_1 = Z_{vL}C_{sL} + Z_{vo}C_{so} + Z_{vP}C_{sP} + Z_{vB}C_{sB} + C_{sv}$. According to the physical meaning, a_1 and b_1 are constant larger than zero. The above equation can be written as:

$$\frac{a_1}{M_v}(M_vC_v)^2 + b_1M_vC_v - P = 0 \quad (24)$$

The root of Eq. (24) is:

$$M_vC_v = \left(-b_1 \pm \sqrt{b_1^2 + \frac{4Pa_1}{M_v}} \right) \frac{M_v}{2a_1} \quad (25)$$

According to the physical meaning, $M_v C_v$ should be larger than zero, while $(-b_1 - \sqrt{b_1^2 + \frac{4Pa_1}{M_v}}) \frac{M_v}{2a_1} < 0$. Anyway, substituting Eq. (25) into Eq. (7), the following equation can be obtained:

$$\frac{dr}{dt} = a \left(\frac{Z_{iL}}{\beta} - Z_{vL} \right) M_v C_v = \left(b_2 \pm \sqrt{b_2^2 + \frac{a_2}{M_v}} \right) M_v \quad (26)$$

where a is the change of loop radius by the absorption of one point defect per one site on the dislocation [2].

$\left(\frac{Z_{iL}}{\beta} - Z_{vL} \right) \approx (Z_{iL} - Z_{vL}) = L_{bias}$, thus, $a_2 = \frac{a^2 P L_{bias}^2}{a_1}$ and $b_2 = \frac{-b_1 a L_{bias}}{2a_1}$.
 Eq. (26) can be changed into:

$$\exp \left(\frac{E_m}{kT} \right) \left(\frac{dr}{dt} \right)^2 - b_3 \left(\frac{dr}{dt} \right) - a_3 = 0 \quad (27)$$

where $a_3 = 1/4a_2$, $b_3 = b_2$. The above equation can be written as:

$$\exp \left(\frac{E_m}{kT} \right) = a_3 \left(\frac{dt}{dr} \right)^2 + b_3 \left(\frac{dt}{dr} \right) \quad (28)$$

As a_3 , b_3 and $\frac{b_3^2}{4a_3} = \frac{b_2^2}{a_2} = \frac{b_1^2}{4Pa_1}$ are constant. There is a constant d to hold the following equation:

$$d * \exp \left(\frac{E_m}{kT} \right) = a_3 \left(\frac{dt}{dr} + \frac{b_3}{2a_3} \right)^2 \quad (29)$$

From the above equation, one can obtain:

$$\frac{1}{T} = \frac{2k}{E_m} * \ln \left(\frac{dt}{dr} + B_1 \right) + C_1 \quad (30)$$

where $B_1 = b_3/2a_3$ and C_1 is constant. By HVEM observation and getting dt/dr [$1/(dr/dt)$] data at different temperatures, the E_m can be obtained by this equation. In order to plot easily, the equation can be rewritten as:

$$\frac{1000}{T} = A * \ln \left(\frac{1}{(dr/dt)} + B \right) + C \quad (31)$$

Note: $A = 2k*1000/E_m$, $B = -b_1/(a*P)$ is a negative constant relating to total effects of all other sinks. Thus, from the function of $1/(dr/dt)$ and $1/T$, the E_m can be obtained by plotting the curve according to Eq. (31).

3. Discussion

Measurement of vacancy motion in solid state materials is a challenging work. There are not so many experimental methods. In situ HVEM has been proven to be one of the powerful tools to obtain vacancy migration energy by measuring the temperature dependence of the growth speed of a dislocation loop during electron irradiation. A reasonable phenomenological model of the loop growth could be selected and applied to extract the vacancy migration energy from the experimental

data. Kiritani et al. firstly proposed one linear model to calculate the vacancy migration energy. Then, Wan et al. derived a new formula by considering the surface effect. In this chapter, a new nonlinear model was developed by considering the other sink effects such as surface, small void, small precipitates, and grain boundary, and the numerical method was rediscussed. When the measured experimental data are ideal, not affected by the surface or other defect sinks, the vacancy migration energy value calculated by the three methods should be the same. One experimental example for calculating the vacancy migration energy by using the three methods was given here. The sample was Fe-10Cr model alloy which was pre-implanted by He and H ion sequentially. Then electron irradiation and in situ observation were carried out in HVEM at 573, 673, and 773 K. At a corresponding temperature, the growth rates of dislocation loop were measured [15]. But, the $\ln(dR/dt)$ and $1/T$ calculated from the experimental data were not strict linear that means there may be influences from the sample surface or other sinks. Thus, three assumed ideal values of the growth rate which are close to the three experimental values were selected to test the three methods, which are about 1.1 nm/min at 573 K, 3.5 nm/min at 673 K, and 8.1 nm/min at 773 K, respectively. According to these values, the $\ln(dR/dt)$ and $1/T$ followed a strict linear relationship, which means an ideal situation without the effect of other sinks. Then, the three methods were used to calculate the vacancy migration energy in this ideal case, and the results were shown in **Figure 1**. **Figure 1(a)** showed the result calculated by the linear method where blue squares are the experimental data and red pentagrams are the ideal values. The result calculated by the numerical method was shown in **Figure 1(b)**; the solving process example of the Eq. (17) was given in the Appendix. **Figure 1(c)** showed the result calculated by the nonlinear method where the horizontal axis

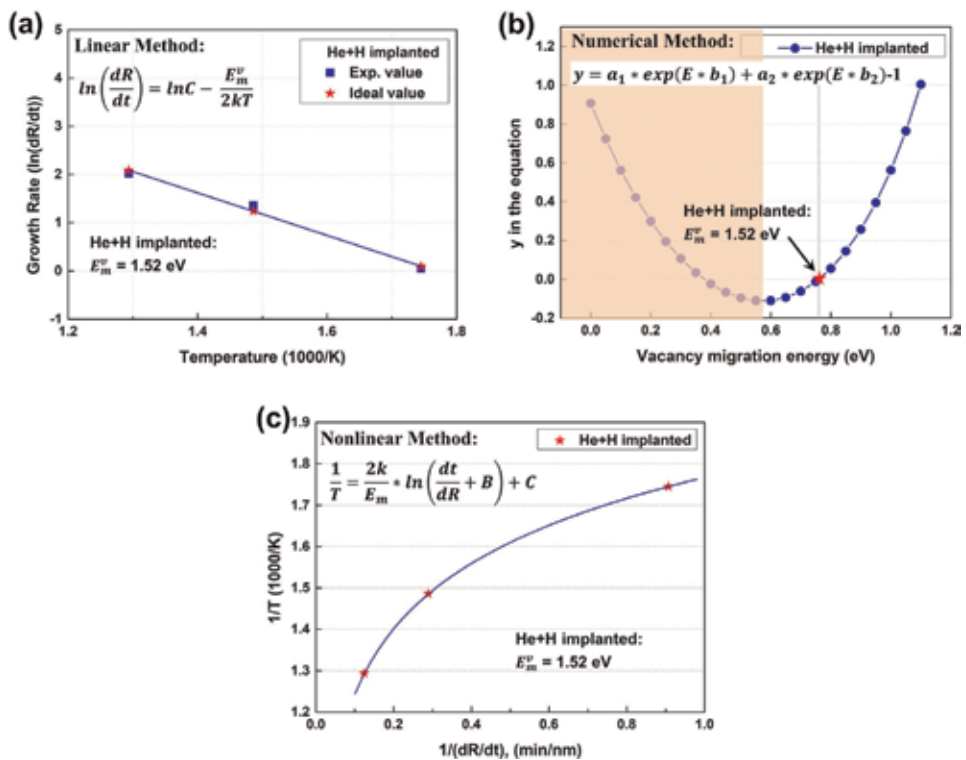


Figure 1. Measurement of vacancy migration energy in sequential-(He+H) ion implanted Fe-10Cr samples according to the ideal values by using linear method (a), numerical method (b), and nonlinear method (c), respectively.

Methods	Considering surface effect	Considering other sinks effect	Anti-noise property
Linear method	No	No	Very good
Numerical method	Yes	No	—
Nonlinear method	Yes	Yes	Good

Table 1.
 The characteristics of three methods for measuring vacancy migration energy.

represents the inverse of the growth rate and the vertical axis represents the inverse of temperature. These results indicated that the vacancy migration energy value calculated by the three methods according to ideal values in He+H pre-implanted Fe-10Cr sample was the same which was about 1.52 eV, while the vacancy migration energy values calculated by a different method according to the experimental data were different because of the different characteristics of the method. The characteristics of three methods for measuring vacancy migration energy were listed in **Table 1**.

In addition, if the linear fitting degree is larger than 0.9 which means the effect of other sinks was not dominated, linear model was preferred to fitting the experimental data and obtaining the value of vacancy migration energy because it is very simple. Otherwise, nonlinear model or numerical method should be used in considering the surface effect and other sink effect intrinsically. And, the overall influence of other sinks was also given as an influence factor (B) in the nonlinear model. It is worth to note that the “nonlinear method” has one more parameter than “linear method,” which means there is a bigger possibility for overfitting problem to arise. Thus, one should notice that parameter B should be negative according to Eq. (31) to avoid the overfitting problem. Another thing which needs to be noted is that $M_i \gg M_v$ is appropriate for pure metals, but $M_v > M_i$ may exist for some alloys [11, 16, 17]. The anti-noise property and the result reliability of different methods were also discussed in Ref. [18] and listed in **Table 1**. Then, one can choose an appropriate method to measure the vacancy migration energy according to the anti-noise property, result reliability, and other characteristics of the three different methods.

4. Summary

In summary, the methods to measure the vacancy migration energy by using HVEM were described and discussed in this chapter. Considering other sinks effects, a new nonlinear method was developed to measure vacancy migration energy according to the relationship of the reciprocal of irradiation temperature and growth speed of dislocation loops. Meanwhile, an influential factor relating to the effects of other sinks was also presented. The characteristics of three methods for measuring vacancy migration energy were also discussed in detail, which can help to select the appropriate method to measure the vacancy migration energy in different situations.

Acknowledgements

This work is supported by the National Natural Science Foundation of China (Grant Nos. 51601012, U1637210, 11775018, 51571021). The authors gratefully

acknowledge the HVEM laboratory in Hokkaido University, Japan. The help and suggestions from Professor Q. Zhan and F.R. Wan at University of Science and Technology Beijing and Professor S. Ohnuki at Hokkaido University were highly appreciated.

Appendix

Python program example (He+H implanted sample for example) for solving Eq. (17) is given here. Two methods were tried to solve Eq. (17). One is Newton iteration method and another is directly plotting the curve. Here we paste the program to illustrate the solving of Eq. (17) by directly plotting, which may be the simplest and most effective method.

```
#Python 3.6
#Filename: Cal Em by using Numerical Method plot curve of Em

import numpy as np
import pandas as pd
import matplotlib.pyplot as plt

print('-----')
print('Import the growth rate data of He+H implantation...')

(t,v)=np.loadtxt('.\\loop growth rate_He+H.txt', skiprows=1, unpack=True)

print('T(K)', 'V(nm/min)')
print(t[0],v[0])
print(t[1],v[1])
print(t[2],v[2])

v0=(v[0]-v[1])/(v[1]-v[2])
v0=float('%0.5f'%v0)
print('\nV0 is:',v0)

a1=(v[0]*v[0])/((1+v0)*v[1]*v[1])
a1=float('%0.5f'%a1)
a2=(v0*v[2]*v[2])/((1+v0)*v[1]*v[1])
a2=float('%0.5f'%a2)
b1=100000*(1/t[0]-1/t[1])/8.6
b1=float('%0.5f'%b1)
b2=100000*(1/t[2]-1/t[1])/8.6
b2=float('%0.5f'%b2)

print('\ny=a1*exp(E*b1)+a2*exp(E*b2)-1')
print('a1 ',b1 ',a2 ',b2)
print(a1,b1,a2,b2)

#Plotting of Em of He+H-implanted sample
x=np.arange(0,1.1,0.000005)

#y=a1*exp(x*b1)+a2*exp(x*b2)-1, is not available here, use y=y1+y2
y1=a1*np.exp(x*b1)
```

```
y2=a2*np.exp(x*b2)-1
y=y1+y2

i=len(x)-1
while y[i]>0.00001:
    i=i-1
else:
    print('Em:',2*x[i]) #M. Kiritani, H. Takata, K. Moriyama, et al., Philos. Mag. A,
40 (1979) 779-802.
    print('y:',y[i])

He+H_data={'y=a1*exp(x*b1)+a2*exp(x*b2)-1':y,
           'Em':x}
df1=pd.DataFrame(He+H_data)
df1.to_csv('.\\He+H_data.csv')

plot1=plt.plot(x,y,'r',label='He+H implanted')

plt.xlabel('E')
plt.ylabel('y in the equation')
plt.legend(loc=2)

plt.show()
plt.savefig('p1.png')
```


Author details

Pingping Liu

School of Materials Science and Engineering, University of Science and Technology
Beijing, Beijing, China

*Address all correspondence to: ppliu@ustb.edu.cn

IntechOpen

© 2019 The Author(s). Licensee IntechOpen. This chapter is distributed under the terms of the Creative Commons Attribution License (<http://creativecommons.org/licenses/by/3.0>), which permits unrestricted use, distribution, and reproduction in any medium, provided the original work is properly cited. 

References

- [1] Ackland G. Controlling radiation damage. *Science*. 2010;**327**(5973): 1587-1588
- [2] Kiritani M, Takata H, Moriyama K, et al. Mobility of lattice vacancies in iron. *Philosophical Magazine A*. 1979; **40**(6):779-802
- [3] Kiritani M, Yoshida N, Takata H, et al. Growth of interstitial type dislocation loops and vacancy mobility in electron irradiated metals. *Journal of the Physical Society of Japan*. 1975; **38**(6):1677-1686
- [4] Hashimoto N, Sakuraya S, Tanimoto J, et al. Effect of impurities on vacancy migration energy in Fe-based alloys. *Journal of Nuclear Materials*. 2014;**445** (1-3):224-226
- [5] Hashimoto N, Tanimoto J, Kubota T, et al. Analysis of helium and hydrogen effect on RAFS by means of multi-beam electron microscope. *Journal of Nuclear Materials*. 2013;**442**(1-3):S796-S799
- [6] Hashimoto N, Tanigawa H, Kinoshita H, et al. Multiple-beam irradiation effects in electron-beam-welded F82H joint. *Journal of Nuclear Materials*. 2011; **417**(1-3):1009-1012
- [7] Liu PP, Bai JW, Ke D, et al. Effects of deuterium implantation and subsequent electron irradiation on the microstructure of Fe-10Cr model alloy. *Journal of Nuclear Materials*. 2012; **423**(1):47-52
- [8] Nishizawa T, Sasaki H, Ohnuki S, et al. Radiation damage process of vanadium and its alloys during electron irradiation. *Journal of Nuclear Materials*. 1996;**239**:132-138
- [9] Muroga T, Araki K, Yoshida N. Defect Behavior and Microstructural Evolution in Vanadium-Base Alloys Under Irradiation in a High-Voltage Electron Microscope. In: Klueh R, Gelles D, Okada M, Packan N, editors. *Reduced Activation Materials for Fusion Reactors*. West Conshohocken, PA: ASTM International; 1990. p. 199-209
- [10] Liu PP, Du YF, Han WT, et al. Effects of hydrogen on point defect mobility in vanadium under electron irradiation. 2019. Under review
- [11] Wan F, Xiao J, Yuan Y. Measurement of vacancy migration energy by electron irradiation. *Acta Metallurgica Sinica*. 1990;**26**(2):A150-A154
- [12] Yoshida N, Kiritani M, Fujita FE. Electron radiation damage of iron in high voltage electron microscope. *Journal of the Physical Society of Japan*. 1975;**39**(1):170-179
- [13] Yoshida N, Kiritani M. Point defect clusters in electron-irradiated gold. *Journal of the Physical Society of Japan*. 1973;**35**(5):1418-1429
- [14] Tabata T, Fujita H, Ishii H, et al. Determination of mobility of lattice vacancies in pure iron by high voltage electron microscopy. *Scripta Metallurgica*. 1981;**15**(12):1317-1321
- [15] Liu PP, Zhan Q, Han WT, et al. Effect of helium and hydrogen synergy on vacancy migration energy in Fe-10Cr model alloy. *Journal of Alloys and Compounds*. 2019;**788**:446-452
- [16] Takahashi H, Hidaka Y, Ohnuki S. Observation of point defect production and clustering by high voltage electron microscopy: Interaction of point defect with solutes. *Micron*. 1996;**27**(3-4): 239-246
- [17] Doyama M. Point defect and defect interaction in metals. In: *Proceedings of the Yamada Conference V*. University of Tokyo Press; 1982. p. 643
- [18] Liu P P, Zhan Q, Ohnuki S, et al. New method for measurement of vacancy migration energy in electron irradiated FeCr-(He) alloy with several types of sinks. 2019. Under review

The Tungsten-Based Plasma-Facing Materials

Tao Zhang, Zhuoming Xie, Changsong Liu and Ying Xiong

Abstract

The plasma-facing materials in fusion reactors will face very extreme servicing condition such as high temperatures, high thermal loads, extreme irradiation conditions induced by high-energy neutron, and high fluences of high-flux and low-energy plasma. Tungsten is considered as the most promising material for plasma-facing components (PFCs) in the magnetic confinement fusion devices, due to its high melting temperature, high thermal conductivity, low swelling, low tritium retention, and low sputtering yield. However, some important shortcomings such as the irradiation brittleness and high ductility-brittle transition temperature of pure tungsten limit its application. Focusing on this issue, various W alloys with enhanced performance have been developed. Among them, nanoparticle dispersion strengthening such as oxide particle dispersion-strengthened (ODS-W) and carbide particle dispersion-strengthened (CDS-W) tungsten alloys and W fiber-reinforced W_f/W composites are promising. This chapter mainly reviews the preparation, microstructure, properties, regulation, and service performance evaluation of ODS-W, CDS-W, and W_f/W materials, as well as future possible development is proposed.

Keywords: W alloy, plasma-facing materials, fabrication, performance

1. Introduction

The development of high-performance materials is the major concern for realizing magnetic confinement fusion reactors. The plasma-facing materials (PFMs) work under extreme conditions including high-energy neutron (14.1 MeV) bombardments, severe thermal loads (up to 20 MWm^{-2}), and high fluences of high-flux ($>10^{21} \text{ m}^{-2} \text{ s}^{-1}$) and low-energy ($<100 \text{ eV}$) hydrogen and helium plasma irradiations [1–3]. The tolerable peak power of the plasma-facing components (PFCs), like the divertor targets, imposes significant restrictions on the design of future fusion reactors such as demonstration (DEMO) reactor or China fusion engineering experiment reactor (CFETR) [4]. Developing advanced materials with improved properties could substantially improve the performance of such PFCs.

Tungsten (W) is a kind of refractory metals that has supreme properties such as high melting temperature, high thermal conductivity, good erosion resistance, low vapor pressure, low swelling, and low tritium retention [1, 5, 6]. These properties are appealing for applications as PFCs in future fusion facilities. However, high brittleness in several regimes including low-temperature embrittlement (relatively high ductile-brittle transition temperature (DBTT)), irradiation embrittlement, and recrystallization embrittlement [7, 8] is one of the main disadvantages, which

limits the engineering application of W alloys, particularly in the nuclear energy fields [3, 9, 10]. The thermal load resistance of material is also intimately linked to the strength and DBTT, because the cracks would initiate when the thermal stress is larger than the ultimate strength of material at temperatures above DBTT or than the yield strength at temperatures below DBTT [11–14]. Currently, the performance of pure W can constrainedly satisfy the ITER servicing condition, but for the CFETR and DEMO with higher working parameters, it is not enough. Therefore, tungsten materials with more excellent mechanical properties, high-temperature stability, and irradiation resistance would be highly desirable for PFCs in future fusion reactors.

For tungsten alloys, decreasing DBTT has been a major goal over recent decades. It is generally understood that the low ductility of tungsten is closely related to their weak grain boundary (GB) cohesion, due to the segregation of interstitial impurities, such as O at GBs [15, 16]. In this sense, methods that purify impurity at GBs should be effective to improve the strength and ductility of tungsten. However at high temperatures (above 1000°C), the strength of pure W decreases significantly [17, 18]. Recent research results indicated that trace active elements, such as Zr, Ti, and Y, in tungsten can react with oxygen and diminish the influence of free oxygen on GBs via forming thermally stable nano-oxide particles and thus purify and strengthen the GBs, raising the stability at high temperature [19–21].

Therefore, several approaches are developed to improve the mechanical properties such as increasing ductility and fracture toughness and decreasing the DBTT. First, tungsten materials with high strength and high thermal stability can be obtained by the dispersing second-phase particles, such as oxides or carbides forming the oxides or carbides and dispersion-strengthened (ODS or CDS) tungsten-based materials [22–30]. Recently, various ODS-W or CDS-W materials with enhanced strength and thermal stability were fabricated and investigated for fusion applications [3, 30]. For example, W-La₂O₃ and W-Y₂O₃ showed enhanced strength, high recrystallization temperatures, and high thermal shock resistance [3, 24, 31]. Carbides such as TiC, ZrC, and HfC have much higher melting temperatures than that of the abovementioned oxides and better compatibility with tungsten, which may lead to excellent comprehensive performances in CDS-W. For example, an ultrafine-grained (UFG) W-1.1%TiC fabricated by severe plastic deformation exhibits a very high bending strength up to ~4.4 GPa and appreciable ductility at room temperature (RT) [23]. Zhang et al. [14, 28, 31] developed a bulk W-ZrC alloy with a flexural strength of 2.5 GPa and a strain of 3% at room temperature (RT) and a DBTT of less than 100°C. In addition, the W-ZrC alloy plate can sustain 4.4 MJ/m² thermal load without any cracks at RT. The low-energy and high-flux plasma irradiation resistance of this W-ZrC alloy is better than that of W-La₂O₃, ITER grade pure W, and commercial pure W; the hydrogen retention is also lower than that of ITER grade pure W [31]. W fiber-reinforced W_f/W composites also provide a good candidate for PFCs. In this chapter, the comprehensive introduction of the abovementioned materials will be reviewed.

2. Oxide dispersion-strengthened W-based materials

In ODS-W, nanoscaled oxides pin and hinder the migration of grain boundaries and dislocations in tungsten matrix, which improved the mechanical properties such as strength, recrystallization temperatures, and creep resistance. In addition, the dispersion of nanoscaled particles provides a large amount of phase interfaces that could act as sinks for irradiation-induced point defects and thus has the potential in improving the irradiation resistance [29, 31]. For instance, W-(0.3–1.0–2.0)wt%Y₂O₃ produced by mechanical alloying (MA) and hot isostatic pressing (HIPing) or microwave sintering has fine grains with the grain sizes ranging between 20 and 500 nm and containing a

high density ($5.4\text{--}6.9 \times 10^{22} \text{ m}^{-3}$) of nanosized Y_2O_3 particles with sizes between 1 and 50 nm [32, 33]. These refined grains and nanosized particles produce high densities of GB/PB interfaces, which generate high strength and a promising radiation resistance. To improve the ductility $\text{W-Y}_2\text{O}_3$ materials, different sintering and posttreatments such as spark plasma sintering (SPS) and high-temperature sintering in combination with hot rolling or hot forging deformation were used [34–38]. The performances of these $\text{W-Y}_2\text{O}_3$ were investigated as potential plasma-facing materials with respect to microstructures, thermal physical properties, mechanical properties, and thermal shock response when exposed to electron beam bombardment. For SPSed $\text{W-Y}_2\text{O}_3$, the tungsten grain exhibits an isotropic microstructure with an average grain size of 3.2 μm ; the average of Y_2O_3 particles is about 80 nm [38]. For the sintered $\text{W-Y}_2\text{O}_3$ in flowing H_2 , Y_2O_3 particles are located at the grain boundaries with a typical bimodal size distribution, i.e., composing of two portions of particles with particle size of ~ 0.68 and 1.1–1.7 μm , respectively, and the average grain size of tungsten is about 3 μm [34]. The thermal conductivity of deformed $\text{W-Y}_2\text{O}_3$ showed nearly 35% and 17% higher values than that of SPSed $\text{W-Y}_2\text{O}_3$ at RT and at 1473 K, respectively [34]. The tensile tests showed that the deformed $\text{W-Y}_2\text{O}_3$ is ductile in the investigated temperature range of 673–1273 K with the total elongation between 4% and 10%. Three-point bending tests indicated that the deformed $\text{W-Y}_2\text{O}_3$ had a better mechanical strength and toughness. The determination of thermal shock response revealed a superior thermal shock resistance of the hot rolled $\text{W-Y}_2\text{O}_3$ [34]: no cracks but only surface roughening was found on the loaded surface after 100 shots at 0.6 GW/m^2 for a pulse duration of 1 ms. Besides, the melting and recrystallization behaviors of deformed $\text{W-Y}_2\text{O}_3$ were less obvious than those of SPSed $\text{W-Y}_2\text{O}_3$ [34]. The discrepancy in thermal shock response between the two materials and in particular the superiority of deformed $\text{W-Y}_2\text{O}_3$ agrees well with the results that the better the thermophysical and mechanical properties, the better the thermal shock resistances. The high-energy-rate forging may significantly improve mechanical properties of $\text{W-Y}_2\text{O}_3$ materials [35]. It is indicated that needlelike grains ranging from a few to more than 50 μm in forged $\text{W-Y}_2\text{O}_3$ lead to the improved mechanical properties [35]. A detectable plastic deformation (TE = 2.9%) associated with work hardening occurs at 100°C, and the ultimate tensile strength of this forged $\text{W-Y}_2\text{O}_3$ material increases drastically to 1040 MPa.

For swaging deformed $\text{W-Y}_2\text{O}_3$, tungsten grains are round bar in shape [38]. The average diameter and length of tungsten grain in swaged $\text{W-Y}_2\text{O}_3$ are 4.6 and 26.7 μm , respectively, corresponding to an aspect ratio of about 6:1. The tensile results have shown that it is a brittle fracture until above 250°C and its strength is also smaller than that of the high-energy-rate forging ones [35], which implies that bimodal interfaces (in forged ones) are more in favor of strengthening and ductility. Therefore, it is important to notice that again the microstructure design, here from hot forging, is at least as important as the ODS effect. Although the addition of Y_2O_3 can produce PB interfaces and control GB interfaces, it cannot reduce the detrimental impurities of oxygen. Xie et al. [21] added Zr element into $\text{W-Y}_2\text{O}_3$ to absorb free oxygen at GBs to form Y-Zr-O particles, and at the same time, the particle size of Y-Zr-O can be further reduced. Because of the improved PB/GB interfaces by Zr, the strength and plasticity of this $\text{W-Zr-Y}_2\text{O}_3$ increase further on the base of $\text{W-Y}_2\text{O}_3$.

3. Carbide dispersion-strengthened tungsten-based materials

As compared with the oxides' strengthening phases, the carbides, such as TiC, ZrC, and HfC, have much higher melting temperatures and better compatibility with tungsten, which may lead to excellent comprehensive performance. Kurishita et al. reported ultrafine-grained (UFG) W-TiC alloys which showed increased

mechanical properties and better irradiation resistance [22, 39, 40]. These favorable properties of W-TiC alloys imply the potential of other carbide dispersion-strengthened tungsten materials with fine microstructures.

Among these carbide-strengthened phases, ZrC and TaC have high melting temperatures of 3540°C and 3900°C, respectively. It's worth mentioning that the lattice match of $d_{(200)\text{ZrC}} \approx d_{(110)\text{W}} \approx 0.221$ nm might introduce coherent PB interface between ZrC phase and W matrix, which will significantly increase PB cohesion. In addition, ZrC as an oxygen getter can react with oxygen to form stable Zr-C-O or ZrO₂ particles at GBs, purifying GB interface, and thus is beneficial to improve the GB cohesion and enhance the low-temperature ductility of tungsten.

Fan et al. [27, 41] fabricated W-ZrC material by high-temperature sintering in hydrogen atmosphere using W-ZrC composite powders prepared by sol-heterogeneous precipitation-spray drying-thermal reduction. The relative density of their W-(0, 1, 2, 3, 4)%ZrC samples is in the range of 98.5–99.7%. They found that the addition of ZrC could refine tungsten grains and improve the strength. The grain size of W-3%ZrC (10~15 μm) is much smaller than that of pure W (~100 μm), and the ZrC particles are micron-sized; most of them are distributed at grain boundaries. Xie et al. [42, 43] fabricated a series of W-(0, 0.2, 0.5, 1.0)%wtZrC with an average grain size which ranges from 2.7 to 4.2 μm by using mechanical alloy and SPS. The ultimate tensile strengths (UTS) of SPS pure W and W-(0.2, 0.5, 1.0)%ZrC at 700°C are 337, 419, 535 and 749 MPa, respectively, suggesting enhancements in strength by adding a small amount of ZrC nanoparticles. The strength of W-0.5%ZrC (W-0.5ZrC) is over 50% higher than that of pure W. Meanwhile, the ductility could also be effectively improved by the ZrC addition.

On the basis of composition optimization, Xie et al. [28] fabricated bulk W-0.5wt%ZrC plates with a thickness of 8.5 mm, which are suitable for engineering application. This material exhibits very good mechanical properties. At RT, this bulk W-0.5ZrC plate exhibits a high bending stress of 2.5 GPa as well as a flexural strain of 3%, which is much higher than those of the hot rolled W, HIPed pure W [44], and W-1.0Y₂O₃ [45] and close to those of the severely deformed W-TiC alloys [46]. The DBTT is about 100°C (see **Figure 1** and **Table 1**), which is much lower than that of reported bulk W alloys and several other tungsten materials [31, 47]. At temperatures above 150°C, the W-0.5ZrC plates can be bent to a high flexural strain of 15% (limited by the machine) without any crack.

Figure 1e shows the engineering stress-strain curves of the W-0.5ZrC alloy tested at various temperatures along rolling direction (RD). At 100°C, the W-0.5ZrC plate exhibits obvious tensile deformation with a TE~3% and an UTS value up to 1.1 GPa. With the increase of the test temperature to 200°C, the TE increases to 14.2%, and the UTS maintains as high as ~1 GPa. At a higher testing temperature of 500°C, the UTS is still very high (583 MPa), and the TE increases up to 41%. The rolled W-0.5ZrC showed both higher strength and ductility than that of the rolled W-0.5TiC [48] and rolled W-0.5TaC [49], which were fabricated following a similar process. The W-3%Re and K-doped W-3%Re show ductility at 100°C, which is comparable with W-0.5ZrC plate, while their tensile strength values (<1000 MPa) are lower than that of W-0.5ZrC plate (1058 MPa) [50]. As compared with Plansee ITER specification W (IGP), AT&M ITER specification W (CEFTR), W-1wt%TiC (W1TiC), W-2wt%Y₂O₃ (W2YO) from Karlsruhe Institute of Technology at Germany, and fine-grained W (FG) from the Institute of Plasma Physics at Czech Republic, W-0.5ZrC exhibits the highest tensile strength and lower DBTT [51], as shown in **Figure 2**.

For PFCs, the transient heat load events such as major plasma disruptions, edge-localized modes (ELMs), and vertical displacement events (VDEs) are serious issues [11], which may lead to a significant temperature rise and high thermal

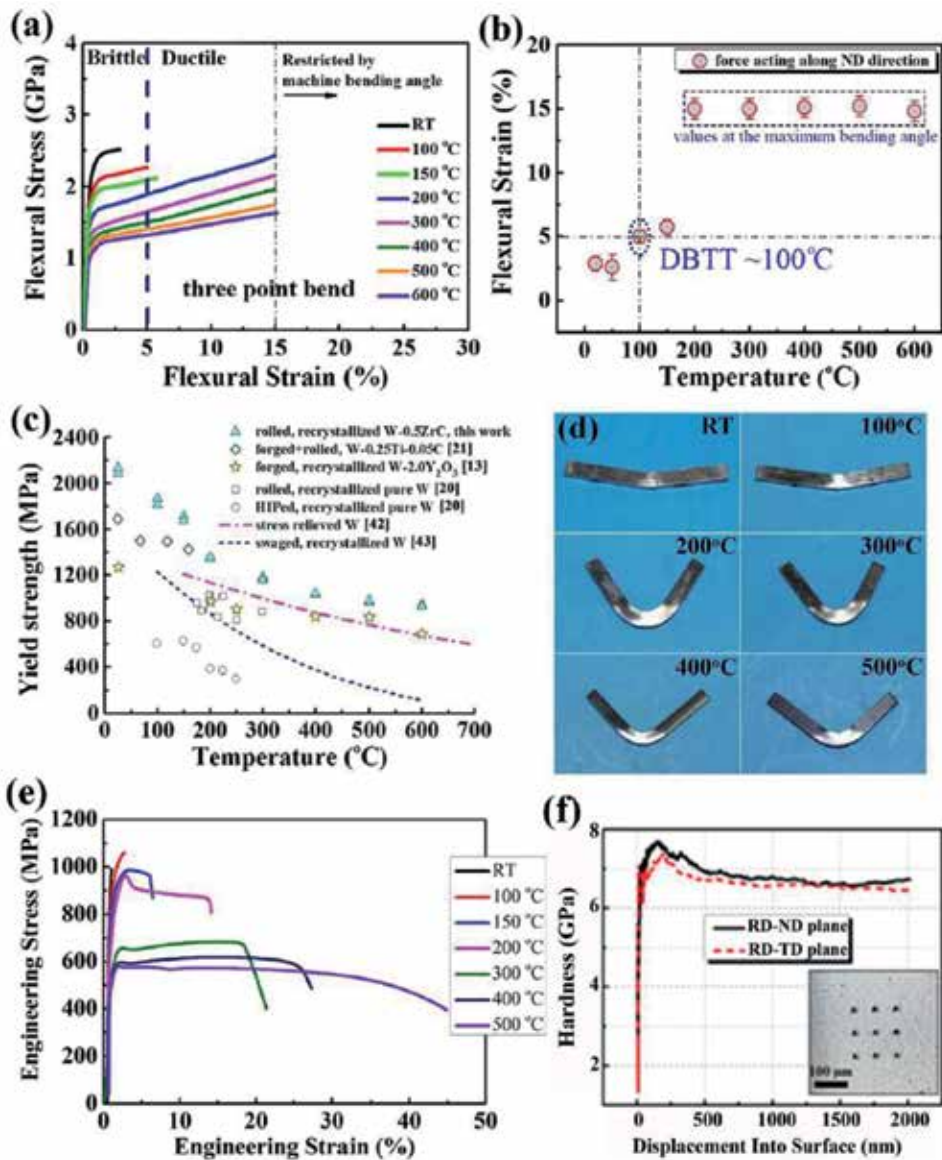


Figure 1. Mechanical properties of W-0.5ZrC alloy: (a) flexural stress-strain curves tested at various temperatures (note that values larger than a flexural strain of 15% is not accurate due to the limited bending angle of the machine). (b) Flexural strain of W-0.5ZrC at various test temperatures. (c) Temperature dependence of the yield strength (YS) by 3-point bending test in comparison with available literature data. (d) Optical images of 3-point bending specimens tested at various temperatures. (e) Tensile engineering stress-strain curves of W-0.5ZrC at different temperatures. (f) Hardness in different planes of W-0.5ZrC tested by nanoindenter [28].

stresses in PFCs. The abrupt high temperature during transient events can lead to material recrystallization, grain growth, surface melting, and droplet ejection. The high thermal stresses can lead to cracking, fatigue fracture, and fatal destruction of the PFCs. Therefore, the thermal shock resistance of PFCs is closely related to their mechanical properties. Intuitively, high strength could resist a relatively high stress induced by thermal shocks to prohibit the cracking formation, while good plasticity/ductility is in favor of releasing the stress via plastic deformation rather than cracking. That is to say, a higher strength and better low-temperature ductility would lead to the better thermal shock resistance [28, 31, 52].

Materials/size	Working process	DBTT (K)	Dimension (mm)	Methods
W-0.5ZrC (8.5 mm thick plate)	Rolling	373	2 × 2 × 20	3 PB
Pure W (0.1 mm thick foil)	Rolling + joining	373	4 × 15 × 33	Charpy
Pure W (10 mm thick plate)	Rolling	473	2 × 4 × 20	3 PB
Pure W (4 mm thick)	HIP	473	2 × 3.3 × 20	3 PB
Pure W	Injection molding	1173	3 × 4 × 27	Charpy
W-2Y ₂ O ₃ (2 mm thick, Φ 95 mm)	Hot forging	473	2 × 2 × 25	3 PB
W-1%Y ₂ O ₃	Injection molding	1273	3 × 4 × 27	Charpy
W-0.2Zr-1.0Y ₂ O ₃ (Φ 9 mm rod)	Swaging	423	2 × 3.3 × 20	3 PB
W-0.25Ti-0.05C (1 mm thick plate)	Rolling	260	1 × 1 × 20	3 PB
W-0.2TiC (1 mm thick)	Forging + rolling	440	1 × 1 × 20	3 PB
W-0.5TiC	HIP + forging	484	1 × 1 × 20	3 PB
WL10	Swaging + rolling	973	10 × 10 × 55	Charpy

Table 1.
DBTT of the rolled W-0.5ZrC and several reported W materials [31].

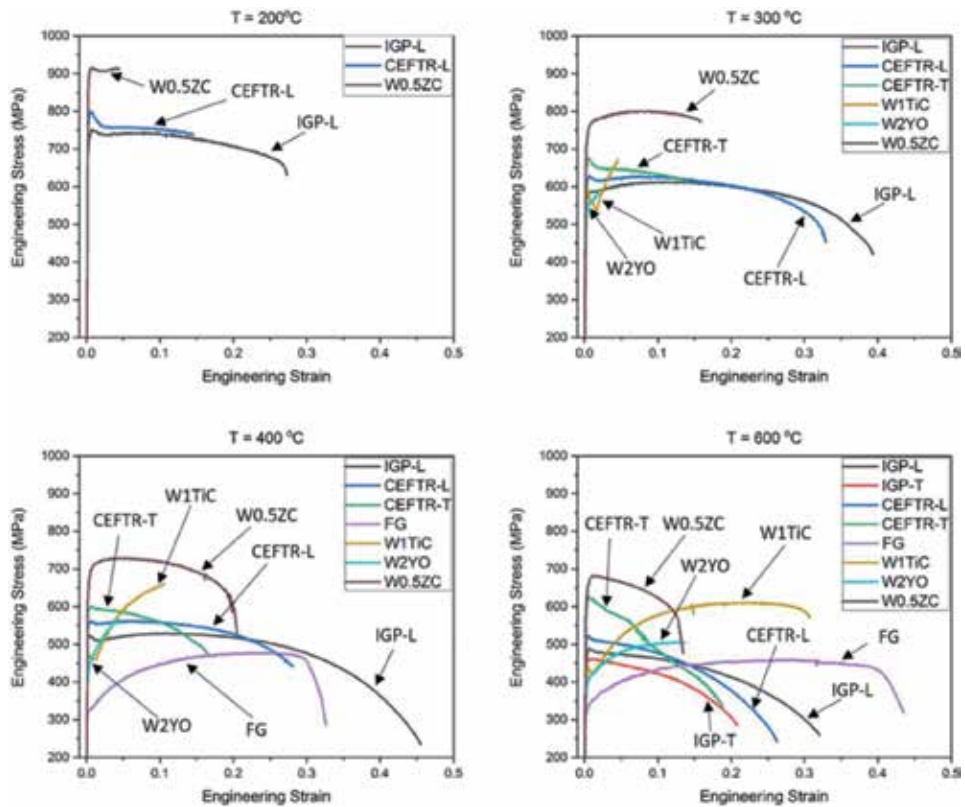


Figure 2.
The tensile stress of various W materials [51].

Figure 3 shows the thermally loaded surfaces of rolled W-0.5ZrC after exposure to single shot with a pulse length of 5 ms using an electron beam. No cracks or melting were observed on the samples when tested at an absorbed power

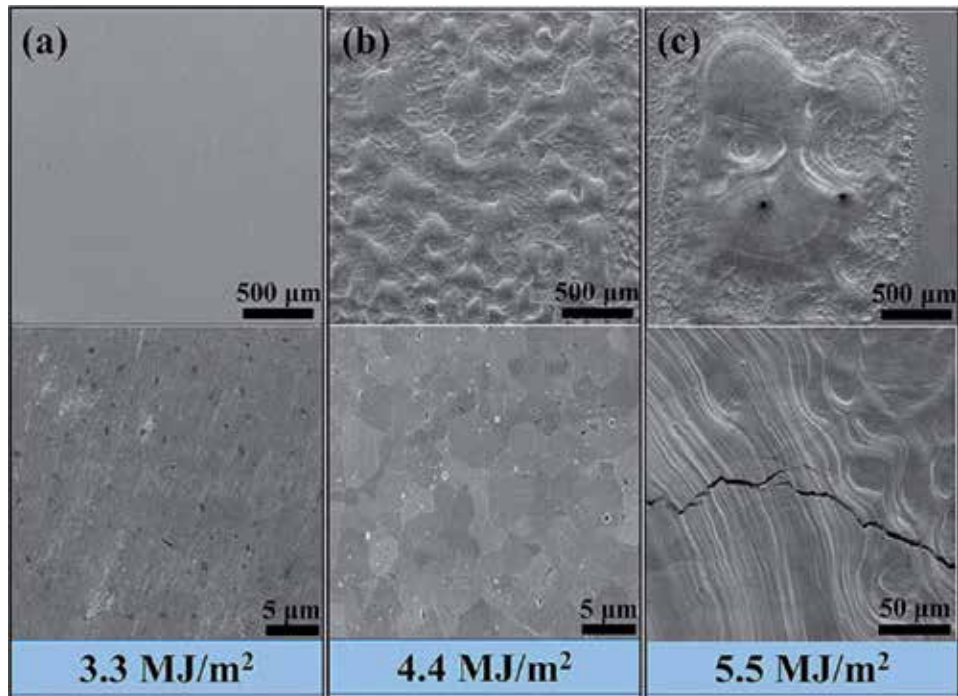


Figure 3.

The SEM images of sample surfaces after exposure to thermal shocks with a pulse duration of 5 ms. (a) 3.3 MJ/m² (0.66 GW/m²), (b) 4.4 MJ/m² (0.88 GW/m²), and (c) 5.5 MJ/m² (1.1 GW/m²) [28]. No cracks were found at 0.88 GW/m² although the sample surface melted and the cracking threshold is 0.88–1.1 GW/m².

density (APD) of 0.66 GW/m² as shown in **Figure 3a**. Still no crack at an APD of 0.88 GW/m² but surface melting was observed as shown in **Figure 3b**. The results suggest that the melting threshold of the rolled W-0.5ZrC is ~0.88 GW/m². When the APD increased to 1.1 GW/m² (**Figure 3c**), both cracks and melting were found on the sample surface, indicating a crack threshold of 0.88–1.1 GW/m². For comparison, the cracking thresholds of previously reported tungsten materials like sintered W, chemical vapor deposition (CVD) W, deformed W, potassium-doped W (W-K), and W-La₂O₃ alloys [53–57] were summarized in **Table 2**. These results further indicate the excellent thermal shock resistance of the rolled W-0.5ZrC.

During the thermal shock, the materials are heated and undergo thermal expansion, which is restricted by the colder surrounding material, causing compressive stress [53]. If the compressive stress exceeds the yield strength of the tested tungsten material, plastic deformation would occur because of the material plastic at high temperatures. During the cooling stage, the thermally loaded area shrinks, and the compressive stress is converted into a tensile stress [53]. Thus the cracks would form if the stress exceeds the ultimate tensile strength of the materials. Therefore, the excellent thermal shock resistance of the rolled W-0.5ZrC seems reasonable, because it has high strength, a lower DBTT, and good plasticity.

Thermal fatigue behaviors of the as-rolled and recrystallized W-0.5ZrC alloys were investigated by repetitive thermal shocks (100 shots in total) with a pulse duration of 1 ms at RT [14]. The cracking thresholds for the as-rolled and recrystallized W-0.5ZrC are 0.22–0.33 GW/m², which is comparable to that of ultrahigh-purity W but lower than that of W-5%Ta [52]. It's reported that at higher base temperatures, tungsten materials tend to exhibit enhanced resistance to thermal

Alloys	State	Crack thresholds (GW/m ²)
W-0.5ZrC	Swaged	0.22–0.44
W-0.5ZrC	Rolled	0.88–1.1
CVD W	—	0.28–0.33
W	As-sintered	0.33–0.55
W	Recrystallized	<0.33
Rolled W	As-rolled	0.44–0.66
Forged W	Stress relieved/ recrystallized	0.15–0.33
W-K alloy	Swaged + rolled	0.44–0.66
W-Y ₂ O ₃	—	0.6
WL10	Rolled	<0.22
W-TiC	—	0.33

Table 2.

Comparison of W-ZrC alloys and some tungsten materials after single thermal shock loads at RT with a pulse duration of 5 ms [31].

shocks because of the increased ductility of materials [13]. Nevertheless, there are still no results of the thermal fatigue behavior of the rolled W-0.5ZrC at higher base temperatures, which would be investigated in the near future.

The irradiation resistance to plasma is another key property for PFCs. The PFCs in fusion reactors suffer from the high-flux (about $10^{24} \text{ m}^{-2} \text{ s}^{-1}$) low-energy plasma irradiation, which would cause bubbles and erosion phenomena on the surface of PFCs, and lead to the degradation of performances. More badly, the excessive erosion dusts will extinguish the burning plasma. Therefore, the less the erosion, the better.

Liu et al. [58] studied the irradiation damage of several newly developed tungsten materials including pure tungsten, CVD-W, W-0.5ZrC, W-1.0wt.%Y₂O₃, W-1.0vol.%Y₂O₃, and W-1.0La₂O₃ under low-energy He plasma neutral beam. **Figure 4** shows the surface and cross-sectional morphologies of irradiation-modified layers on the abovementioned tungsten materials after high fluences (10^{26} ions/m^2) of low-energy helium plasma irradiation [58]. After 220 eV He-ion irradiation at 900°C, all samples showed pinhole features on the irradiated surface, while in the case of 620 eV He-ion irradiation at 1000°C, the pinhole surface evolved into coral-like features except for the W-0.5ZrC alloy which retains the pinhole feature [58]. This result indicates the good resistance of W-0.5ZrC alloy to He-ion irradiation. The fine-grained W-0.5ZrC alloy has abundant GBs and PBs which all provide nucleation sites for He atom aggregation and thus reduce the concentration of He, thus hindering the growth of He bubbles and mitigating the evolution from pinhole to coral-like structures. The thickness of modified layers on the surface of tungsten materials was measured and plotted in **Figure 5**, in which W-La, W-Y1, and W-Y2 represent W-1wt.%La₂O₃, W-1wt.%Y₂O₃, and W-1vol.%Y₂O₃, respectively. The thickness of modified layers on W-0.5ZrC is much lower than that of pure W, W-La, and W-Y1, implying its better resistance to plasma irradiation and erosion [58].

Liu et al. [58] also studied the evolution of morphology and thermal-mechanical properties of pure W, CVD-W, and W-0.5ZrC alloys after pure H beam and H/He mixed beam irradiation using the neutral beam facility GLADIS (Max Planck Institute for Plasma Physics, Germany). It is found that just roughness occurred on all W material surfaces after H irradiation, while a mixture of 6% He resulted in pinhole structures, indicating the crucial factor of He irradiation for the surface modification. The unexposed and pre-irradiated CVD-W and W-0.5ZrC were then

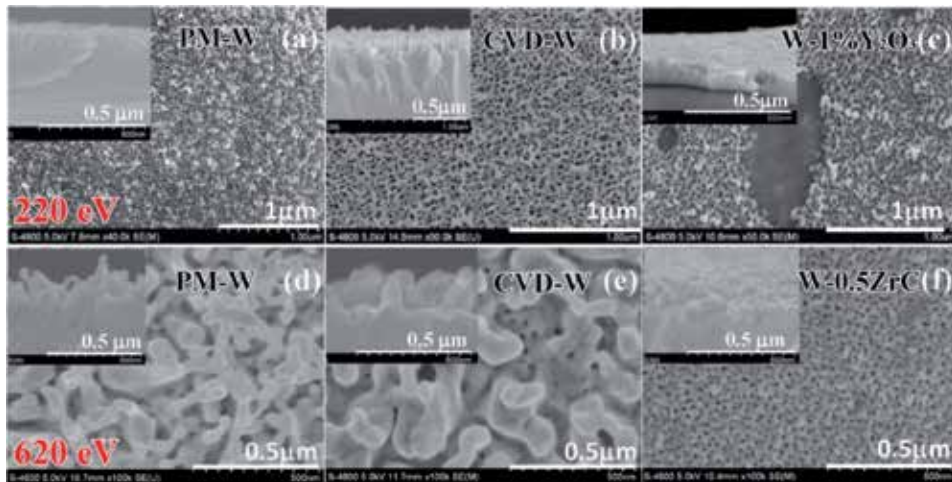


Figure 4. The surface morphologies of (a) pure W, (b) CVD-W, (c) W-1.0%Y₂O₃ irradiated by 220 eV He⁺ at about 900°C and (d) pure W, (e) CVD-W, and (f) W-0.5ZrC irradiated by 620 eV He⁺ at 1000°C to a same fluence of 1×10^{26} atoms/m² [58]. The insets of (a)–(f) show the corresponding cross-sectional morphologies of irradiation-modified layer in each sample.

loaded repeatedly by thermal shocks through an electron beam with a 1 ms pulse and 100 cycles. The cracking threshold of unexposed CVD-W is about ~ 0.22 GW/m², a little lower than that of W-0.5ZrC. Pre-irradiation by H only seems to have less effect on the critical cracking thresholds, while pre-irradiation by H/He mixed beam significantly reduces the cracking thresholds [58].

The effects of deuterium (D) plasma irradiation on the microstructure of W-ZrC were also investigated. Several CDS-W materials, including rolled W-0.5ZrC [28], W-0.5HfC [30], W-0.5TiC [48], as well as pure W, were subjected to D plasma irradiation in the linear plasma device of simulation for tokamak edge plasma (STEP) [59]. **Figure 6** shows the morphologies of these materials after exposing to D plasma irradiation under a same condition

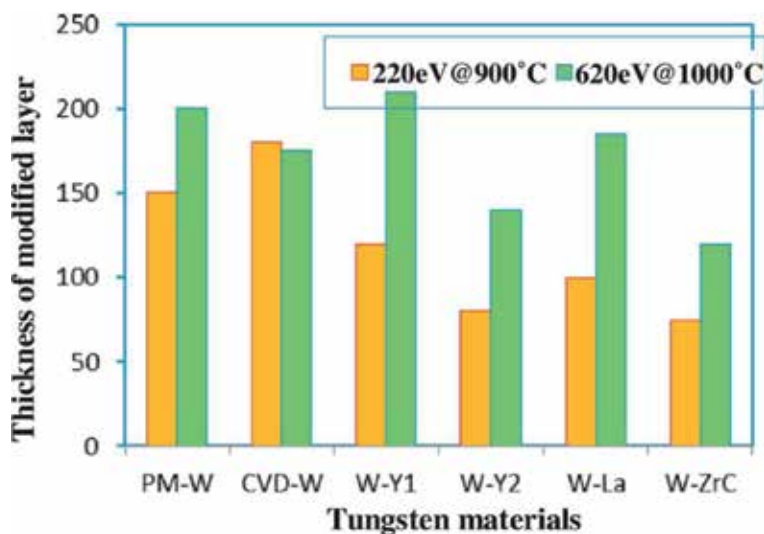


Figure 5. Thickness of modified layers in various tungsten materials under the He⁺ irradiation of 220 eV at 900°C and 620 eV at 1000°C [58].

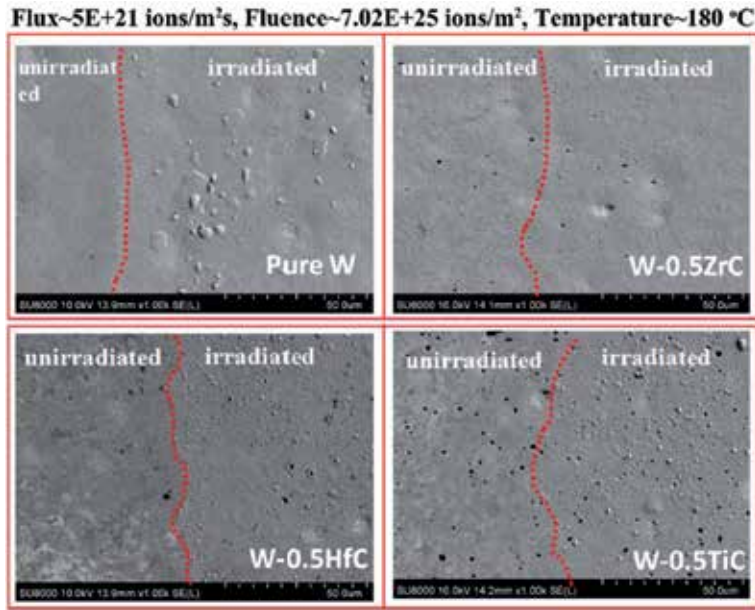


Figure 6. Surface morphologies of pure W, rolled W-0.5ZrC, W-0.5HfC, and W-0.5TiC irradiated by D plasma. [31].

(D⁺ energy ~90 eV, flux ~5 × 10²¹ ions/m² s, fluence~7.02 × 10²⁵ ions/m², temperature ~180°C) [31]. Surface swelling and a high density of large bubbles with size ranging from 1 to 10 μm were found on the surface of the pure W. On the surface of W-0.5HfC and W-0.5TiC, the bubble size was much smaller (less than 1 μm). In the case of W-0.5ZrC, only blisters (about 100 nm) were observed, despite the high blister density. These results further indicate the increased resistance to bubble formation to D plasma irradiation. The enhanced irradiation resistance may come from the fine grains and homogeneously dispersed nanoscaled particles in the rolled W-0.5ZrC, which provide a large number of GB and PB interfaces that act as effective sinks for irradiation-induced defects [60–62].

The hydrogen isotopes especially tritium retention behaviors in PFCs are also an important issue, which has an impact on the tritium fueling and the safety of fusion reactors and has not been completely understood. The hydrogen isotope retention behaviors of W-ZrC alloy were investigated through plasma irradiation and thermal desorption spectrum (TDS) analysis. The D plasma irradiation was carried out in the STEP device [59]. Rolled pure W and W-0.5ZrC were exposed to low-energy high-flux deuterium plasma under the same condition (D⁺ energy~90 eV, flux ~5 × 10²¹ ions/m² s, fluence~7.02 × 10²⁵ ions/m², temperature 400 K). After irradiation, the TDS results have shown that the rolled W-0.5ZrC exhibits much lower hydrogen retention than that of pure W as shown in **Figure 7**. This result indicates that the hydrogen retention in W-ZrC is not increased although they contain the Zr element, because the Zr element exists in the form of stable carbide or oxide particles. Both the rolled W-0.5ZrC and pure W had a desorption peak at temperature around 560°C, and the peak intensity of W-0.5ZrC is much lower than that of pure W.

The above performance is closely related to the microstructure of the rolled W-0.5ZrC. The detailed microstructures show the coexistence of multi-scale interfaces in the rolled W-0.5ZrC plate. From the outer to inner space, in the first layer along the rolling direction, the average length of mother grains is about

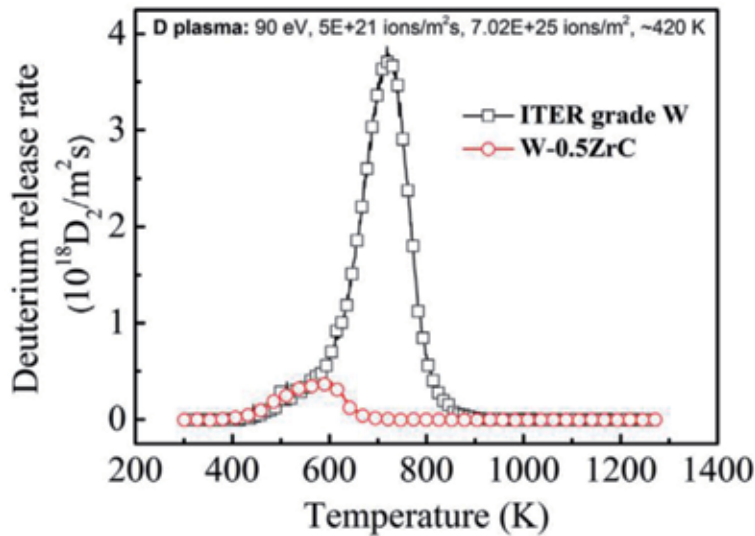


Figure 7. TDS results of pure W and W-0.5ZrC after 90 eV high-flux ($\sim 5 \times 10^{21}$ ions/m² s) D plasma irradiation to a fluence of 7.02×10^{25} ions/m² at 400 K [31].

10 μm , and the width is about 1–3 μm , which is the micrometer scale GB interface [28]. Prolonged mother grains come from the multistep rolling deformation. In the second layer, there are equiaxed sub-grains in the matrix with average size of about 1 μm , which could be considered to the sub-micrometer scale GB interfaces. The sub-grains can be attributed to the deformation and dynamic recrystallization resulting from the precise control of rolling parameters [28]. For the third layer, most of the nanoscaled particles disperse in tungsten grain interior. The size distributions of the particles indicate that most particles located in W grains have an average size of 51 nm, while parts of particles at W GBs show bimodal distribution which contains relatively small particles with an average particle size of 60 nm ranging from 40 to 200 nm and a small fraction of large particles with an average particle size of 385 nm ranging from 250 to 400 nm [28]. It is worth pointing out that the small particles at GBs are dominantly ZrC, while the large particles are W-Zr-C-O complexes, which eliminate the free O at GBs and purifying GB interfaces. Therefore, the third layer interface is the nanoscale or sub-micrometer scale interface. The intuitive magnifying HRTEM of PBs shown in **Figure 8a–e** exhibits a perfect coherent structure interface between W matrix and ZrC dispersoids. This atomic ordered interface could pin and accumulate dislocations and thus effectively raise the strength and simultaneously improve the ductility of alloys.

The multi-scaled interface structure is in favor of irradiation resistance and decreases the retention of hydrogen. Mother grain boundaries may provide rapid diffusion paths for H and its isotope [63], and thus H could easily diffuse to the surface of the specimen even at a relatively low temperature. Thus a large fraction of D atoms may escape from the W-0.5ZrC during the D plasma irradiation at 400 K, leading to low retention of D in materials. At the same time, the fine sub-grains increase the GB interface density, and the nanosized particles create a high density of PB interfaces, which can absorb interstitial defects and then annihilate nearby vacancies by re-emitting the interstitial atoms back into the grain, thus improving the ability of irradiation resistance of W-0.5ZrC alloy.

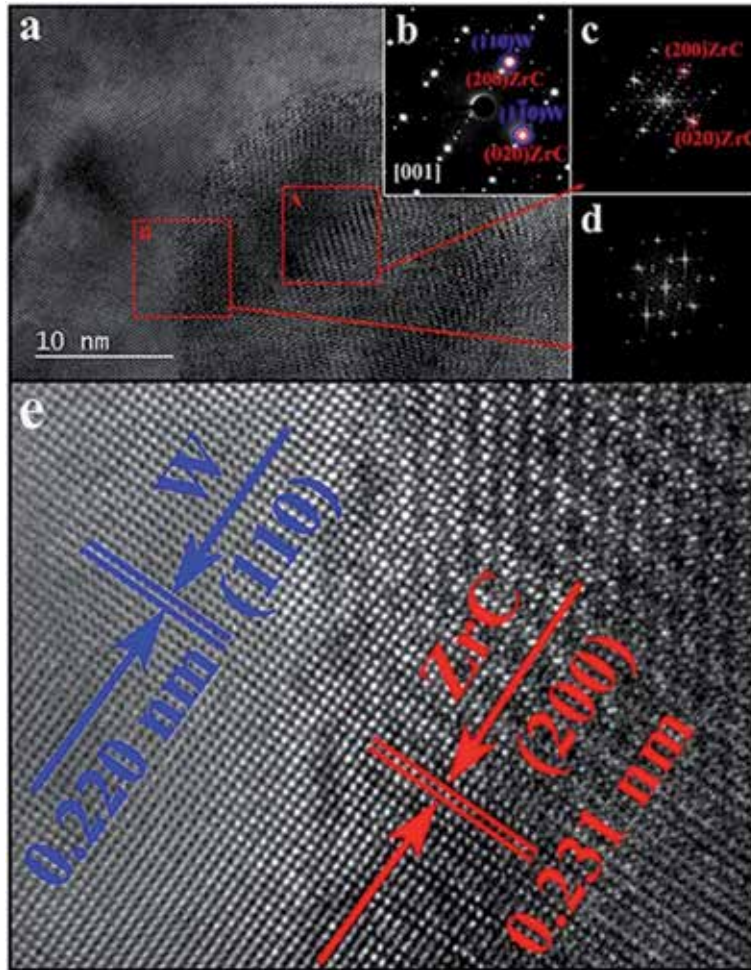


Figure 8. (a) HRTEM image of W matrix and ZrC phase (intragranular) as viewed along [001]. (b) The SAEDP revealing the particle with a face-centered cubic structure. (c) Fast Fourier transform (FFT) pattern of selected red square area A on ZrC. (d) FFT pattern of selected red square area B at interface area between W and ZrC. (e) It is clear that the particle-matrix phase boundaries have a coherent structure like that shown in high magnification [28].

4. W fiber-reinforced W_f/W composites

Since a decade, a promising method of toughening tungsten composites using tungsten fiber reinforcement has been actively pursued, namely, tungsten fiber-reinforced tungsten (W_f/W) composites [64–72]. However, in the bare W_f/W , the interface is not obvious due to the chemical reaction between W_f and W matrices, so the reinforcing effect is not ideal. Therefore, in this material concept, tungsten fibers are embedded in a tungsten matrix where a proper interface has to be introduced to prevent a chemical reaction between the two components. The increase in toughness is achieved through a couple of non-plastic energy dissipation mechanisms such as matrix cracking and interfacial debonding followed by frictional sliding/pullout of the fibers, while the primary crack is bridged by mostly elastically deforming fibers [65, 73]. To maximize the energy dissipation, the interfaces need to be engineered by coating which can withstand thermal exposure during service. Du et al. [65] investigate the thermal stability of the various kinds of coated interfaces for W_f/W composites: Cu/W multilayer, Er/W multilayer, ZrO_x/W bilayer, ZrO_x/Zr multilayer,

and C/W dual layer. These coatings were selected for interface engineering with which one utilizes energy dissipation by controlled interfacial debonding and sliding achieving apparent toughness. Regarding the effect on the interfacial properties, the fracture energy of the Er/W multilayer and the ZrO_x/Zr multilayer was affected by less than 10%, while it increased by 40% for the ZrO_x/W bilayer. Therefore, the ZrO_x/W bilayer interface is the best choice for W_f/W composite. The single direction of W fibers can enhance the fracture energy of tungsten matrix once the extrinsic toughening mechanisms of fiber pullout and plastic deformation were triggered, but they will lead to the obvious anisotropy of mechanical properties [73]. Lama et al. [74] use woven tungsten wire meshes as reinforcement in the composites (wire diameter, 127 μm ; distance between wires, 1 mm), which avoided the anisotropy induced by single direction of W fibers. In addition, a stable interfacial coating zirconia film (ZrO_x) was deposited on the meshes by magnetron sputtering. The zirconia coating could survive the heat loads without any notable damage or overall cracking. The coating thickness remained mostly unchanged. Therefore, under the extreme environment, the zirconia coating interfaces are stable, which is in favor of reinforcing the W_f/W composites [75, 76].

5. Summary and outlook

The improvements in different aspects of tungsten have been enriching the knowledge base and help to show the way to high-performance tungsten materials for fusion applications. Nevertheless, to satisfy the requirements of PFCs in future fusion facilities, the performances of tungsten materials need to be further improved, which may be achieved through several approaches as follows. Firstly, microstructure optimization includes the size and shape of tungsten grains and the size, distribution, and the number density of second-phase particles in tungsten-based materials. For ODS-W or CDS-W, the size of strengthening particles is not small enough; if second-phase particles could be further refined, e.g., to 10 nm or even smaller, more favorable particle-matrix interfaces would be constructed, and thus mechanical properties, resistance to thermal loads, and irradiation might be further improved. Secondly, to reduce the DBTT and improve the low-temperature ductility, the content of detrimental interstitial impurities (i.e., O, N) should be as low as possible. For the W_f/W composites, the interface is still a weak point and needs to be further optimized.

For the materials used in fusion reactors, the synergistic effects of multi-loadings including high thermal loads, high-flux H/He plasma etching, and neutron irradiation may lead to much more severe degradation of properties. Therefore, the synergistic effects of high heat loads, low-energy high-flux plasma etching and neutron irradiation, and transmutation elements on the microstructures and properties of tungsten materials need to be systematically investigated in the near future, which is necessary to evaluate the performance of the tungsten materials more accurately, and the corresponding database for the performance of tungsten materials should be established.

Acknowledgements

This work was financially supported by the National Natural Science Foundation of China (Grant Nos.: 51771184, 11735015, 11575241, 51801203), the Natural Science Foundation of Anhui Province (Grant No. 1808085QE132), and the Open Project of State Key Laboratory of Environmental Friendly Energy Materials. We thank for the support of Professor Guang-Hong Lu in BeiHang University, Professor Dongping Liu in Dalian Nationalities University, and Professor Xiang Liu in the Southwest Institute of Physics.

Author details

Tao Zhang^{1*}, Zhuoming Xie², Changsong Liu² and Ying Xiong³

1 School of Physics and Electronic Engineering, GuangZhou University, GuangZhou, China

2 Institute of Solid State Physics, Chinese Academy of Sciences, Hefei, China

3 State Key Laboratory of Environment-Friendly Energy Materials, Southwest University of Science and Technology, Mianyang, China

*Address all correspondence to: zhangtao@issp.ac.cn

IntechOpen

© 2019 The Author(s). Licensee IntechOpen. This chapter is distributed under the terms of the Creative Commons Attribution License (<http://creativecommons.org/licenses/by/3.0>), which permits unrestricted use, distribution, and reproduction in any medium, provided the original work is properly cited. 

References

- [1] Knaster J, Moeslang A, Muroga T. Materials research for fusion. *Nature Physics*. 2016;**12**:424-434
- [2] Raffray AR, Nygren R, Whyte DG, et al. High heat flux components—Readiness to proceed from near term fusion systems to power plants. *Fusion Engineering and Design*. 2010;**85**:93-108
- [3] Rieth M, Dudarev SL, de Vicente SMG, et al. Recent progress in research on tungsten materials for nuclear fusion applications in Europe. *Journal of Nuclear Materials*. 2013;**432**:482-500
- [4] Linsmeier C, Rieth M, Aktaa J, et al. Development of advanced high heat flux and plasma-facing materials. *Nuclear Fusion*. 2017;**57**:092007
- [5] Bolt H, Barabash V, Krauss W, Linke J, Neu R, Suzuki S, et al. Materials for the plasma-facing components of fusion reactors. *Journal of Nuclear Materials*. 2004;**329**:66-73
- [6] Smid I, Pacher HD, Vieider G, Mszanowski U, Igitkhanov Y, Janeschitz G, et al. Lifetime of Be-, CFC-and W-armoured ITER divertor plates. *Journal of Nuclear Materials*. 1996;**233**:701-707
- [7] Kurishita H, Arakawa H, Matsuo S, et al. Development of nanostructured tungsten based materials resistant to recrystallization and/or radiation induced embrittlement. *Materials Transactions*. 2013;**54**:456-465
- [8] Norajitra P, Boccaccini LV, Gervash A, et al. Development of a helium-cooled divertor: Material choice and technological studies. *Journal of Nuclear Materials*. 2007;**367**:1416-1421
- [9] Wurster S, Baluc N, Battabyal M, et al. Recent progress in R&D on tungsten alloys for divertor structural and plasma facing materials. *Journal of Nuclear Materials*. 2013;**442**:S181-S189
- [10] Byun TS, Li M, Cockeram BV, Snead LL. Deformation and fracture properties in neutron irradiated pure Mo and Mo alloys. *Journal of Nuclear Materials*. 2008;**376**:240-246
- [11] Garkusha IE, Landman I, Linke J, Makhraj VA, Medvedev AV, Malykhin SV, et al. Performance of deformed tungsten under ELM-like plasma exposures in QSPA Kh-50. *Journal of Nuclear Materials*. 2011;**415**:S65-S69
- [12] Linke J, Loewenhoff T, Massaut V, Pintsuk G, Ritz G, Rodig M, et al. Performance of different tungsten grades under transient thermal loads. *Nuclear Fusion*. 2011;**51**(7):073017
- [13] Liu X, Lian YY, Chen L, Chen ZK, Chen JM, Duan XR, et al. Experimental and numerical simulations of ELM-like transient damage behaviors to different grade tungsten and tungsten alloys. *Journal of Nuclear Materials*. 2015;**463**:166-169
- [14] Xie ZM, Miao S, Liu R, Zeng LF, Zhang T, Fang QF, et al. Experimental and numerical simulations of ELM-like transient damage behaviors to different grade tungsten and tungsten alloys. *Journal of Nuclear Materials*. 2017;**496**:41-53
- [15] Kurishita H, Matsuo S, Arakawa H, et al. Current status of nanostructured tungsten-based materials development. *Physica Scripta*. 2014;**T159**:014032
- [16] Liu R, Xie ZM, Zhang T, Fang QF, Wang XP, Hao T, et al. Mechanical properties and microstructures of W-1% Y₂O₃ microalloyed with Zr. *Materials Science and Engineering: A*. 2016;**660**:19-23
- [17] Aguirre MV, Martin A, Pastor JY, Llorca J, Monge MA, Pareja R. Mechanical Behavior of W-Y₂O₃ and W-Ti Alloys from

25°C to 1000°C. Metallurgical and Materials Transactions A: Physical Metallurgy and Materials Science. 2009;**40**(10):2283-2290

[18] Song GM, Wang YJ, Zhou Y. Thermomechanical properties of TiC particle-reinforced tungsten composites for high temperature applications. International Journal of Refractory Metals and Hard Materials. 2003;**21**:1-12

[19] Xie ZM, Liu R, Fang QF, Zhou Y, Wang XP, Liu CS. Spark plasma sintering and mechanical properties of zirconium micro-alloyed tungsten. Journal of Nuclear Materials. 2014;**444**:175-180

[20] Liu R, Xie ZM, Hao T, Zhou Y, Wang XP, Fang QF, et al. Fabricating high performance tungsten alloys through zirconium micro-alloying and nano-sized yttria dispersion strengthening. Journal of Nuclear Materials. 2014;**451**:35-39

[21] Xie ZM, Liu R, Zhang T, Fang QF, Liu CS, Liu X, et al. Achieving high strength/ductility in bulk W-Zr-Y₂O₃ alloy plate with hybrid microstructure. Materials and Design. 2016;**107**:144-152

[22] Kurishita H, Amano Y, Kobayashi S, Nakai K, Arakawa H, Hiraoka Y, et al. Development of ultra-fine grained W-TiC and their mechanical properties for fusion applications. Journal of Nuclear Materials. 2007;**367**:1453-1457

[23] Kurishita H, Matsuo S, Arakawa H, Sakamoto T, Kobayashi S, Nakai K, et al. Development of re-crystallized W-1.1% TiC with enhanced room-temperature ductility and radiation performance. Journal of Nuclear Materials. 2010;**398**:87-92

[24] Rieth M, Dafferner B. Limitations of W and W-1% La₂O₃ for use as structural materials. Journal of Nuclear Materials. 2005;**342**:20-25

[25] Yar MA, Wahlberg S, Bergqvist H, Salem HG, Johnsson M, Muhammed M. Spark plasma sintering of tungsten-yttrium oxide composites from chemically synthesized nanopowders and microstructural characterization. Journal of Nuclear Materials. 2011;**412**:227-232

[26] Yar MA, Wahlberg S, Bergqvist H, Salem HG, Johnsson M, Muhammed M. Chemically produced nanostructured ODS-lanthanum oxide-tungsten composites sintered by spark plasma. Journal of Nuclear Materials. 2011;**408**:129-135

[27] Fan JL, Han Y, Li PF, Sun ZY, Zhou Q. Micro/nano composited tungsten material and its high thermal loading behavior. Journal of Nuclear Materials. 2014;**455**:717-723

[28] Xie ZM, Liu R, Miao S, Yang XD, Zhang T, Wang XP, et al. Extraordinary high ductility/strength of the interface designed bulk W-ZrC alloy plate at relatively low temperature. Scientific Reports. 2015;**5**:16014

[29] Lee D, Umer MA, Ryu HJ, Hong SH. The effect of HfC content on mechanical properties HfC-W composites. International Journal of Refractory Metals and Hard Materials. 2014;**44**:49-53

[30] Wang YK, Miao S, Xie ZM, Liu R, Zhang T, Fang QF, et al. Thermal stability and mechanical properties of HfC dispersion strengthened W alloys as plasma-facing components in fusion devices. Journal of Nuclear Materials. 2017;**492**:260-268

[31] Liu R, Xie ZM, Yao X, Zhang T, Wang XP, Hao T, et al. Recent progress on the R&D of W-ZrC alloys for plasma facing components in fusion devices. Nuclear Materials and Energy. 2018;**16**:191-206

[32] Veleva L, Oksiuta Z, Vogt U, et al. Sintering and characterization

of W–Y and W–Y₂O₃ materials.
Fusion Engineering and Design.
2009;**84**(7-11):1920-1924

[33] Liu R, Zhou Y, Hao T, Zhang T, Wang XP, Liu CS, et al. Microwave synthesis and properties of fine-grained oxides dispersion strengthened tungsten. *Journal of Nuclear Materials*. 2012;**424**:171-175

[34] Zhao MY, Zhou ZG, Zhong M, Tan J, Lian YY, Liu X. Thermal shock behavior of fine grained W–Y₂O₃ materials fabricated via two different manufacturing technologies. *Journal of Nuclear Materials*. 2016;**470**:236

[35] Lian YY, Liu X, Feng F, Song JP, Yan BY, Wang YM, et al. Mechanical properties and thermal shock performance of W–Y₂O₃ composite prepared by high-energy-rate forging. *Physica Scripta*. 2017;**T170**:014044

[36] Battabyal M, Schblin R, Spatig P, Baluc N. W–2wt.%Y₂O₃ composite: Microstructure and mechanical properties. *Materials Science and Engineering A*. 2012;**538**:53

[37] Veleva L, Schaeublin R, Battabyal M, Plociski T, Baluc N. Investigation of microstructure and mechanical properties of W–Y and W–Y₂O₃ materials fabricated by powder metallurgy method. *International Journal of Refractory Metals and Hard Materials*. 2015;**50**:210-216

[38] Xie ZM, Liu R, Miao S, Zhang T, Wang XP, Fang QF, et al. Effect of high temperature swaging and annealing on the mechanical properties and thermal conductivity of W–Y₂O₃. *Journal of Nuclear Materials*. 2015;**464**:193-199

[39] Pintsuk G, Kurishita H, Linke J, Arakawa H, Matsuo S, Sakamoto T, et al. Thermal shock response of fine-and ultra-fine-grained tungsten-based materials. *Physica Scripta*. 2011;**T145**:014060

[40] Kurishita H, Kobayashi S, Nakai K, Ogawa T, Hasegawa A, Abe K, et al. Development of ultra-fine grained W–(0.25-0.8) wt% TiC and its superior resistance to neutron and 3 MeV He-ion irradiations. *Journal of Nuclear Materials*. 2008;**377**:34-40

[41] Li PF, Fan JL, Han Y, et al. Microstructure evolution and properties of tungsten reinforced by additions of ZrC. *Rare Metal Materials and Engineering*. 2018;**47**(6):1695-1699

[42] Xie ZM, Zhang T, Liu R, Fang QF, Miao S, Wang XP, et al. Grain growth behavior and mechanical properties of zirconium micro-alloyed and nano-size zirconium carbide dispersion strengthened tungsten alloys. *International Journal of Refractory Metals and Hard Materials*. 2015;**51**:180-187

[43] Liu R, Xie ZM, Yao X, Zhang T, Wang XP, Hao T, et al. Effects of swaging and annealing on the microstructure and mechanical properties of ZrC dispersion-strengthened tungsten. *International Journal of Refractory Metals & Hard Materials*. 2018;**76**:33-40

[44] Krsjak V, Wei SH, Antusch S, Dai Y. Mechanical properties of tungsten in the transition temperature range. *Journal of Nuclear Materials*. 2014;**450**:81-87

[45] Zhao M, Zhou Z, Zhong M, Tan J. Effect of hot rolling on the microstructure and fracture behavior of a bulk fine-grained W–Y₂O₃ alloy. *Materials Science and Engineering: A*. 2015;**646**:19-24

[46] Ishijima Y, Kannari S, Kurishita H, Hasegawa M, Hiraoka Y, Takida T, et al. Processing of fine-grained W materials without detrimental phases and their mechanical properties at 200–432 K. *Materials Science and Engineering: A*. 2008;**473**:7-15

- [47] Guo HY, Xia M, Chan LC, Wang K, Zhang X-X, Yan Q-Z, et al. Nanostructured laminar tungsten alloy with improved ductility by surface mechanical attrition treatment. *Scientific Reports*. 2017;**7**:1351
- [48] Miao S, Xie ZM, Zhang T, Wang XP, Fang QF, Liu CS, et al. Mechanical properties and thermal stability of rolled W-0.5 wt% TiC alloys. *Materials Science and Engineering: A*. 2016;**671**:87-95
- [49] Miao S, Xie ZM, Yang XD, Liu R, Gao R, Zhang T, et al. *International Journal of Refractory Metals and Hard Materials*. 2016;**56**:8-17
- [50] Fukuda M, Nogami S, Hasegawa A, et al. Tensile properties of K-doped W-3% Re. *Fusion Engineering and Design*. 2014;**89**(7-8):1033-1036
- [51] Yin C, Bakaeva A, Terentyev D, Petrov R, Pardoën T, Antush S, et al. Tensile properties of baseline and advanced tungsten grades for fusion applications. *International Journal of Refractory Metals and Hard Materials*. 2018;**75**:153
- [52] Wirtz M, Linke J, Loewenhoff T, Pintsuk G, Uytendhouwen I. Transient heat load challenges for plasma-facing materials during long-term operation. *Nuclear Materials and Energy*. 2017;**12**:148-155
- [53] Lian YY, Liu X, Cheng ZK, Wang J, Song JP, Yu Y, et al. Thermal shock performance of CVD tungsten coating at elevated temperatures. *Journal of Nuclear Materials*. 2014;**455**:371-375
- [54] Uytendhouwen I, Decreton M, Hirai T, Linke J, Pintsuk G, Van Oost G. Influence of recrystallization on thermal shock resistance of various tungsten grades. *Journal of Nuclear Materials*. 2007;**363**:1099-1103
- [55] Zhang XX, Yan QZ. The thermal crack characteristics of rolled tungsten in different orientations. *Journal of Nuclear Materials*. 2014;**444**:428-434
- [56] Huang B, Tang J, Chen LQ, Yang XL, Lian YY, Chen L, et al. Design of highly thermal-shock resistant tungsten alloys with nanoscaled intra- and inter-type K bubbles. *Journal of Alloys and Compounds*. 2019;**782**:149-159
- [57] Zhang XX, Yan QZ, Lang ST, Xia M, Liu X, Ge CC. Thermal shock and fatigue resistance of tungsten materials under transient heat loading. *Journal of Nuclear Materials*. 2014;**455**:537-543
- [58] Liu X, Lian YY, Greuner H, Boeswirth B, Jin YZ, Feng F, et al. Irradiation effects of hydrogen and helium plasma on different grade tungsten materials. *Nuclear Materials and Energy*. 2017;**12**:1314-1318
- [59] Lu GH, Cheng L, Arshad K, Yuan Y, Wang J, Qin SY, et al. Development and optimization of STEP—a linear plasma device for plasma-material interaction studies. *Fusion Science and Technology*. 2017;**71**:177-186
- [60] Ackland G. Controlling radiation damage. *Science*. 2010;**327**:1587-1588
- [61] Zinkle SJ, Snead LL. Designing radiation resistance in materials for fusion energy. *Annual Review of Materials Research*. 2014;**44**:241-267
- [62] Bai XM, Voter AF, Hoagland RG, Nastasi M, Uberuaga BP. Efficient annealing of radiation damage near grain boundaries via interstitial emission. *Science*. 2010;**327**:1631-1634
- [63] Iwaoka H, Arita M, Horita Z. Hydrogen diffusion in ultrafine-grained palladium: Roles of dislocations and grain boundaries. *Acta Materialia*. 2016;**107**:168-177
- [64] Du J, Höschel T, You JH. Feasibility study of a tungsten wire-reinforced

tungsten matrix composite with ZrOx interfacial coatings. *Composites Science and Technology*. 2010;**70**:1482-1489

[65] Du J, You JH, Höschel T. Thermal stability of the engineered interfaces in Wf/W composites. *Journal of Materials Science*. 2012;**47**:4706-4715

[66] Riesch J, Buffière J-Y, You JH, et al. In situ synchrotron tomography estimation of toughening effect by semi-ductile fibre reinforcement in a tungsten-fibre-reinforced tungsten composite system. *Acta Materialia*. 2013;**61**:7060-7071

[67] Riesch J, Höschel T, You JH. Enhanced toughness and stable crack propagation in a novel tungsten fibre-reinforced tungsten composite produced by chemical vapour infiltration. *Physica Scripta*. 2014;**T159**:014031

[68] Coenen JW, Antusch S, Aumann M, et al. Materials for DEMO and reactor applications—boundary conditions and new concepts. *Physica Scripta*. 2016;**T167**:014002

[69] Mao Y, Coenen JW, Riesch J, Sistla S, Almanstötter J, Jasper B, et al. Influence of the interface strength on the mechanical properties of discontinuous tungsten fiber-reinforced tungsten composites produced by field assisted sintering technology. *Composites Part A Applied Science and Manufacturing*. 2018;**107**:342-353

[70] Jiang Y, Zhang LH, Fang QF, Zhang T, Wang XP, Hao T, et al. Toughness enhancement of tungsten reinforced with short tungsten fibres. *Materials Science and Engineering A*. 2017;**690**:208-213

[71] Du J, Hochen T, Rasinski M, You J-H. Shear debonding behavior of a carbon-coated interface in a tungsten fiber-reinforced tungsten matrix composite. *Journal of Nuclear Materials*. 2011;**417**:472-476

[72] Riesch J, Han Y, Almanstötter J, Coenen JW, Höschel T, Jasper B, et al. Development of tungsten fibre-reinforced tungsten composites towards their use in DEMO—potassium doped tungsten wire. *Physica Scripta*. 2016;**T167**:014006

[73] Riesch J, Buffiere J-Y, Höschel T, Scheelc M, Linsmeiere C, You J-H. Crack bridging in as-fabricated and embrittled tungsten single fibre-reinforced tungsten composites shown by a novel in-situ high energy synchrotron tomography bending test. *Nuclear Materials and Energy*. 2018;**15**:1-12

[74] Avello de Lama M, Balden M, Greuner H, Höschel T, Matejcek J, You JH. Microstructural stability of spark-plasma-sintered Wf/W composite with zirconia interface coating under high-heat-flux hydrogen beam irradiation. *Nuclear Materials and Energy*. 2017;**13**:74-80

[75] Riesch J, Aumann M, Coenen JW, Gietl H, Holzner G, Höschel T, et al. Chemically deposited tungsten fibre-reinforced tungsten—the way to a mock-up for divertor applications. *Nuclear Materials and Energy*. 2016;**9**:75-83

[76] Linsmeier C, Rieth M, Aktaa J, et al. Development of advanced high heat flux and plasma-facing materials. *Nuclear Fusion*. 2016;**57**:092007

Edited by Aamir Shahzad

This book highlights the need for environmentally friendly energy sources. One of the most significant problems facing civilization today is how to generate alternative clean energy sustainably and in sufficient quantity to supply a growing global population. Fossil fuel burning machines pollute the atmosphere resulting in global warming and causing health risks. Alternatively, fusion energy does not produce any carbon dioxide.

This book discusses the latest developments and innovative techniques of fusion energy and its practical uses. Chapters cover such topics as beam injectors for fission reactors, detachment in helical fusion devices, wave instabilities in dusty plasmas of fusion devices, tungsten-based plasma materials, migration energy by high-voltage electron microscopes, and taxonomy of big nuclear chambers.

Published in London, UK

© 2020 IntechOpen
© MVal / iStock

IntechOpen

